UNIVERSITY OF PUERTO RICO

RIO PIEDRAS CAMPUS

COLLEGE OF NATURAL SCIENCES

DOCTORAL PROGRAM IN CHEMICAL PHYSICS

SYNTHESIS AND CHARACTERIZATION OF CATHODE MATERIALS FOR LITHIUM-SULFUR BATTERIES

BY

CLAUDIA C. ZULUAGA-GÓMEZ

A Dissertation Submitted in Partial Fulfillment of the Requirement of Degree of

DOCTOR OF PHYLOSOPHY IN CHEMICAL PHYSICS

Supervised by

Professor Ram S. Katiyar

DEPARTMENT OF PHYSICS

UNIVERSITTY OF PUERTO RICO

San Juan, Puerto Rico, USA

July 31, 2023

University of Puerto Rico

Rio Piedras Campus

Department of Physics

We hereby recommend that the research work presented by Claudia C. Zuluaga-Gómez in this thesis entitled " **Synthesis and characterization of cathode materials for lithium-sulfur batteries**" is accepted for the partial fulfillment of the requirements for the degree of **Doctor of Philosophy in Chemical Physics Program**, in July 31, 2023.

Prof. Ram S. Katiyar

Thesis Advisor

Department of Physics

Prof. Liz Diaz	Prof. Gerardo Morell
Thesis Committee Member	Thesis Committee Member
Department of Chemistry	Department of Physics

Dedicated to

I dedicate this Ph.D. thesis to my mother, father, siblings, husband, extended family, friends, and professors who with love and effort have accompanied me in this process, without hesitating at any moment to see my dreams come true, making them their own.

Abstract

Lithium−sulfur (Li−S) batteries have attracted considerable interest as next-generation high-density energy storage devices. However, their practical applications are limited due to rapid capacity fading when cycling cells with high mass loading levels. The combination of lithium and sulfur as the active materials in these batteries offers several advantages over traditional lithium-ion batteries. One of the key benefits of Li-S batteries is their high energy density, which allows them to store more energy per unit mass compared to other battery technologies. This makes them particularly attractive for electric vehicles and portable electronic devices where maximizing energy storage capacity is crucial. Another advantage of Li-S batteries is their low cost. Sulfur is an abundant and inexpensive element, making it a cost-effective choice for large-scale battery production. Additionally, the absence of expensive transition metals in Li-S batteries further contributes to their affordability. Furthermore, Li-S batteries exhibit improved safety characteristics compared to conventional lithium-ion batteries. The use of sulfur as the cathode material reduces the risk of thermal runaway reactions, which can lead to battery fires or explosions. This enhanced safety profile makes Li-S batteries a promising option for applications that prioritize safety, such as aerospace devices. One major issue is the shuttle effect, where polysulfide intermediates formed during the discharge process migrate between the cathode and anode, resulting in capacity loss and reduced cycle life. Researchers are actively working on developing strategies to mitigate this effect and improve the overall performance of Li-S batteries.

This work provides a detailed study of composites of sulfur/ferroelectric nanoparticles/holey graphene (S/FNPs/hG) cathodes were fabricated for high-mass-loading S cathodes. The solvent-free and binder-free procedure is enabled using holey graphene as a unique dry-pressable electrode for Li−S batteries. The unique structure of the holey graphene framework ensures fast electron and ion transport within the electrode and affords enough space to mitigate the electrode's volume expansion. Moreover, ferroelectric polarization due to FNPs within S/hG composites induces an internal electric field, which effectively reduces the undesired shuttling effect. With these advantages, the S/FNPs/hG composite cathodes exhibit sustainable and ultrahigh specific capacity up to 1409 mAh/g_s for the S/ BTO/hG cathode. A capacity retention value of 90% was obtained for the S/BNTFN/hG battery up to cycle 18. The high mass loading of sulfur ranging from 5.72 to 7.01 mg$_s$/cm^2 allows maximum high areal capacity up to ∼10 mAh/cm^2 for the S/BTO/hG battery and superior rate capability at 0.2 and 0.5 mA/cm^2. These results suggest sustainable and high-yielding Li−S batteries can be obtained for potential commercial applications.

In additional, this work is the impact of the incorporation of ferroelectric nanoparticles (FNPs), such as BaTiO$_3$ (BTO), BiFeO$_3$ (BFO), Bi$_4$NdTi$_3$Fe$_{0.7}$Ni$_{0.3}$O$_{15}$ (BNTFN), and Bi$_4$NdTi$_3$Fe$_{0.5}$Co$_{0.5}$O$_{15}$ (BNTFC), as well as the mass loading of sulfur to fabricated solvent-free sulfur/holey graphene-carbon black/polyvinylidene fluoride (S/FNPs/CBhG/PVDF) composite electrodes to achieve high areal capacity for Li-S batteries. The dry-press method was adopted to fabricate composite cathodes. The hG, a conductive and lightweight scaffold derived from graphene, served as a matrix to host sulfur and FNPs for the fabrication of solvent-free composites. Raman spectra confirmed

the dominant hG framework for all the composites, with strong D, G, and 2D bands. The surface morphology of the fabricated cathode system showed a homogeneous distribution of FNPs throughout the composites, confirmed by the EDAX spectra. The observed Li+ ion diffusion coefficient for the composite cathode started at 2.17×10^{-16} cm^2/s ($S_{25}(CBhG)_{65}PVDF_{10}$) and reached up to the highest value (4.15×10^{-15} cm^2/s) for $S_{25}BNTFC_5(CBhG)_{60}PVDF_{10}$. The best discharge capacity values for the $S_{25}(CBhG)_{65}PVDF_{10}$ and $S_{25}BNTFC_5(CBhG)_{60}PVDF_{10}$ composites started at 1123 mAh/g$_s$ and 1509 mAh/g$_s$ and dropped to 612 mAh/g$_s$ and 572 mAh/g$_s$, respectively, after 100 cycles; similar behavior was exhibited by the other composites that were among the best. These are better values than those previously reported in the literature. The incorporation of ferroelectric nanoparticles in the cathodes of Li-S batteries reduced the rapid formation of polysulfides due to their internal electric fields. The areal capacity for the $S_{25}(CBhG)_{65}PVDF_{10}$ composites was 4.84 mAh/cm^2 with a mass loading of 4.31 mg$_s$/cm^2, while that for the $S_{25}BNTFC_5(CBhG)_{60}PVDF_{10}$ composites was 6.74 mAh/cm$_2$ with a mass loading of 4.46 mgs/cm^2. It was confirmed that effective FNPs incorporation within the S cathode improves the cycling response and stability of cathodes, enabling the high performance of Li-S batteries.

Acknowledgements

A research study, which is a complex exercise, involves a long process. It cannot be carried out in isolation without reasonable external support, both active and moral, being obtained from numerous sources. Looking back in view of this, I at once realize as to how largely I owe to various people and institutions, too many to specify for having contributed towards the fulfilment of my present goals. Nevertheless, I would be failing in my duty if I avoid placing a few of them on record.

First of all, I want to thank God for granting me strength and health to complete this work. With Him, all impossibilities become possible, because without Him, I could not have gotten this far.

I am very grateful for all the support and assistance I have received in my graduate studies. First, I would like to express my deepest gratitude to my supervisor, Dr. Ram S. Katiyar, for his continuous support, teaching, dedication, and for always believing in me. I also want to thank my tutors in this and other projects, Dr. Margarita Correa, and Dr. Balram Tripathi, for instilling in me an unreserved interest in research; for your friendship and guidance, I am forever grateful. My most sincere thanks also to Dr. Liz Diaz and Dr. Gerardo Morell, who gave me the opportunity to grow beyond being a researcher in science, opening doors in the area of education, and exposure to participate in professional competitions.

Finally, I want to thank a group of friends and work team that gave me full support and assistance in academic and non-academic matters. Academically, I would like to highlight Carolina Rojas Michea, Valerio Dörvilien, Dr. Sita Dugu, Carlos Malca, Dr. Rajesh Katiyar,

Oli Nischal, Mohan Bhattarai, Dr. Ricardo Martínez, Dr. Alvaro Instan, Dr. Danilo Barrionuevo, Dr. Adriana Rivera, and to all my colleagues at the SPECLAB laboratory, for their support. I am grateful to all those with whom I have had the pleasure of working on this and related projects. A special thanks to William Perez, laboratory technician, for his continuous help with laboratory instruments and availability of resources needed for carrying out the research as well as advice, guidance, and constant encouragement.

I also want to thank my parents Blanca O. Gómez Ramirez and Jaime N. Zuluaga Zuluaga, my seven siblings; Adriana, John, Cesar, Sergio, Carlos, Jorge, and Andres Zuluaga Gómez, especially my mother Blanca O. Gómez Ramirez; whose support was unconditional throughout this process. I want to thank my husband Carlos E. Tomassini Quijano who was present at every moment of this arduous journey. Thanks to his constant support it was possible to achieve this goal. I also want to infinitely thank my extended family who have opened a place in their hearts from day one and have supported me in achieving this great goal, my parents in law Amelia M. Quijano Rivera, and Carlos A. Tomassini Ramírez, stepdaughter Jonnalie C. Tomassini Fernandini, Jose Manuel Jiménez Rivera, Aida Luz Rivera Quijano, Aida Isabel Jiménez Rivera, and Maria E. Cabrera Nieves, especially my mother in law Amelia Quijano Rivera, who was always there to provide not only moral support, but also mistake proofing my work and helping me improve my technical writing skills.

I dedicate this Ph.D. thesis to my mother, father, siblings, husband, extended family, friends, and professors who with love and effort have accompanied me in this process, without hesitating at any moment to see my dreams come true, making them their own.

Contents

Chapter 3

Holey Graphene/Ferroelectric/Sulfur Composite Cathodes for High-Capacity

Lithium−Sulfur Batteries

Chapter 4

High Areal Capacity and Sustainable High Energy in Ferroelectric Doped Holey

Graphene/Sulfur Composite Cathode for Lithium-Sulfur Batteries

Chapter 5

List of Tables

List of Figures

Abbreviations and Symbols

This thesis employs the use of specific symbols throughout its content. Further symbols may be introduced as necessary.

Li-S: Lithium-Sulfur

Li-ion: Lithium-ion

PVDF: Polyvinylidene fluoride

LiTFSI: Lithium bis(trifluoromethanesulfonyl)imide

DME: 1,2-dimethoxyethane

DOL: 1,3-dioxolane

τ_D: Diffusion time constant

λ_D: Debye length

l_D: Diffusion length

NMP: N-methyl-2-pyrrolidone

hG: Holey graphene

P_r: Remnant polarization

W_{sc}: Warburg element

R_{ct}: Resistance of charge transfer

FNPs: Ferroelectric nanoparticles

Lists of Publications

1. Holey Graphene/Ferroelectric/Sulfur Composite Cathodes for High-Capacity Lithium−Sulfur Batteries. **<u>Claudia C. Zuluaga Gómez</u>**, Christian O. Plaza-Rivera, Balram Tripathi, Rajesh K. Katiyar, Dhiren K. Pradhan, Gerardo Morell, Yi Lin, Margarita Correa, and Ram S. Katiyar, Journal ACS Omega, 8 (14), 2023. DOI: 10.1021/acsomega.3c00361.

2. High Areal Capacity and Sustainable High Energy in Ferroelectric Doped Holey graphene/Sulfur Composite Cathode for Lithium-Sulfur Batteries. **<u>Claudia C. Zuluaga Gómez</u>**, Christian O. Plaza-Rivera, Balram Tripathi, Rajesh K. Katiyar, Dhiren K. Pradhan, Gerardo Morell, Margarita Correa, and Ram S. Katiyar, Journal Batteries. 9(6), 293 (2023). DOI: 10.3390/batteries9060293.

3. Role of Ferroelectric Nanoparticles Coated Separator in Improvement of capacity Retention at High Current Density on Sulfur/SWCNT composite cathodes for Li-S Batteries. Rajesh K Katiyar, **<u>Claudia C. Zuluaga Gómez</u>**, Swati Katiyar, Balram Tripathi, Gerardo Morell, Brad R. Weiner, and Ram S Katiyar, Journal APL Materials. 11, 051115 (2023). DOI: 10.1063/5.0152737.

4. Revealing Underestimated Performance in the Bismuth Ferrite (BiFeO3) Anode for High-Capacity and Long-Cycling Lithium-Ion Batteries. Nischal Oli, José Fernando Flórez Gómez, **<u>Claudia C. Zuluaga Gómez</u>**, Rajesh Katiyar, Gerardo Morell, Ram Katiyar, Journal ACS Applied Energy Material Submitted being evaluated for publication under Manuscript ID ae-2023-01546h.

5. Capacity Retention and High-rate Performance in Li-S Batteries with Ferroelectric Gd/Ni doped $BiFeO_3$ (BGFNO)@Sulfur/SWCNT Composite Cathode and

BGFNO Coated Separator. Rajesh K Katiyar, **Claudia C. Zuluaga Gómez**, Swati Katiyar, Balram Tripathi, Gerardo Morell, Brad R. Weiner, and Ram S Katiyar. Journal Chemistry accepted July 31,2023.

6. High specific capacity of Lithium-Sulfur batteries with Carbon Black/Chitosan and Carbon Black/Polyvinylidene Fluoride, coated separators. Isaac Paniagua-Vásquez, **Claudia C. Zuluaga Gómez**, Sofía Chacón-Vargas, Allan León Calvo, Giovanni Sáenz-Arce, Ram S. Katiyar, and José Javier Saavedra-Arias, Journal of Energies, 15(6), 2022. DOI: 10.3390/en15062183.

7. Tuning the magnetic phase transition above room temperature through Fe and Mn modification in gallium ferrite with reduced leakage current. Sita Dugu, Shalini Kumari, Dhiren K Pradhan, **Claudia Zuluaga Gómez**, Mikel Holcomb, Ram S Katiyar, Journal of Physics D: Applied Physics, 53, 2020, pp. 225001. DOI: 10.1088/1361-6463/ab795c.

8. Influence of rare-earth substitution on the structural, magnetic, optical, and dielectric properties of ZnO nanoparticles. Ricardo Martínez, **Claudia Zuluaga**, Sandra Dussan, Hannu Huhtinen, Wojciech Jadwisienczak and Ratnakar Palai, MRS Advances, 4, 2019, pp. 675-682. DOI: 10.1557/adv.2019.66

Presentations
Oral Presentations

1. Ferroelectric and Multiferroic Materials being Incorporated into Lithium-Sulfur Batteries to Promote Efficient High-Performance. **Claudia C. Zuluaga-Gomez,** Christian Plaza, Gerardo Morell, Margarita Correa, and Ram Katiyar. MRS Spring Meeting & Exhibit via online in May 2022 in Hawaii.

Presentations

Poster Presentations

1. Holey Graphene/Sulfur Composite Cathodes via Coupling with Ferroelectric Nanoparticles for Sustainable and High-Capacity Lithium-Sulfur Batteries. **Claudia C. Zuluaga Gómez**, Christian O. Plaza-Rivera, Balram Tripathi, Rajesh K. Katiyar, Gerardo Morell, Yi Lin, Margarita Correa, and Ram S. Katiyar. The 243rd ECS Meeting with the 18th International Symposium on Solid Oxide Fuel Cells (SOFC-XVIII). Boston, Massachusetts from May 28 – June 2, 2023.

2. High-Loading, Solvent-Free, and Binder-Free Holey Graphene/Sulfur Composite Cathodes via Coupling with Ferroelectric Nanoparticles for Lithium-Sulfur Batteries. **Claudia C. Zuluaga Gómez**, Christian O. Plaza-Rivera, Balram Tripathi, Rajesh K. Katiyar, Gerardo Morell, Yi Lin, Margarita Correa, and Ram S. Katiyar. NASA MIRO PR-SPRInT, University of Puerto Rico, Rio Piedras campus, December 7, 2022.

3. Ferroelectric Materials Being Incorporated into Lithium-Sulfur Batteries to Promote Efficient High-Performance. **Claudia C. Zuluaga-Gomez,** Gerardo Morell, Margarita Correa, and Ram Katiyar. CAWT Annual Meeting in Dorado PR, May 13-14, 2022.

4. Ferroelectric Materials Being Incorporated into Lithium-Sulfur Batteries to Promote Efficient High-Performance. **Claudia C. Zuluaga-Gomez,** Christian Plaza, and Ram Katiyar. The Forward Research & Innovation Summit 2021 Virtual Edition of Puerto Rico Science, Technology & Research Trust in 2021.

Chapter 1

Introduction

1.1 General background

As society has progressed, the demand for electrical energy to live in comfort has increased. Lithium-Sulfur (Li-S) batteries have demonstrated their potential for high-energy-density applications for powering portable electronics [1]. The development of Li-S batteries dates to the 1960s when researchers first investigated the use of sulfur as a cathode material. However, it was not until the 1980s that Li-S batteries gained significant attention due to their high theoretical energy density and low cost. In the early 1990s, several research groups reported successful demonstrations of Li-S batteries with promising performance characteristics [2, 3]. Over the years, numerous efforts have been made to improve the performance and stability of Li-S batteries. One major challenge has been the dissolution of polysulfides, which can lead to capacity fading and poor cycling stability. To address this issue, various strategies have been proposed, including the use of protective coatings, electrolyte additives, and advanced electrode architectures [4, 5]. This has propelled us to look at the Li-S batteries in the search for more efficient and cost-effective advanced energy storage technologies that are environmentally friendly. Sulfur is a basic earth element obtained extensively from nature at low cost and not toxic. Among the applications of these batteries that can reach high energy density are as power sources of electric vehicles and aircraft due to their high open circuit voltage, high capacity, and non-memory effect [6].

Lithium-ion (Li-ion) and Li-S batteries are both rechargeable battery technologies that have been developed for use in various applications. However, there are some key differences between the two. One of the main differences is the chemistry of the batteries. Li-ion batteries use lithium cobalt oxide or lithium iron phosphate as the cathode material, while Li-S batteries use sulfur as the cathode material [7]. This difference in chemistry affects the performance and characteristics of the batteries. Another difference is the energy density of the batteries. Li-S batteries have a higher theoretical energy density than Li-ion batteries, which means they can store more energy per unit weight. However, Li-S batteries also have lower practical energy density due to issues such as low conductivity and poor cycle life. Cycle life is another important factor to consider when comparing these two battery types. Li-ion batteries typically have a longer cycle life than Li-Sulfur batteries, meaning they can be charged and discharged more times before their capacity starts to degrade. This is because Li-Sulfur batteries suffer from issues such as polysulfide dissolution and shuttle effect, which can cause capacity loss over time [8].

The discharge capacity of current Li-ion batteries technology is reaching its theoretical limit, which is far from enough to keep up with current and growing portable energy needs. The research on Li-S batteries is promising, since they have a high theoretical gravimetric energy density of 2,600 Wh/kg, compared to the energy density of the Li-ion batteries which is lower than 200 Wh/kg [9]. In addition, Li-S batteries have a high theoretical capacity of 1,675 mAh/g and versus 300 mAh/g in Li-ion batteries [5]. The Li metal anode has a large capacity of 3,860 mAh/g [10, 11]. The Li-S batteries charge/discharge are constituted by a cathode of sulfur, an anode of lithium metal, requiring an ether-based electrolyte. In principle, the sulfur existing as ring-like octatonic molecules with a chemical

formula of S_8 will be reduced to Li_2S as the final discharged product and oxidized to sulfur reversibly when the battery is charged [12]. The gravimetric and volumetric energy densities of various electrochemical energy storage technologies are depicted in Figure 1.1 Future Li-S cells are anticipated to have a volumetric energy density similar to that of state-of-the-art Li-ion cells (700 Wh/L) but more than twice the gravimetric energy density with values of 400-600 Wh/kg, according to manufacturer's Sion Power and Oxis Energy [13].
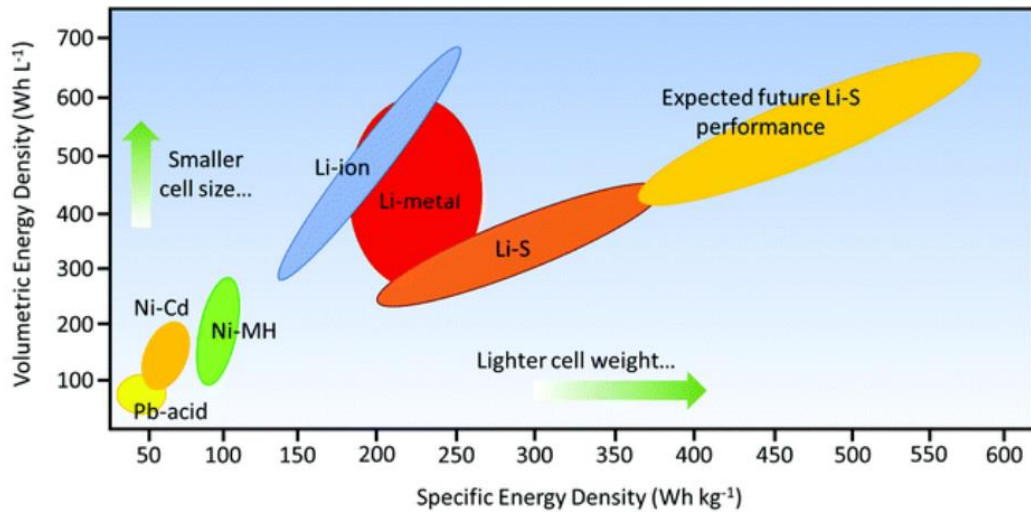
Figure 1.1. Diagram of various electrochemical storage technologies energy densities. Taken from [13]

1.2 Functional component of Li-S batteries

A Li-S battery is an energy storage device that converts the chemical energy of lithium and sulfur into electrical energy by means of an electrochemical reaction. The most important functional components are the anode, cathode, electrolyte, and separator as shown in Figure 1.2.
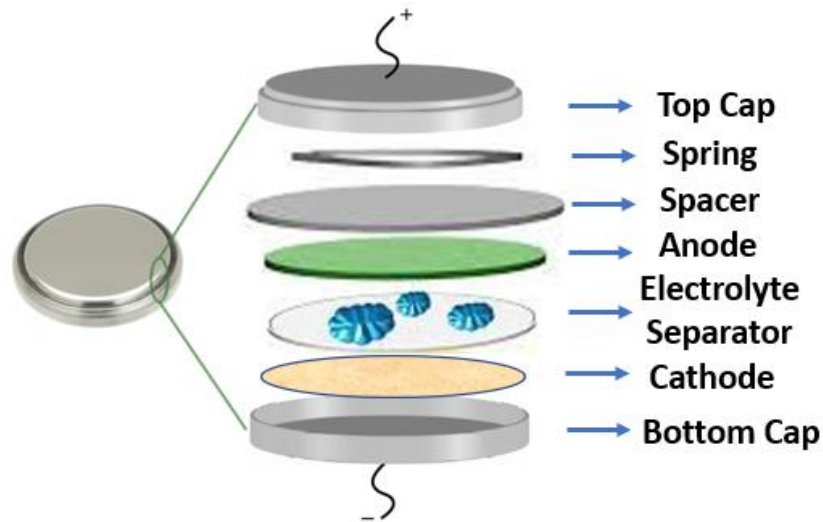
Figure 1.2. Various electrochemical storage technologies energy densities.

1.2.1 Cathode

The cathode of Li-S batteries is a critical component that plays a crucial role in the overall performance and efficiency of the battery. As a virtual sulfur sponge, it absorbs and releases sulfur during the charging and discharging process, respectively. This process involves the conversion of sulfur to lithium polysulfides and back to sulfur, which results in a high energy density [14]. The cathode of Li-S batteries can be made from various materials such as carbon, metal oxides, and polymers. However, the choice of material depends on several factors such as cost, availability, stability, and electrochemical properties [15]. Carbon-based cathodes are the most used due to their low cost, high conductivity, and good mechanical properties. They also have a high surface area, which provides more sites for sulfur absorption and release. Metal oxide cathodes, on the other hand, offer better stability and higher capacity but are expensive and have lower conductivity. Polymer-based cathodes have recently gained attention due to their flexibility, lightweight, and ease of processing. They also offer good mechanical strength and chemical stability. However, they have lower conductivity and may require additional conductive additives to improve their

4

performance [16]. The positive electrode consists of sulfur as an active material, a conductive additive, and a binder. The cathode is usually mounted on an aluminum foil current collector (Figure 1.3) [17]. The electronic conductivity of pure sulfur is very poor (5×10^{-30} S.cm^{-1} at 25 °C), requiring the addition of conductive additives to maintain smooth electron transfer to sulfur [18].
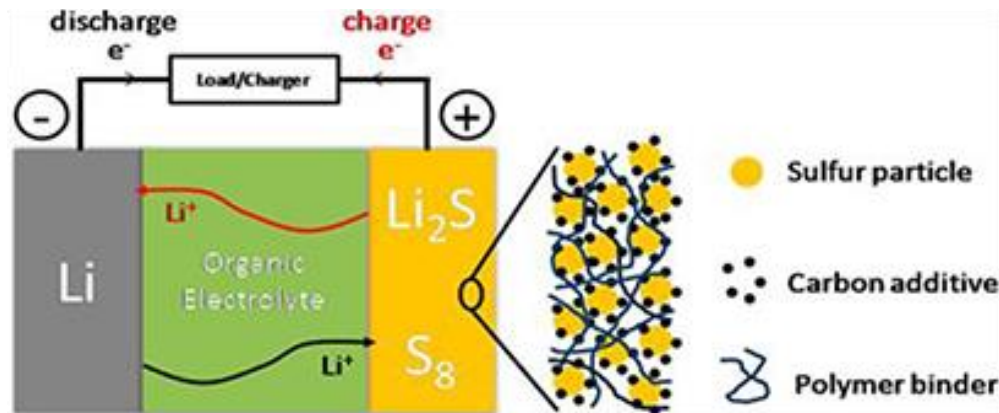
Figure 1.3. Structure scheme of Li-S battery. Taken from [17]

1.2.2 Binder

The challenge in developing these Li-S batteries is finding an effective binder to hold the active materials together. Binder plays a crucial role in the performance and durability of Li-S batteries [19]. It acts as a glue that binds the electrode materials together and provides mechanical strength to the battery. The binder also helps to maintain the structural integrity of the electrodes during repeated charge-discharge cycles. In recent years, several types of binders have been developed for Li-S batteries, including polyvinylidene fluoride (PVDF), carboxymethyl cellulose, and sodium alginate [20]. These binders have shown promising results in improving the performance and stability of Li-S batteries. However, choosing the right binder for a specific application can be challenging. Factors such as the type of electrode material, electrolyte, and operating conditions must be considered when selecting

a binder. Additionally, the binder must be compatible with the manufacturing process and cost-effective [21].

1.2.3 Current collector

The current collector in Li-S batteries must meet several requirements to ensure optimal performance. Firstly, it must be able to conduct electricity efficiently, with low resistance and high conductivity. This is essential for minimizing energy loss and maximizing the battery's power output. Secondly, it must be chemically stable and resistant to corrosion, as the harsh chemical environment within the battery can cause degradation over time. Finally, it should be lightweight and flexible, to allow for easy integration into the battery design. There are several materials that have been investigated as potential current collectors for Li-S batteries. These include metals such as copper, aluminum, and nickel, as well as carbon-based materials like graphene and carbon nanotubes [22]. Each material has its own advantages and disadvantages, and the choice of current collector will depend on factors such as cost, performance, and manufacturability.

1.2.4 Electrolyte

The electrolyte is a component of Li-S batteries. It acts as a medium for the transport of ions between the cathode and anode during charge and discharge cycles. The choice of electrolyte can significantly impact the performance, safety, and stability of the battery. One of the most used electrolytes in Li-S batteries is lithium bis(trifluoromethanesulfonyl)imide (LiTFSI). This salt has excellent solubility in organic solvents, high ionic conductivity, and good electrochemical stability. However, it also suffers from issues such as low redox potential and poor compatibility with sulfur-based cathodes. To overcome these limitations, researchers have explored alternative electrolytes

such as lithium nitrate (LiNO$_3$), lithium iodide (LiI), and lithium perchlorate (LiClO$_4$) [23]. These salts have shown promising results in improving the cycle life, capacity retention, and rate capability of Li-S batteries. Another approach to enhancing the performance of Li-S batteries is the use of solid-state electrolytes. Solid-state electrolytes offer several advantages over liquid electrolytes, including higher thermal stability, lower flammability, and reduced dendrite formation. However, their development and implementation into commercial Li-S batteries are still in the early stages. The most commonly used electrolytes in Li-S batteries are 1,3-dioxolane (DOL) and 1,2-dimethoxyethane (DME) in a volume ratio of 1:1 as solvent, containing 1M LiTFSI salt and 0.2M LiNO$_3$ [24].

1.2.5 Separator

The separator is a crucial component in Li-S batteries as it prevents direct contact between the anode and cathode, which could result in short circuits. The separator also allows for the flow of lithium ions from the anode to the cathode during discharge and vice versa during charging. One of the main challenges with Li-S batteries is the dissolution of polysulfides, which can lead to capacity loss and reduced battery performance over time. Therefore, the separator must be able to effectively trap these polysulfides and prevent them from migrating to the anode or cathode [25]. There are various types of separators used in Li-S batteries, including microporous polyethylene membranes, ceramic membranes, and graphene oxide membranes. Each type has its advantages and disadvantages, such as pore size, mechanical strength, and chemical stability [26].

1.2.6 Anode

The anode is an essential part of the Li-S batteries in the overall performance and efficiency of the battery. As the source of lithium ions during discharge, the anode must be able to accommodate high-capacity cycling without degrading or losing its structural integrity. The metallic lithium anode is responsible for storing and releasing electrical energy during the charging and discharging process. The use of metallic lithium as an anode material offers several advantages over other materials such as graphite or silicon. The main advantage of using metallic lithium is its high theoretical capacity, which is around 3860 mAh/g [27]. Additionally, metallic lithium has a low reduction potential, which allows for a higher voltage output and thus, higher energy density. However, the use of metallic lithium also poses several challenges. One of the major issues is the formation of dendrites, which are tiny needle-like structures that grow from the surface of the anode and can penetrate the separator, causing short circuits and potentially leading to thermal runaway [28].

1.3 Electrochemistry of Li-S batteries

The electrochemistry of Li-S batteries is a complex process that involves the interaction between different materials and chemical reactions. The main components of Li-S batteries are lithium metal as anode, sulfur as cathode, and electrolyte solution. During the discharge process, lithium ions migrate from the anode to the cathode through the electrolyte, while electrons flow through the external circuit, generating electrical energy. The most critical aspect of Li-S batteries is the formation of intermediate species during the discharge/charge cycle [29]. These intermediates include polysulfides (Li_2S_x), which can dissolve in the electrolyte and diffuse back to the anode, leading to capacity loss and reduced performance.

Another challenge in Li-S batteries is the high reactivity of sulfur with lithium, which can cause side reactions and passivation of the electrode surface [5]. This problem can be addressed by optimizing the electrolyte composition and concentration, controlling the charging-discharging rate, and improving the stability of the electrode-electrolyte interface. Overall, the electrochemistry of Li-S batteries is a fascinating field that requires interdisciplinary knowledge and skills. By understanding the fundamental mechanisms and exploring innovative solutions, we can enhance the performance and reliability of Li-S batteries and accelerate their commercialization for various applications, including electric vehicles and portable electronics [30].

1.3.1 Mechanism of Li-S batteries

The Li-S battery is a promising energy storage technology that has attracted significant attention in recent years due to its high theoretical specific capacity and low cost. The basic mechanism of the Li-S battery involves the electrochemical reaction between lithium metal and sulfur to form lithium sulfide (Li_2S) during discharge, and the reverse reaction during charge. During discharge, Lithium ions (Li^+) are oxidized at the anode, releasing electrons that travel through the external circuit to the cathode where they reduce S to form intermediate polysulfides (Li_2S_x) [31]. These polysulfides then react with Li^+ ions from the electrolyte to form solid Li_2S, which is deposited on the cathode surface. This process is reversible during charging, where Li_2S is oxidized back to S and Li^+ ions are released into the electrolyte as shown in Figure 1.4.
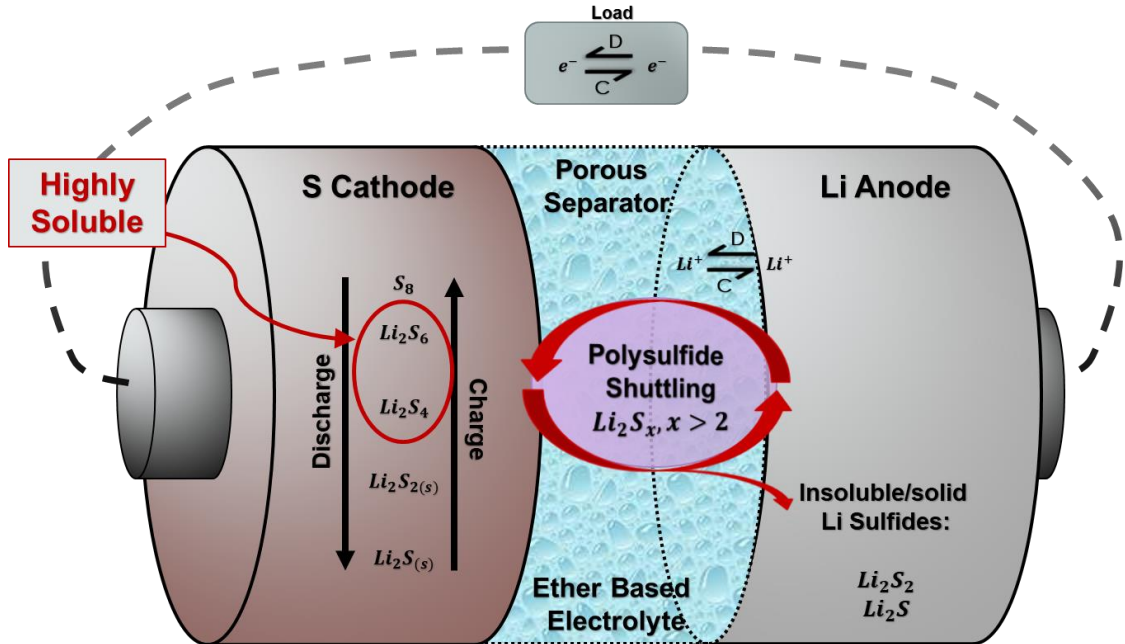
Figure 1.4. Schematic of the electrochemical processes in a Li-S battery.

In Li-S batteries, sulfur exists as polysulfides or sulfides of the general formula Li_2S_n, where n = 1, 2, 4, 6 or 8, depending on the state of charge. In the fully charged state, polysulfides are the highest order (n = 8). During discharge, higher-order polysulfides are reduced until the lowest-order polysulfides (n =1 and 2) are formed. The voltage of a lithium-sulfur cell during discharge ranges from 2.7 to 1.8 V and follows a curve with four different ranges (Figure 1.5) [32]. Although we start with elemental sulfur in the cathode, elemental sulfur is reduced to polysulfides at the first discharge (Equation 1.1).

$$S_8 + 2e^- + 2Li^+ \leftrightarrow Li_2S_8 \quad > 2.3\ V \tag{1.1}$$

During charging, polysulfides are usually not fully oxidized back to elemental sulfur. At voltages above 2.3 V (region I of Figure 1.5), the higher-order polysulfides (n = 8) were reduced to the lower-order polysulfides (n = 6) according to Equation 1.2 [31].

$$3Li_2S_8 + 2e^- + 2Li^+ \leftrightarrow 4Li_2S_6 \quad > 2.3\ V \tag{1.2}$$
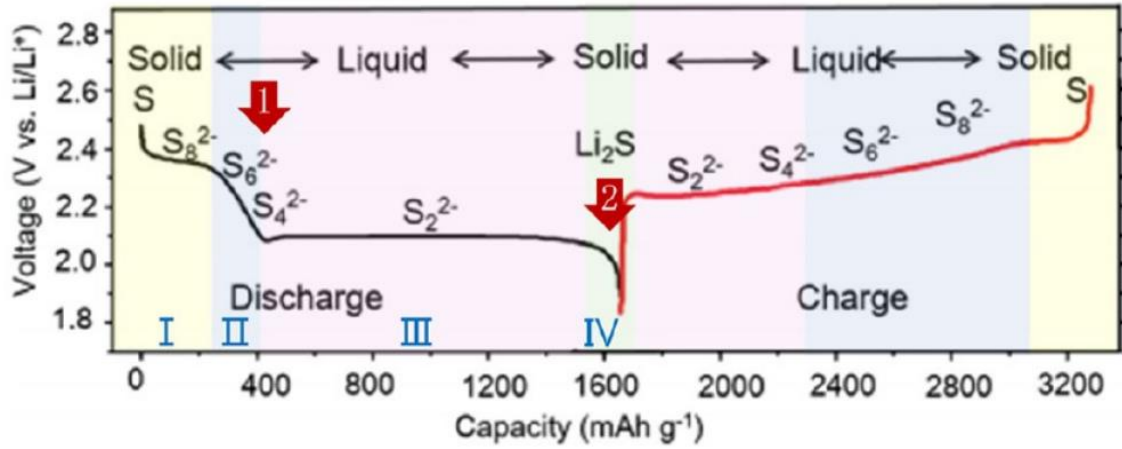
Figure 1.5. Typical discharge-charge profile of the Li−S battery in one cycle, taken from [32].

In the voltage range of 2.3 V to 2.1 V (Region II of Figure 1.5), the n = 6 polysulfides are further reduced to n = 4 soluble products according to Equation 1.3.

$$2Li_2S_6 + 2e^- + 2Li^+ \leftrightarrow 3Li_2S_4 \quad 2.3\,V\,to\,2.1\,V \tag{1.3}$$
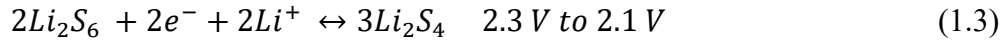
In the voltage range of 1.9 V to 2.1 V (Region III of Figure 1.5), further reduction of polysulfides to insoluble products (n = 1 and n = 2) occurs according to Equation 1.4 and Equation 1.5.

$$Li_2S_4 + 2e^- + 2Li^+ \leftrightarrow 2Li_2S_2 \quad 1.9\,V\,to\,2.1\,V \tag{1.4}$$

$$Li_2S_4 + 6e^- + 6Li^+ \leftrightarrow 4Li_2S \quad 1.9\,V\,to\,2.1\,V \tag{1.5}$$
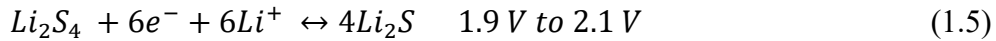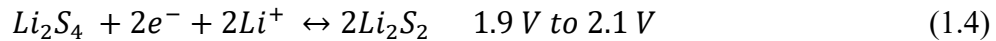
At voltages lower than 1.9 V (Region III of Figure 1.5), lithium polysulfide is converted increasingly to insoluble lithium sulfide as shown in Equation 1.6.

$$Li_2S_2 + 2e^- + 2Li^+ \leftrightarrow 2Li_2S \quad < 1.9\,V \tag{1.6}$$
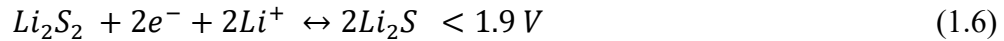
The galvanostatic charge/discharge curve analysis of the working mechanism and limitation factors of Li-S batteries during the cycling produce lithium polysulfides that dissolve. Therefore, the dissolved lithium polysulfide species can move toward lithium

anode through the separation membrane and react with lithium metal, causing the loss of active materials.

1.4 Why is high sulfur loading needed for Li-S batteries

High sulfur loading for the performance of Li-S batteries is needed because sulfur is the active material in Li-S batteries, and increasing its loading can lead to higher energy density and longer cycle life. In addition, high sulfur loading can also improve the safety and cost-effectiveness of Li-S batteries. The reason why high sulfur loading is important is that it increases the amount of active material available for electrochemical reactions. This means that more lithium ions can be stored and released during charge and discharge cycles, leading to higher energy density [33]. Studies have shown that increasing sulfur loading from 1 mg/cm^2 to 6 mg/cm^2 can increase the specific capacity of Li-S batteries by up to 50%. For Li-S batteries to be commercially relevant in electric vehicles, an areal capacity of 4 mA/cm^2 is required [34]. The required sulfur loading can be estimated using:

$$Areal\ capacity\ = \frac{Theoretical\ Sulfur\ capacity\ *\ Sulfur\ loading}{1000}$$

For an areal capacity of 6 mAh/cm^2, a minimum sulfur loading of 3.58 mg/cm^2 is required. However, in practice the theoretical specific capacity of sulfur is difficult to achieve. Therefore, a higher sulfur loading is needed to produce an areal capacity of more than 6 mAh/cm^2. The advantage of high sulfur loading is that it can reduce the formation of unwanted side products, such as lithium polysulfides. These compounds can dissolve in the electrolyte and migrate to the anode, causing capacity loss and reduced cycle life, and this improves the stability of Li-S batteries [35]. The conventional method of Li-S batteries cathode fabrication first consists of mixing the active material with Carbon Black for conductivity adding PVDF as binder, using an organic solvent such as N-Methyl-2-

pyrrolidone (NMP) to form a slurry. The slurry is coated on aluminum foil, and the solvent evaporates. Then the cathodes are cut in disc shape, with low S mass loading ($< 2 \ mg/cm^2$) [29, 36]. Further, multiple fabrications-related problems such as non-uniform coating and crack were encountered. This has become a challenge to achieve high contents of S and low Electrolyte/Sulfur (E/S) ratio.

1.5 Process of Li-S batteries for achieving high areal capacity

To achieve high areal capacity in Li-S batteries, several strategies have been proposed and tested. One approach is to use high-loading sulfur cathodes, which involve packing more sulfur into the electrode to increase its energy density. This can be achieved through various methods such as using nanostructured sulfur or incorporating conductive additives to improve the electrode's conductivity. Another strategy is to modify the anode to enhance its ability to capture lithium ions during charging. Also, electrolyte optimization has been explored to improve the performance of Li-S batteries [37]. By selecting appropriate solvents and additives, researchers have been able to mitigate issues such as sulfur dissolution and shuttle effect, which can degrade the battery's cycling stability and reduce its capacity. Overall, achieving high areal capacity in Li-S batteries requires a multidisciplinary approach that involves optimizing the cathode, anode, and electrolyte components [38]. While considerable progress has been made in this area, further research is needed to overcome remaining challenges and enable widespread adoption of Li-S batteries in practical applications [39].

References

[1] J. Herbert D. and Ulam, Electric dry cells and storage batteries, US3043896A (1962).

[2] S. Ponnada, M.S. Kiai, D.B. Gorle, A. Nowduri, History and recent developments in divergent electrolytes towards high-efficiency lithium–sulfur batteries – a review, Materials Advances 2(13) (2021) 4115-4139.

[3] M.V. Reddy, A. Mauger, C.M. Julien, A. Paolella, K. Zaghib, Brief History of Early Lithium-Battery Development, Materials (Basel) 13(8) (2020).

[4] J.B. Robinson, K. Xi, R.V. Kumar, A.C. Ferrari, H. Au, M.-M. Titirici, A. Parra-Puerto, A. Kucernak, S.D.S. Fitch, N. Garcia-Araez, Z.L. Brown, M. Pasta, L. Furness, A.J. Kibler, D.A. Walsh, L.R. Johnson, C. Holc, G.N. Newton, N.R. Champness, F. Markoulidis, C. Crean, R.C.T. Slade, E.I. Andritsos, Q. Cai, S. Babar, T. Zhang, C. Lekakou, N. Kulkarni, A.J.E. Rettie, R. Jervis, M. Cornish, M. Marinescu, G. Offer, Z. Li, L. Bird, C.P. Grey, M. Chhowalla, D.D. Lecce, R.E. Owen, T.S. Miller, D.J.L. Brett, S. Liatard, D. Ainsworth, P.R. Shearing, 2021 roadmap on lithium sulfur batteries, Journal of Physics: Energy 3(3) (2021).

[5] X. Ji, L.F. Nazar, Advances in Li–S Batteries., *Journal of Materials Chemistry 20*(44) (**2010**).

[6] S. Dorfler, S. Walus, J. Locke, A. Fotouhi, D.J. Auger, N. Shateri, T. Abendroth, P. Hartel, H. Althues, S. Kaskel, Recent Progress and Emerging Application Areas for Lithium-Sulfur Battery Technology, Energy Technol (Weinh) 9(1) (2021) 2000694.

[7] E.J. Cairns, P. Albertus, Batteries for electric and hybrid-electric vehicles, Annu Rev Chem Biomol Eng 1 (2010) 299-320.

[8] S.J.D. Kalpana R. Nagde, Chapter 12 - Li-S ion batteries: a substitute for Li-ion storage batteries, (2021) 335-371.

[9] B. Liu, R. Fang, D. Xie, W. Zhang, H. Huang, Y. Xia, X. Wang, X. Xia, J. Tu, Revisiting Scientific Issues for Industrial Applications of Lithium-Sulfur Batteries., *Energy & Environmental Materials 1*(4) (**2018**) 196-208.

[10] Y.X. Yin, S. Xin, Y.G. Guo, L.J. Wan, Lithium-Sulfur Batteries: Electrochemistry, Materials, and Prospects., *Angew Chem Int Ed Engl 52*(50) (**2013**) 13186-200.

[11] S.H. Chung, C.H. Chang, A. Manthiram, Progress on the Critical Parameters for Lithium–Sulfur Batteries to be Practically Viable., *Advanced Functional Materials 28*(28) (**2018**).

[12] Y.S. Su, A. Manthiram, Lithium-sulphur batteries with a microporous carbon paper as a bifunctional interlayer, Nat Commun 3 (2012) 1166.

[13] M. Hagen, D. Hanselmann, K. Ahlbrecht, R. Maça, D. Gerber, J. Tübke, Lithium-Sulfur Cells: The Gap between the State-of-the-Art and the Requirements for High Energy Battery Cells, Advanced Energy Materials 5(16) (2015).

[14] Y. Yang, G. Zheng, Y. Cui, Nanostructured sulfur cathodes, Chem Soc Rev 42(7) (2013) 3018-32.

[15] A. Eftekhari, D.-W. Kim, Cathode materials for lithium–sulfur batteries: a practical perspective, Journal of Materials Chemistry A 5(34) (2017) 17734-17776.

[16] Y. Zhou, S.L. Candelaria, Q. Liu, Y. Huang, E. Uchaker, G. CaO, Sulfur-rich carbon cryogels for supercapacitors with improved conductivity and wettability, Journal of Materials Chemistry A 2(22) (2014).

[17] Y.F. ARUMUGAM MANTHIRAM, AND YU-SHENG SU, Challenges and Prospects of Lithium-Sulfur Batteries, American Chemical Society (2013).

[18] S. Li, B. Jin, X. Zhai, H. Li, Q. Jiang, Review of Carbon Materials for Lithium-Sulfur Batteries, ChemistrySelect 3(8) (2018) 2245-2260.

[19] A. Abdul Razzaq, Y. Yao, R. Shah, P. Qi, L. Miao, M. Chen, X. Zhao, Y. Peng, Z. Deng, High-performance lithium sulfur batteries enabled by a synergy between sulfur and carbon nanotubes, Energy Storage Materials 16 (2019) 194-202.

[20] Y. Ding, X. Zhong, C. Yuan, L. Duan, L. Zhang, Z. Wang, C. Wang, F. Shi, Sodium Alginate Binders for Bivalency Aqueous Batteries, ACS Appl Mater Interfaces 13(17) (2021) 20681-20688.

[21] A. Manthiram, Y. Fu, S.H. Chung, C. Zu, Y.S. Su, Rechargeable lithium-sulfur batteries, Chem Rev 114(23) (2014) 11751-87.

[22] S.S. Zhang, A review on electrolyte additives for lithium-sulfur batteries, Journal of power sources 231 (2013) 153-162.

[23] N. Angulakshmi, A.M. Stephan, Efficient Electrolytes for Lithiumâ€"Sulfur Batteries, Frontiers in Energy Research 3 (2015).

[24] C.O.P.-R. Claudia C. Zuluaga-Gómez, Balram Tripathi, Rajesh K. Katiyar, Dhiren K. Pradhan, Gerardo Morell, Yi Lin, Margarita Correa, and Ram S. Katiyar, Holey Graphene/Ferroelectric/Sulfur Composite Cathodes for HighCapacity Lithium−Sulfur Batteries, ACS OMEGA (2023).

[25] A. Mullaliu, J. Asenbauer, G. Aquilanti, S. Passerini, M. Giorgetti, Highlighting the Reversible Manganese Electroactivity in Na-Rich Manganese Hexacyanoferrate Material for Li- and Na-Ion Storage, Small Methods 4(1) (2019).

[26] C. Li, R. Liu, Y. Xiao, F. Cao, H. Zhang, Recent progress of separators in lithium-sulfur batteries, Energy Storage Materials 40 (2021) 439-460.

[27] A. Manthiram, S.H. Chung, C. Zu, Lithium-Sulfur Batteries: Progress and Prospects, Adv Mater 27(12) (2015) 1980-2006.

[28] H. Hong, N.A.R. Che Mohamad, K. Chae, F. Marques Mota, D.H. Kim, The lithium metal anode in Li–S batteries: challenges and recent progress, Journal of Materials Chemistry A 9(16) (2021) 10012-10038.

[29] Z. Deng, Z. Zhang, Y. Lai, J. Liu, J. Li, Y. Liu, Electrochemical Impedance Spectroscopy Study of a Lithium/Sulfur Battery: Modeling and Analysis of Capacity Fading, Journal of The Electrochemical Society 160(4) (2013) A553-A558.

[30] G. Zhou, L. Li, D.W. Wang, X.Y. Shan, S. Pei, F. Li, H.M. Cheng, A flexible sulfur-graphene-polypropylene separator integrated electrode for advanced Li-S batteries, Adv Mater 27(4) (2015) 641-7.

[31] Yuriy V. Mikhaylik, z.a.J.R. Akridge, Polysulfide Shuttle Study in the Li-S Battery System, Journal ofThe Electrochemical Society 151 (11) (2004) A1969-A1976.

[32] D. Moy, A. Manivannan, S.R. Narayanan, Direct Measurement of Polysulfide Shuttle Current: A Window into Understanding the Performance of Lithium-Sulfur Cells, Journal of The Electrochemical Society 162(1) (2014) A1-A7.

[33] M. Rana, S.A. Ahad, M. Li, B. Luo, L. Wang, I. Gentle, R. Knibbe, Review on areal capacities and long-term cycling performances of lithium sulfur battery at high sulfur loading, Energy Storage Materials 18 (2019) 289-310.

[34] J. Song, T. Xu, M.L. Gordin, P. Zhu, D. Lv, Y.-B. Jiang, Y. Chen, Y. Duan, D. Wang, Nitrogen-Doped Mesoporous Carbon Promoted Chemical Adsorption of Sulfur and

Fabrication of High-Areal-Capacity Sulfur Cathode with Exceptional Cycling Stability for Lithium-Sulfur Batteries, Advanced Functional Materials 24(9) (2014) 1243-1250.

[35] Y. Feng, G. Wang, J. Ju, Y. Zhao, W. Kang, N. Deng, B. Cheng, Towards high energy density Li–S batteries with high sulfur loading: From key issues to advanced strategies, Energy Storage Materials 32 (2020) 320-355.

[36] D. Lv, J. Zheng, Q. Li, X. Xie, S. Ferrara, Z. Nie, L.B. Mehdi, N.D. Browning, J.-G. Zhang, G.L. Graff, J. Liu, J. Xiao, High Energy Density Lithium-Sulfur Batteries: Challenges of Thick Sulfur Cathodes., *Advanced Energy Materials 5*(16) (**2015**).

[37] A. Manthiram, A reflection on lithium-ion battery cathode chemistry, Nat Commun 11(1) (2020) 1550.

[38] F. Li, Q. Liu, J. Hu, Y. Feng, P. He, J. Ma, Recent advances in cathode materials for rechargeable lithium-sulfur batteries, Nanoscale 11(33) (2019) 15418-15439.

[39] C.C. Zuluaga-Gómez, B. Tripathi, C.O. Plaza-Rivera, R.K. Katiyar, M. Correa, D.K. Pradhan, G. Morell, R.S. Katiyar, High Areal Capacity and Sustainable High Energy in Ferroelectric Doped Holey Graphene/Sulfur Composite Cathode for Lithium-Sulfur Batteries, Batteries 9(6) (2023).

Chapter 2

Synthesis and characterization techniques

2.1 Introduction

This chapter describes the materials used in this research, the synthesis and processing methods used in the fabrication of ferroelectric materials, the fabrication of cathodes for implanted lithium-sulfur batteries, and the characterization of the materials.

Ferroelectric materials are fabricated using a solid-state technique that combines synthesis with mechanochemical activation and thermal treatment. The cathode is made using solvent-free dry pressing and binder technology.

2.2 Materials synthesis

The hG was prepared from graphene (Vorbeck materials) using the established one-step air oxidation procedure reported previously [1]. Bis(trifluoromethylsulfonyl)imide lithium salt (LiTFSI; 98+%), lithium nitrate (LiNO$_3$; 99.999%), 1,2-dimethoxyethane (DME; 99+%), and 1,3-dioxolane (DOL; 99.5%) were purchased from Thermo Fisher. Sulfur (S; 99.998%), highly pure barium carbonate (BaCO$_3$; 99.8%), high purity neodymium (III) oxide (Nd$_2$O$_3$; 99.9%), lithium foil 0.75 mm thick x 19 mm wide (Al; 99.9 %), and high purity cobalt (II, III) oxide (Co$_3$O$_4$; 99.998 %) were purchased from Alfa Aesar. Iron oxide (Fe$_2$O$_3$; 99.998%), nickel (III) oxide nano-powder (Ni$_2$O$_3$; 99%), and Celgard membrane 25 μm thickness and 85 mm width were purchased from Sigma-Aldrich. High-purity bismuth oxide (Bi$_2$O$_3$; 99.9%) was purchased from Fluka, and titanium dioxide (TiO$_2$; 97%) was purchased from Fisher Scientific. All chemical materials for battery assembly

were handled inside an Ar-filled glove box with water (H_2O), and oxygen (O_2) contents < 0.5 ppm. The ferroelectric nanoparticles were synthesized by mechanical activation followed by thermal treatment. Stoichiometric amounts of 15 wt% excess of Bi_2O_3 were used to compensate volatilization loss during the thermal treatment. The oxides were mixed with isopropanol using a high-energy ball-milling planetary machine with zirconia balls (Across International, PQ-N04 planetary ball mill, USA) operating at 45 Hz (2700 rpm) for 8 hrs. The synthesized material was dried on a hot plate at 100 °C for 8 hrs. We used a furnace (Carbolite, HTF1700, USA) at a heating and cooling rate of 5 °C/min in which the powders were calcined.

2.3 Materials characterization techniques

This section briefly describes the characterization techniques such as: X-ray diffraction, Raman spectroscopy, Scanning Electron Microscopy, Energy-Dispersive X-ray Spectroscopy, Electrochemical Impedance Spectroscopy, and Charge-Discharge Profile. The methods and software used for the analysis of the investigated compounds will also be explained in detail.

2.3.1 X-ray diffraction

X-ray diffraction is a powerful analytical technique that allows us to determine the atomic and molecular structure of materials. With this technique, it is possible to know the position of the atoms (ions or molecules) in the structure, determine the parameters of the lattice, the crystalline system, the presence of impurities and even the presence of stress or deformation in the sample. X-ray diffraction occurs when the beam collides with the atoms that make up the crystal, causing the electrons in its path to vibrate with a frequency

identical to the frequency of the incident radiation. These electrons act as secondary sources of new X-ray wavefronts with the same wavelength and frequency [2].
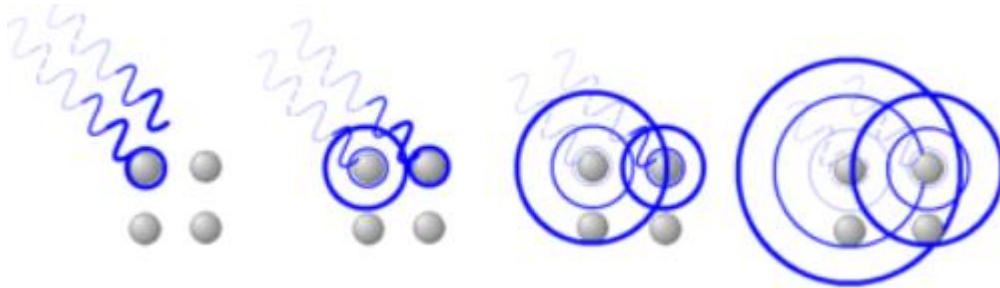
Figure 2.1. Diffraction phenomenon in a crystal. Taken from [2]

The basic principle of X-ray diffraction is that when X-rays are directed at a crystal, they interact with the atoms in the crystal lattice and are scattered in different directions. The scattered X-rays interfere with each other, creating a pattern of bright spots and dark areas on a detector screen. This pattern is known as a diffraction pattern, and it contains information about the arrangement of atoms in crystals. When a crystal diffracts X-rays, the reemitted scattered electromagnetic waves interfere with each other constructively in some directions, i.e., they reinforce each other and cancel each other out in the rest. For this to happen, it is necessary that the difference of paths between the waves diffracted by two successive planes is an integer number of wavelengths ($n\lambda$) [3]. The reflection condition established by W. Bragg indicates that the difference in optical paths traveled is an integer multiple of the wavelength as shown in Equation 2.1:

$$2d \sin \theta = n\lambda \qquad (2.1)$$

where d represents the separation between two consecutive planes and n is an integer that we will call the order of reflection; this equation is known as Bragg's law [4]. Applications of X-ray diffraction in polycrystalline materials are used by Bragg-Brentano geometry,

where the excitation source and the detector are placed at equal distance and angle from the sample surface.
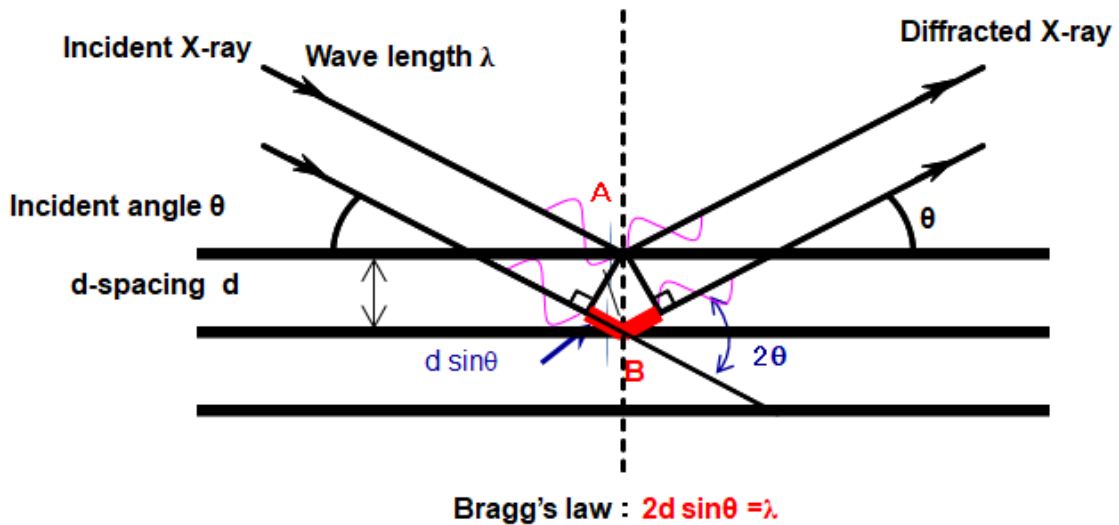
Figure 2.2. Incident on a family of planes of a crystal. Taken from [5]

2.3.1.1 Determination of mean particle size

The determination of the crystal size is based on the broadening of the peaks in the case of small crystal domains, which leads to an inverse relationship between the two parameters. Among the reasons for the broadening of the diffraction pattern, the following points should be emphasized:

a) Instrumental effects

b) Particle size smaller than approximately 0.1 μm

c) Stresses in the crystalline structure due to lattice defects

The different contributions of crystal size, microtensions and instrumental effects can be separated by fitting the peaks to different profiles such as the following:

a) **Gaussian**: rounded peaks where the stress distribution tends to broaden a Gaussian-shaped peak.

b) **Lorentzian**: sharp peaks where the size distribution tends to broaden a profile peak such as dislocations.

c) **Pseudo-Voigt**: preferentially applied when peak broadening is dominated by structural stresses.

d) **Pearson VII**: applied when the broadening is due to crystalline particle size.

The background of the diffractogram, the contribution of $K\alpha_2$, the asymmetry of the peaks, and the start and end points of the integrated peaks need to be correctly determined. With all these parameters, most programs for processing X-ray diffraction data can theoretically fit the experimental curves and perform the calculations automatically [5].

There are several methods to estimate the size of crystallites, the two main ones being Scherrer and Williamson-Hall. These two are based on the elongation of X-ray diffraction peaks.

2.3.1.2 Scherrer's method

The most common and simple method for estimating the size of crystalline particles from the widths of their X-ray diffraction peaks is the one developed by Scherrer in 1918 based on the Equation 2.2:

$$D = \frac{K\lambda}{\beta \cos \theta_\beta} \qquad\qquad (2.2)$$

where D is the crystalline particle size, K the Scherrer constant which depends on the profiles of the crystalline particles present in the sample (K = 0.9) , λ the monochromatic wavelength of the radiation used and β is the peak width (integral width) present at angle θ_β measured in radians, which is calculated by the following Equation 2.3:

$$\beta = \sqrt{(\beta_{exp})^2 - (\beta_{ins})^2} \qquad\qquad (2.3)$$

Figure 2.3 shows the instrumental width β_{ins} (diffraction angle dependent) to be obtained through the measurement of patterns and subtraction of the integral width of the experimental diffraction peaks β_{exp}.
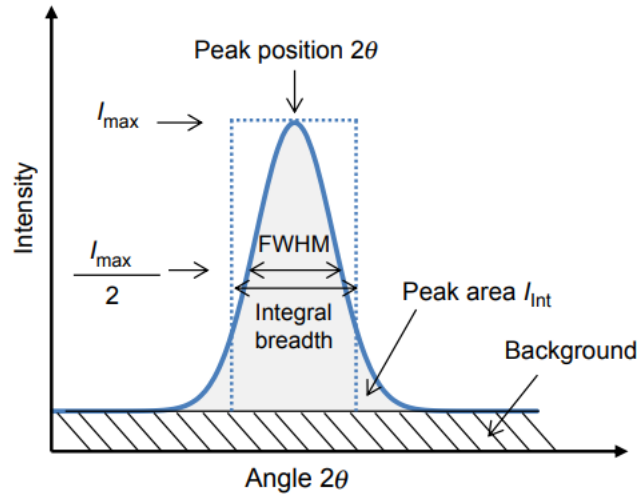
Figure 2.3. Diffraction peak and information content that can be extracted. Taken from [6]

If the instrumental contribution β_{ins} is not known, the FWHM value (peak width at half-height of maximum intensity) can be assumed as the area of the peak divided by its height. Scherrer's method does not take into account the stresses that may take place in the crystalline domain, and that the elongation of diffraction peaks is exclusively due to the crystallite size [6].

2.3.1.3 Williamson-Hall method

In 1953, Williamson and Hall proposed a method using the simplified integral width to deconvolute the contributions of crystalline particle size and stresses due to peak broadening as a function of 2θ; this model assumes a Lorentzian profile for the peaks.

This method considers the presence of micro-deformations or distortions of the lattice within the domain since it also leads to elongation of the diffraction peaks. These twists

consist of random displacements of the unit cell or group of units relative to the ideal position [7, 8]. The particle size and microstrain in the material are obtained by the relationship of Equation 2.4:

$$\beta_{WH} \cdot \cos\theta = 2\xi \cdot \sin\theta + \frac{K\lambda}{D_{WH}} \qquad (2.4)$$

where D_{WH} is the size of the particle by the Williamson-Hall method. The plotting β_{WH} Cos θ as a function of sin θ yields a straight line as shown in Figure 2.4.
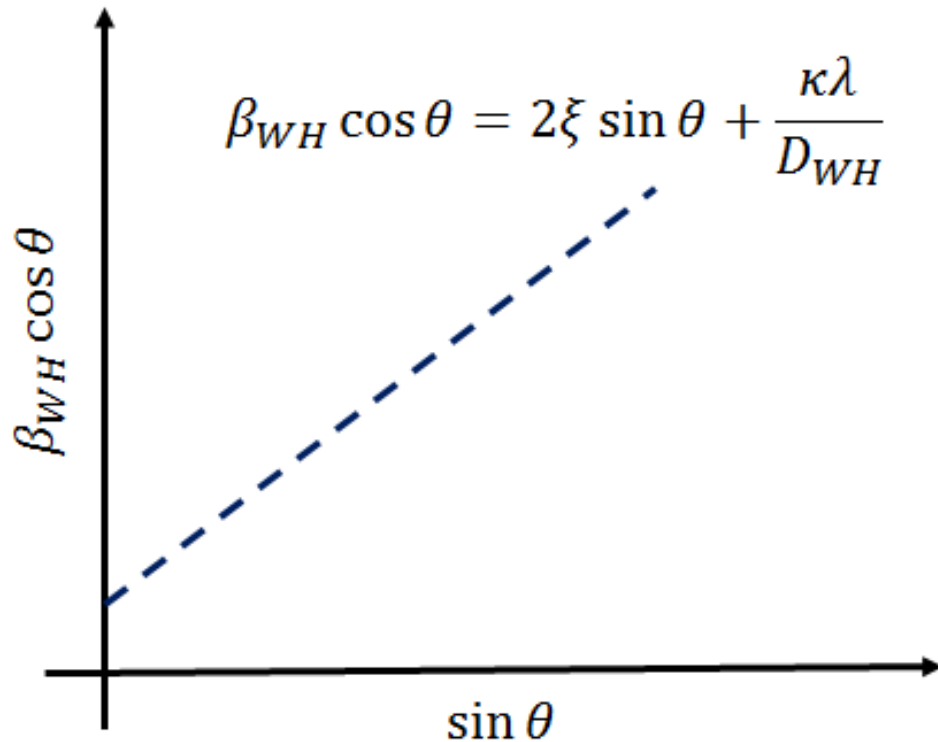
Figure 2.4. Extrapolation of the points (obtained from the diffraction peak widths) allowing the calculation of crystallite size and microstrain.

In this way, the value of microstrain can be calculated from the slope of the line and the particle size using the intercept of the line. The slope of the line can be positive, negative, or zero: a positive value indicates an extension of the network, a negative value

indicates network compression, and a zero slope indicates no microstrain (perfect crystal).

2.3.1.4 Rietveld refining

The method developed by Rietveld exploits all the overlapping information in the powder diffraction pattern to precisely determine the structure of any polycrystalline material, making it the most powerful technique currently available for studying the crystal structure of a material. The Rietveld method includes theoretical fitting of structural parameters as well as experimental parameters of the complete diffraction pattern profile. The initial parameters are adjusted in an iterative process until convergence is reached between the experimental values and the theoretical model. Advances in computing technology and the free availability of programs such as GSAS, DBWS, and FullProf have made the Rietveld method an easy-to-use and increasingly widely used technique. The basis of the method is to use the intensity profile data of each reflection instead of its integration area for the refinement process, which makes it possible to extract the maximum amount of information contained in the dust map. The iterative process tries to minimize the discrepancy between the crystallographic model and the experimental data by means of least squares refinement [9, 10]. The function that is minimized by least squares is called the Sy residual and is shown in Equation 2.5:

$$S_y = \sum_i w_i |Y_i - Y_{cal}|^2 \qquad\qquad (2.5)$$

In this function, y_i is the observed (experimental) intensity at the subindex i step of the diffractogram, y_{cal} is the calculated intensity at the subindex i step, W_i is the respective weight given to the intensities while the summation is over all points of the diffraction pattern. The refinement consists of finding the optimum values of all these parameters so

that S_y adopts the minimum possible value. The calculated intensities y_{cal} are obtained from the F_k, where F_k are the structure factors, whose values are calculated from the structural model. The intensity of a peak is calculated by the following Equation 2.6:

$$Y_i = \sum_j y_{i,j} = \sum_j S_j \sum_k L_{k,j} |F_k|^2 \emptyset_{k,j} (2\theta_i - 2\theta_k) P_{k,j} A + y_{b,j} \qquad (2.6)$$

where Y_i is the calculated intensity at the point i of the diffraction pattern, $y_{i,j}$ is the intensity at point i of the diffraction pattern due to the phase j, S_y is the scaling factor corresponding to phase j, $L_{k,\,j}$ represents polarization factors, multiplicity and Lorentz factor, $L_{k,\,j}^2$ phase j structure factor, $\emptyset_{k,\,j}(2\theta_i\text{-}2\theta_{k,j})$ is the function describing the diffraction peak profile centered at the Bragg angle $2\theta_k$ of the phase j, $P_{k,\,j}$ is the function describing the preferential orientation when the crystals of phase j are not randomly located, A is the absorption factor which depends on the thickness of the sample and the geometry of the diffraction equipment, and $y_{b,i}$ is the background intensity at point $2\theta_i$ of the diffraction pattern.

For refinement, it is necessary to implement functions that model diffraction peaks and other functions that describe the full width at half maximum (FWHM). We can use analytical functions that generate normalization functions for peak description. These functions mainly depend on three parameters such as: position 2θ, intensity I and mean width at maximum height. There are numerical criteria that can indicate the progress of the refinement process and help to infer the suitability of the chosen method. Therefore, several indicators of this cycle need to be implemented so that it can be determined whether the process is satisfactory or not. Some numerical standards used in this method are:

The weighted pattern residual (R_{wp}): determines the residual weight on the basis that the experimental data points of high intensities are more important than those of low intensities. It is also the most statistically significant index of the overall fit as shown in Equation 2.7 [11].

$$R_{wp} = \left(\frac{\Sigma_i W_i |y_{i(obs)} - y_{i(cal)}|^2}{\Sigma_i W_i |y_{i(obs)}|^2} \right)^{1/2} \qquad (2.7)$$

where R_{wp} is the residue of the weighed standard, $y_{i(obs)}$ is the intensity observed at the subindex i step, $y_{i(cal)}$ is the intensity calculated at the subindex i step, W_i is the assigned weight.

The residual of the expected value (R_{exp}): expresses the estimation of the quality of the data considering that data with more noise or peaks with low intensities will have a large R_{exp} as shown in Equation 2.8 [11]:

$$R_{exp} = 100 \left(\frac{(N-P)}{\Sigma_i W_i |y_{i(obs)}|^2} \right) \qquad (2.8)$$

where R_{exp} is the residual of the expected value, N the number of observed data, P the number of parameters to be refined.

The Bragg factor residual (R_b): is an index that numerically expresses the difference between observed and calculated data points on a point-for-point basis as shown in Equation 2.9:

$$R_b = 100 \left(\frac{\Sigma_k |I_{k(obs)} - I_{k(cal)}|^2}{\Sigma_k |I_{k(obs)}|^2} \right) \qquad (2.9)$$

where R_b is the residual of the Bragg factor, $I_{k(obs)}$ is observed intensity at subscript k reflection, $I_{k(cal)}$ is calculated intensity at subscript k reflection. Another parameter to consider is the goodness of fit (chi-square) which is calculated as shown in Equation 2.10:

$$\chi^2 = \frac{R_{wp}}{R_{exp}} \qquad (2.10)$$

where χ^2 is the goodness-of-fit, R_{wp} and R_{exp} are the heavy standard and expected value residuals. A value of χ^2 of the order of 1.3 is usually considered satisfactory [11-13].

For the Rietveld refinement process and the identification of phases of the diffraction patterns of the study samples, the software X'pert High ScorePlus and Fullprof Suite were used. The phases were identified by X'pert High Score Plus, using the 2004 PDF - 2 database. Once the phases present in the sample have been identified, the refinement is carried out and the characteristic graph is obtained, where the red line represents the observed pattern, the black lines represent the calculated pattern, the blue lines represent the difference between the observed and calculated pattern, and finally the green lines indicate the Bragg positions of the phases present.

2.3.2 Raman spectroscopy

Raman spectroscopy is a high-resolution technique, which allows to quickly know information about the material under study, its structural and chemical properties, thus allowing its identification. It is a non-destructive analysis technique, so it does not produce alterations on the analysis surface [14]. At the beginning of the 20th century, the possibility of the existence of a non-elastic scattering of light in the interaction between photons and molecules was postulated. Schrödinger and Dirac, among others, considered this possibility. However, it was not until 1923 when in India Sir Chandrasekhara Venkata

Raman and his collaborator, K.S. Krishnan, discovered the phenomenon of inelastic light scattering [15]. The scientific importance of this discovery earned Sir C.V. Raman the Nobel Prize. At the end of the 1990s, Raman spectroscopy was only academic, but with the technological development of new excitation sources such as lasers and novel detection equipment, it has become an expanding technique and is increasingly present in the characterization protocols of a large number of compounds. The applications of Raman spectroscopy are found in a number of scientific disciplines such as: archeology, biology, in the investigation of material properties at manometric scale, among others [16]. The Raman effect consists of the inelastic scattering of visible light through interactions with the vibrational states of molecules. When monochromatic radiation of a frequency ν_0 is incident on any material, the absorbed incident photons excite the molecules of the material to a virtual excited state. If the virtual state decays, the emitted photons possess mostly the same energy as that of the absorbed photons. This is known as elastic or Rayleigh scattering. However, a small fraction of the emitted photons undergoes an energy change after scattering which is known as inelastic scattering, emerging with a frequency ν_R different from that of the incident photons which is known as the Raman effect [17]. Due to the existence of a series of selection rules imposed by quantum mechanics, not all vibrational modes are active in Raman. Only those that produce a change in polarizability are active. Normally, the molecule ends up at a higher energy level so that the energy released is less than that absorbed, thus increasing the wavelength, and decreasing the frequency of the radiation. This Raman scattering is called Stokes (with frequencies $\nu_0 - \nu_R$) [18]. If the molecule ends up at a lower energy level, more energy is released than is absorbed, which decreases the wavelength and increases the radiation frequency. This

Raman scattering is called anti-Stokes (with frequencies $\nu_0 + \nu_R$). These two bands are symmetrically located on both sides of the Rayleigh band as presented in Figure 2.5 [18].
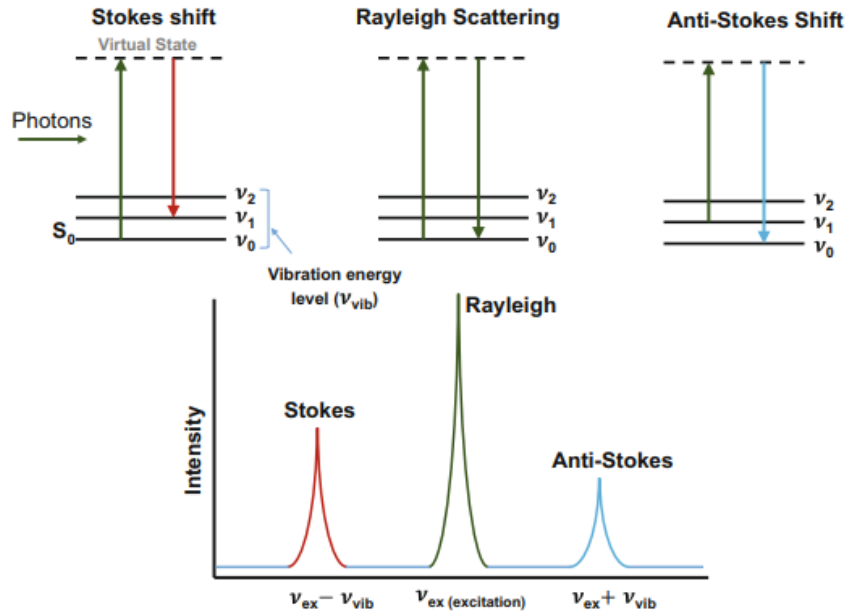
Figure 2.5. Representation of the Rayleigh Scattering versus Stokes Raman and Anti-Stokes Raman Scattering. Taken from [18]

2.3.3 Scanning electron microscope

In a scanning electron microscope (SEM), an electron beam is scanned across the sample. Electrons scattered through large angles such as secondary scattering and backscattering are used to obtain information about the sample. SEM provides chemical information and surface sensitivity when equipped with energy-dispersive and wavelength-dispersive X-ray detectors. In this work, the microstructure and grain growth of ferroelectric nanoparticles materials for each Li-S battery cathode composition were recorded using SEM JEOL model JSM-5800LV.

2.3.4 Energy-dispersive X-ray spectroscopy

Energy dispersive X-ray spectroscopy (EDS) is an elemental analysis technique based on the generation of characteristic X-rays in atoms by electrons in the incident beam. The incident beam can excite an electron in the inner shell, pushing it out of the shell, creating an electron hole. During this stage, two basic physical events occur, elastic scattering and inelastic scattering. Elastic scattering involves changing the direction of an electron without losing energy. It is usually caused by interaction with the core composed of materials. Inelastic scattering is a loss of energy without a discernible change in direction, usually produced by interactions with bonding electrons and the nuclei of atoms. However, the atoms are ionized [19]. Then an electron from the higher energy outer shell fills the hole, and the energy difference between the higher energy shell and the lower energy shell can be released as X-rays.

2.4 Electrochemical characterization

The electrochemical characterization techniques are used to gain insights into the behavior of various materials and systems. Electrochemical impedance spectroscopy and charge-discharge measurements have been particularly valuable for the research.

2.4.1 Electrochemical impedance spectroscopy

The Electrochemical impedance spectroscopy (EIS) can be traced back to the early 20th century when researchers began investigating the behavior of electrolytic cells. However, it was not until the 1970s that EIS gained widespread recognition as a versatile tool for characterizing electrochemical interfaces [20]. Since then, advancements in instrumentation and data analysis techniques have further enhanced the capabilities and applications of EIS. The EIS technique allows for the determination of the electrical

properties of a system by measuring its response to an applied sinusoidal voltage or current signal over a range of frequencies [21]. This technique provides information about the interfacial processes, such as charge transfer resistance and double-layer capacitance, which are crucial in understanding the kinetics and efficiency of electrochemical reactions, the optimization of novel electrochemical devices, contributing to advancements in fields such as energy storage, corrosion protection, and sensor technology [22].

The EIS may be used to characterize either the static or dynamic impedance of a battery. Regardless of whether galvanostatic or potentiostatic mode is used, the AC signal, and therefore the response, is sinusoidal [23].

Resistance refers to the dissipation of energy in a circuit due to the presence of resistors. It is represented by the symbol R and is measured in ohms. Resistance determines how much current will flow through a circuit when a voltage is applied, according to Ohm's Law: V = I * R, where V is the voltage, I is the current, and R is the resistance. The impedance, Z, is a frequency-dependent complex number characterized by the ratio of voltage to current and the phase angle shift between them, Ø as shown in Equation 2.11 to Equation 2.13 [24].

$$Z = \frac{V}{I} = Z_o e^{j\emptyset} \qquad\qquad (2.11)$$

$$Z = Z_o(Cos\,\emptyset + jSin\,\emptyset\,) \qquad\qquad (2.12)$$

$$Z = Z' + jZ'' \qquad\qquad (2.13)$$

where j is the $\sqrt{-1}$, Z' is the real part, and Z" is the imaginary part.

A significant amount of information is acquired by varying the applied frequency in an EIS measurement. Two graphs are commonly used to fully represent this complex

dataset: Nyquist and Bode plots (Figure 2.6). They are complementary and contain the same data as shown in Equation 2.14 and Equation 2.15 [25].

$$|Z(\omega)| = \sqrt{Z'(\omega)^2 + Z''(\omega)^2} \qquad (2.14)$$

$$\emptyset(\omega) = \tan^{-1}\left(\frac{Z'(\omega)}{Z''(\omega)}\right) \qquad (2.15)$$
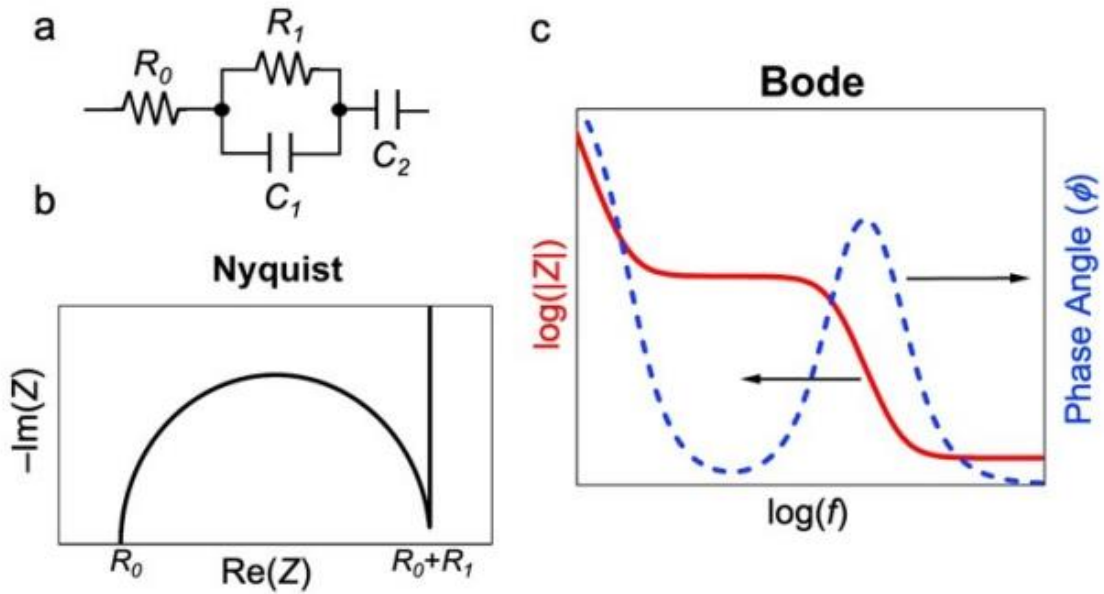
Figure 2.6. a) Equivalent circuit for single electron transfer and ion migration in the electrolyte. b) Nyquist plot of the real impedance against the imaginary impedance showing the resistance for the electrolyte. c) Bode plot of the magnitude of the impedance and phase angle against frequency. Taken from [25]

The Nyquist and Bode plots for various simple electrical circuits containing a single passive element (R,C, or L) as well as combinations of them in different arrangements (in series or in parallel) are illustrated in Figure 2.7 and Figure 2.8, respectively.
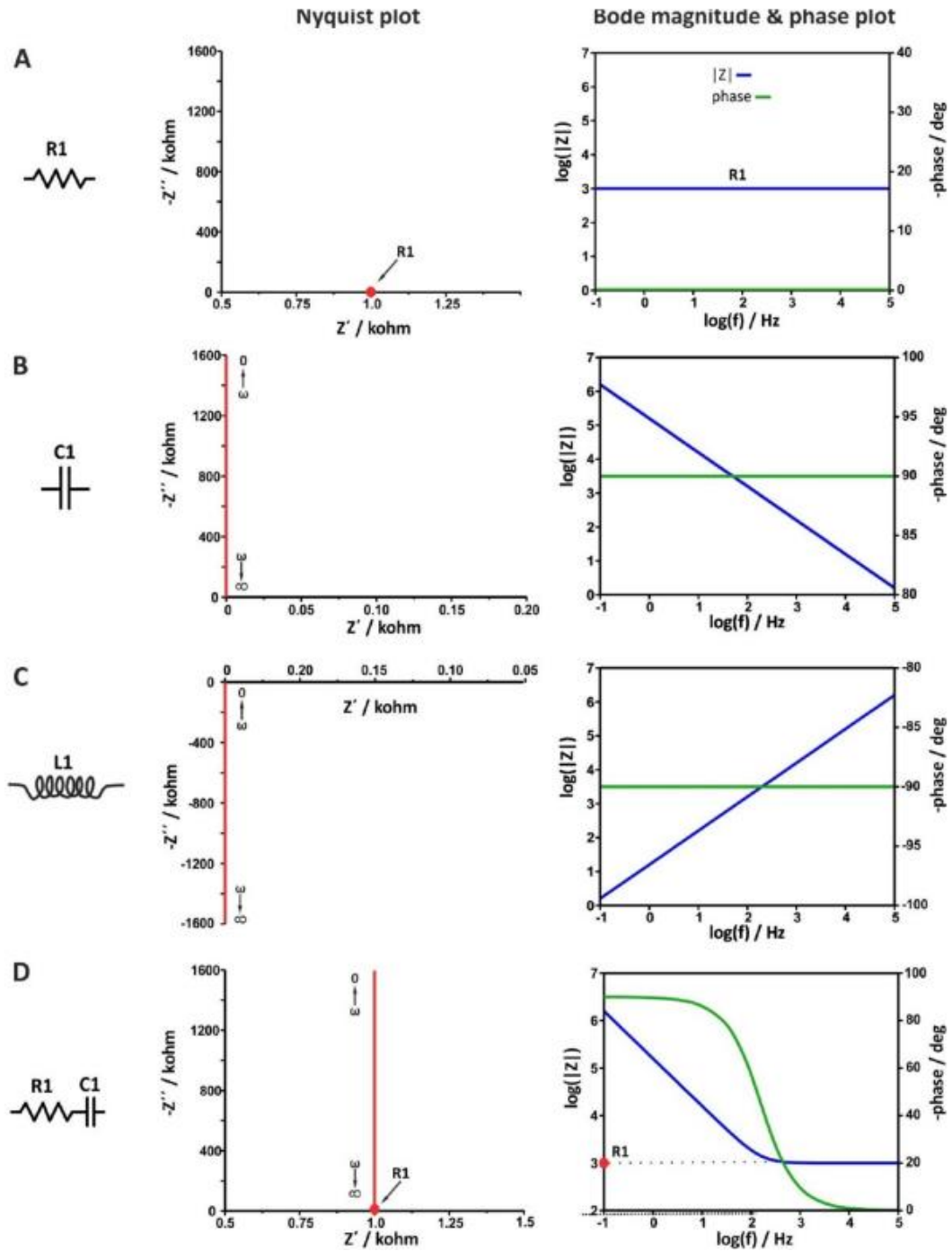
Figure 2.7. Nyquist, Bode magnitude and phase angle plots of some model circuits R1=1kOhm.

Taken from [25]

The Nyquist, bode magnitude, and phase angle plots are essential tools in analyzing the

behavior of model circuits. These plots provide valuable insights into the frequency

response characteristics of a circuit, allowing to assess stability, gain, and phase shift. When the circuit contains only a resistor, Figure 2.7A, the equation of the impedance is $Z = Z' + j(0)$. The real part equals Z', while the imaginary part is zero. As a result, the Nyquist plot shows a single point lying in the real axis. That is, the impedance values at all the excitation frequencies are exactly the same and equal to the value of the resistance of the resistor (in this example, R1 = 1 kOhm). As a result, the Bode magnitude plot shows a straight line that crosses the left axis at $|Z| = R1$ [26].
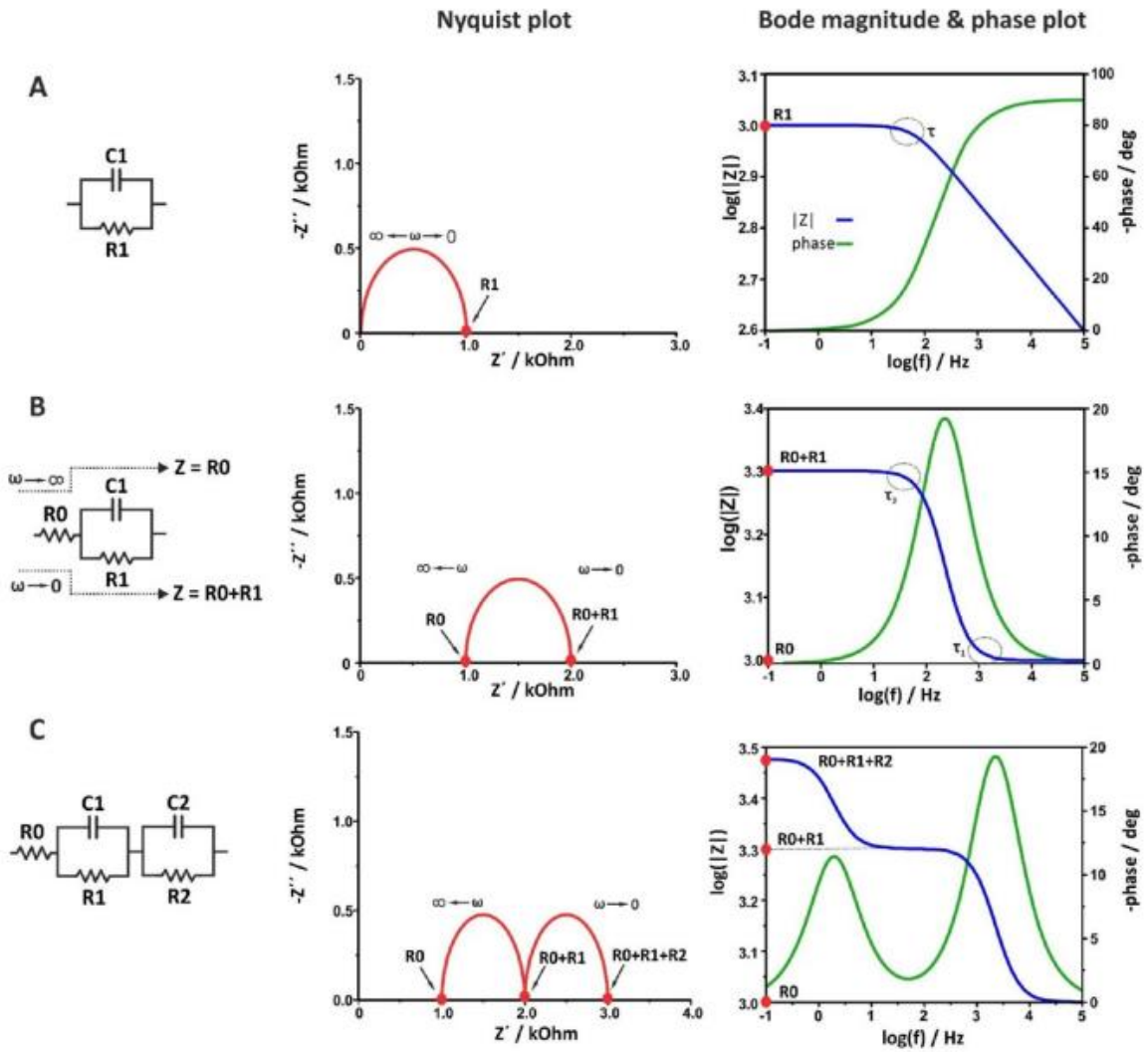
Figure 2.8. Nyquist, Bode magnitude, and phase angle plots of some model circuits. R0 = R1 = R2 = 1 kOhm. Taken from [25]

The Bode magnitude plot showcases the amplitude response of a circuit over a range of frequencies. This plot is particularly useful for understanding the gain characteristics of a system. It can easily identify the cutoff frequency, where the gain starts to decrease, and determine the overall gain of the system at different frequencies. Additionally, the slope of the magnitude plot provides insights into the system's order and its ability to amplify or attenuate certain frequencies as shown in Figure 2.8.

When analyzing the diffusion behavior of ions or molecules, impedance spectroscopy data can provide valuable insights. By studying the electrical response of a system to an applied alternating current (AC) signal, we can extract information about the diffusion coefficients of species present in the solution. The diffusion coefficient is defined via the diffusion length, l_D and the diffusion time constant, τ_D as shown in Equation 2.16:

$$D = \frac{l_D^2}{\tau_D} \qquad (2.16)$$

Therefore, these two parameters must be extracted from experimental data or theoretical models. However, in electrochemical systems, the net mobility-diffusion coefficient can be determined from the effective permittivity model through the relaxation time (τ_2) distribution of the bilayer thickness (equal to the Debye length λ_D) during charge polarization, see Equation 2.17 [27]:

$$D_m = \frac{\lambda_D^2}{\tau_2} \qquad (2.17)$$

The diffusion length is based on the Equation 2.18 to Equation 2.23.

$$l_D = \sqrt{(\tau_s \ x \ D_m)} \qquad (2.18)$$

$$D_m = \lambda_D^2 / \tau_1 \qquad\qquad (2.19)$$

$$\lambda_D = d/\delta \qquad\qquad (2.20)$$

$$tan(\phi)_{max} = \sqrt{\delta}/2 \qquad\qquad (2.21)$$

$$Z_W = \frac{W_{sc}}{\sqrt{\omega}} (1-j)tanh[W_{sc} \sqrt{j\omega}] \qquad\qquad (2.22)$$

$$\tau_D = W_{sc}^2 \qquad\qquad (2.23)$$

where D_m and λ_D are the diffusion coefficient of net mobility and the Debye length of the electrode, respectively, δ is a dimensionless number, τ_1 is the reciprocal of the frequency corresponding to the inflection point of the Nyquist, τ_s is the reciprocal of the frequency corresponding to the highest point in the Bode plot, $tan(\phi)_{max}$ can be obtained from loss tangent, d is the half thickness of the electrode, and W_{sc} is a part of the Warburg element, which can be extracted from the simulated equivalent circuit. Similarly, the τ_1, τ_s, $tan(\phi)_{max}$ and W_{sc} can be obtained from the Nyquist plot, Bode Plot, loss tangent plot and simulated equivalent circuit diagram, respectively [25, 27-29].

2.4.2 Charge-discharge profile

The charge-discharge profile is a battery performance analysis. It provides valuable insights into the behavior and characteristics of a battery during its operation. In energy storage systems, the process of charge-discharge plays a role in determining the overall performance and efficiency [30]. It involves the transfer of electrical energy into and out of a storage device, such as batteries, enabling them to store and release energy as needed. During the charging phase, electrical energy is supplied to the storage device, causing the accumulation of electric charge within its components. This process typically involves an external power source, which delivers the necessary voltage and current to overcome

internal resistance and drive the charge transfer. Conversely, the discharging phase involves the release of stored electrical energy from the storage device, allowing it to power external devices or systems. As the discharge occurs, the stored charge gradually depletes, resulting in a reduction of voltage and available energy. Like the charging process, discharging also depends on the specific technology utilized, with variations in discharge rates, capacity, and voltage profiles. Efficient charge-discharge cycles are crucial for maximizing the lifespan and performance of energy storage systems. Factors such as charging/discharging rates, depth of discharge, temperature management, and voltage control significantly impact the overall efficiency and longevity of the storage device. Proper monitoring and control of these parameters are essential to prevent overcharging, over-discharging, or excessive heat generation, which can lead to degradation and reduced operational capabilities [31].

Generally quantitative electrochemical performances of battery material are evaluated by Galvanostatic cycling (or cyclic chronopotentiometry) method. In this method, a constant current (i) is applied to the cell and the voltage function of time is measured. From this experiment, one can obtain the specific capacity of the cell which is the total amount of charge passed through an electrode in a set-up period (t) per unit mass (m), as shown in Equation 2.24.

$$C = \frac{I*t}{m}$$
(2.24)

The galvanostatic techniques of a constant current are applied to an electrochemical cell, and the resulting potential is measured over time. This allows for the determination of various electrochemical parameters such as charge transfer kinetics, electrode surface area, and electrochemical reaction mechanisms. Here, a short current pulse between t_o and t_1 is

applied and the potential response is monitored. This is shown schematically in Figure 2.9. From the potential response, a cell resistance (R) can be obtained as shown in Equation 2.25.

$$R = \frac{V_{to} - V_{t1}}{I_{to} - I_{t1}} \qquad (2.25)$$
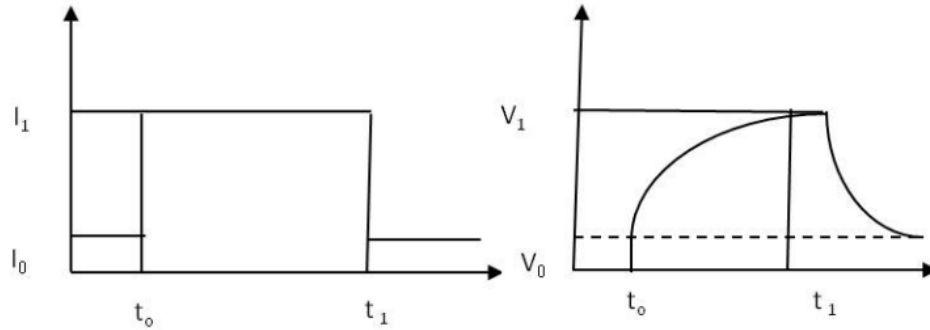
Figure 2.9. Schematic representation of the potential response to a current pulse.

References

[1] Y. Lin, X. Han, C.J. Campbell, J.-W. Kim, B. Zhao, W. Luo, J. Dai, L. Hu, J.W. Connell, Holey Graphene Nanomanufacturing: Structure, Composition, and Electrochemical Properties, Advanced Functional Materials 25(19) (2015) 2920-2927.

[2] Y. Leng, X-Ray Diffraction Methods, (2008).

[3] A. Ali, Y.W. Chiang, R.M. Santos, X-ray Diffraction Techniques for Mineral Characterization: A Review for Engineers of the Fundamentals, Applications, and Research Directions, Minerals 12(2) (2022).

[4] A.L. RYLAND, X-ray diffraction Journal of chemical education (1958).

[5] P.W. Stephens, Phenomenological Model of Anisotropic Peak Broadening in Powder Diffraction, Journal of Applied Crystallography 32 (1999) 281-289.

[6] J. Epp, X-ray diffraction (XRD) techniques for materials characterization, Materials Characterization Using Nondestructive Evaluation (NDE) Methods2016, pp. 81-124.

[7] Y.P.a.B.D. VD Mote, Williamson-Hall Analysis in Estimation of Lattice Strain in Nanometer-Sized ZnO Particles, Journal of Theoretical and Applied Physics (2012).

[8] Y.T. Prabhu, K.V. Rao, V.S.S. Kumar, B.S. Kumari, X-Ray Analysis by Williamson-Hall and Size-Strain Plot Methods of ZnO Nanoparticles with Fuel Variation, World Journal of Nano Science and Engineering 04(01) (2014) 21-28.

[9] F. Bhadala, L. Suthar, P. Kumari, M. Roy, Rietveld refinement, morphological, vibrational, Raman, optical and electrical properties of Ca/Mn co-doped $BiFeO_3$, Materials Chemistry and Physics 247 (2020).

[10] F. Sun, Y.S. Yin, Rietveld Refinement of the $BaTiO_3$ from X-ray Powder Diffraction, Advanced Materials Research 79-82 (2009) 593-596.

[11] B. Thrope, A.R. Ferreira Lima, A.H. Pinto, From the Periodic Properties of Metals to the Rietveld Refinement of the Pharmaceutical Molecule Naproxen: Three Remote Experiments about X-ray Diffraction, Journal of Chemical Education 99(5) (2022) 2055-2066.

[12] J.S.O. Evans, I.R. Evans, Structure Analysis from Powder Diffraction Data: Rietveld Refinement in Excel, Journal of Chemical Education 98(2) (2020) 495-505.

[13] M. Spiliopoulou, D.-P. Triandafillidis, A. Valmas, C. Kosinas, A.N. Fitch, R.B. Von Dreele, I. Margiolaki, Rietveld Refinement for Macromolecular Powder Diffraction, Crystal Growth & Design 20(12) (2020) 8101-8123.

[14] U.A.J.a.R.D. Jenkins., Introduction to Raman Spectroscopy Springer (2002.) 77–104.

[15] R.F. Stamm, Raman Spectroscopy, American Chemical Society (26,1) (1954) 49–53.

[16] P.D. RS Katiyar, MM Hargreave, GR Wilkinson, Dynamics of the rutile structure. III. Lattice dynamics, infrared and Raman spectra of $SnO2$, 4 (1971) 2421.

[17] G.L. Yuan, S.W. Or, H.L.W. Chan, Raman scattering spectra and ferroelectric properties of $Bi1-xNdxFeO3$ (x=0–0.2) multiferroic ceramics, Journal of Applied Physics 101(6) (2007).

[18] Y.C. Cho, S.I. Ahn, Fabricating a Raman spectrometer using an optical pickup unit and pulsed power, Sci Rep 10(1) (2020) 11692.

[19] E. Fernandez-Segura, A. Warley, Electron probe X-ray microanalysis for the study of cell physiology, Methods Cell Biol 88 (2008) 19-43.

[20] D.D. Macdonald, Reflections on the history of electrochemical impedance spectroscopy, Electrochimica Acta 51(8-9) (2006) 1376-1388.

[21] X. Qiu, Q. Hua, L. Zheng, Z. Dai, Study of the discharge/charge process of lithium-sulfur batteries by electrochemical impedance spectroscopy, RSC Adv 10(9) (2020) 5283-5293.

[22] N.S. Zhai, M.W. Li, W.L. Wang, D.L. Zhang, D.G. Xu, The Application of the EIS in Li-ion Batteries Measurement, Journal of Physics: Conference Series 48 (2006) 1157-1161.

[23] F. Huet, A review of impedance measurements for determination of the state-of-charge or state-of-health of secondary batteries Journal of Power Sources 70 (1998) 59-69.

[24] L.A. Middlemiss, A.J.R. Rennie, R. Sayers, A.R. West, Characterisation of batteries by electrochemical impedance spectroscopy, Energy Reports 6 (2020) 232-241.

[25] P. Vadhva, J. Hu, M.J. Johnson, R. Stocker, M. Braglia, D.J.L. Brett, A.J.E. Rettie, Electrochemical Impedance Spectroscopy for All-Solid-State Batteries: Theory, Methods and Future Outlook, ChemElectroChem 8(11) (2021) 1930-1947.

[26] S. Dhillon, R. Kant, Theory for electrochemical impedance spectroscopy of heterogeneous electrode with distributed capacitance and charge transfer resistance, Journal of Chemical Sciences 129(8) (2017) 1277-1292.

[27] T.Q. Nguyen, C. Breitkopf, Determination of Diffusion Coefficients Using Impedance Spectroscopy Data, Journal of The Electrochemical Society 165(14) (2018) E826-E831.

[28] M. Gaberšček, Impedance spectroscopy of battery cells: Theory versus experiment, Current Opinion in Electrochemistry 32 (2022).

[29] M. Gaberscek, Understanding Li-based battery materials via electrochemical impedance spectroscopy, Nat Commun 12(1) (2021) 6513.

[30] M. Victoria, K. Zhu, T. Brown, G.B. Andresen, M. Greiner, The role of storage technologies throughout the decarbonisation of the sector-coupled European energy system, Energy Conversion and Management 201 (2019).

[31] J. Liu, C. Hu, A. Kimber, Z. Wang, Uses, Cost-Benefit Analysis, and Markets of Energy Storage Systems for Electric Grid Applications, Journal of Energy Storage 32 (2020).

Chapter 3

Holey Graphene/Ferroelectric/Sulfur Composite Cathodes for High-Capacity Lithium−Sulfur Batteries

3.1 Introduction

The emerging markets for portable electronics, electric vehicles, and grid-level energy storage system demand next-generation rechargeable batteries with high energy density and low costs [1]. Among them, lithium–sulfur (Li–S) batteries discovered in the 1960s [2], have received significant attention because of the unprecedented theoretical capacity of elemental sulfur (S_8), high specific energy density, and low material cost [3]. Sulfur is low-cost, environment-friendly, naturally abundant, and non-toxic. These superior properties position Li−S batteries to be considered for the next-generation energy source for portable electronic devices [4]. The research on Li-S batteries is promising, since it has a high theoretical gravimetric energy density of 2600 Wh/kg, compared to the energy density of lithium-ion batteries (LIBs) which is lower than 200 Wh/kg [5]. In addition, S cathodes have a high theoretical capacity of 1675 mAh/g_s, versus 300 mAh/g in typical cathodes for LIBs [6]. The Li metal anode has a large capacity of 3860 mAh/g [7, 8]. The conventional method of Li-S batteries cathode fabrication consists of mixing the active material with carbon black plus polyvinylidene fluoride (PVDF) as the binder, followed by using an organic solvent such as N-methyl-2-pyrrolidone (NMP) to form a slurry, which is then coated on aluminum foil and allowed to dry for solvent evaporation. Next, the cathodes are cut into disc shapes, with typical S mass loadings < 2 mg$_s$/cm^2 [9, 10]. Several

methods have been investigated using holey graphene (hG) as an electrode material for electrochemical energy storage applications because the through-thickness holes facilitate ion transport across the nanosheet planes, a feature that is not attainable with intact graphene. In S/hG composite cathode, holey graphene has the higher mechanical strength which has been mentioned in several reports [11]. Although in the present manuscript the mechanical character of holey graphene has not been measured, based on the literature, it can be assumed that this special character of holey graphene controls the volume expansion of cathode during charge and discharge cycle. Another outstanding attribute of hG is that it can be directly molded into architectures of arbitrary shapes [12, 13]. The presence of holes through the graphene sheets enables molding into appropriate shapes. For example, high-mass loading S composite cathodes were obtained with hG as a host matrix and conductive scaffold [11]. In addition, ion transport is facilitated by the presence of holes on the graphene sheet, enabling efficient electrochemical processes [14]. However, Li−S batteries usually face the challenges of the poor electronic conductivity of insulated sulfur, the dramatic volume change of about 80% during cycling, and the shuttle effect induced by soluble lithium polysulfides (Li_2S_x, $4 < x < 8$). So far, many strategies have been applied to deal with these deficiencies. Further, multiple fabrication-related problems such as non-uniform coatings and cracks are typically encountered when using conventional slurry-based electrode fabrication methods, particularly when trying to achieve high S content and low electrolyte/sulfur (E/S) ratios. Dry compressibility of hG enabled electrodes support ultrahigh mass loadings and high performance. For example, ultrahigh mass loading selenium cathodes (15.6 mg/cm^2; hG/Se-90%) were used in lithium-selenium batteries that displayed high areal capacity (8.7 mAh/cm^2; hG/Se-90%) with the first

discharge capacity around 574 mAh/g$_s$ and utilization of ~85% [15]. Lithium-ion battery electrodes with hG:LFP (lithium iron phosphate) were fabricated by using binder-free dry processing at 20 MPa for only 10 sec, and they exhibited a capacity retention within experimental error and reach >160 mAh/g for at least the first 10 cycles [16]. For hG/S-50% high mass loading Li-S batteries cathodes, it was found that the first discharge capacity reached was as high as 1429 mAh/g$_s$, 8.2 mAh/cm^2 and utilization of ~85% at 0.5 mA/cm^2 [11]. Barium titanate BaTiO$_3$ (BTO), one of the most important and widely used ferroelectric materials, was introduced into the cathode, for the first time in 2016, as a proof-of-concept to demonstrate the novel polysulfide reduction strategy for stabilizing the Li–S batteries. It was found that by mixing the BTO nanoparticles with the cathode materials, the heteropolar polysulfides can be anchored in the cathode due to the internal electric field originating from the spontaneous polarization of BTO nanoparticles. A discharge capacity of 835 mAh/g after 100 cycles was obtained for the cathodes with BTO nanopaticles added, two times more than cathode without BTO nanoparticles [17]. The incorporation of BTO particles into the poly(ethylene) separator in Li-S batteries was also explored; the permanent dipoles that are formed in the BTO nanoparticles upon the application of an electric field can effectively reject polysulfide from passing through the separator via electrostatic repulsion, resulting in significantly improved cyclability. In addition, the coated BTO particles improve the thermal response of poly(ethylene) separator. In this way, Li-S cell exhibited a significantly enhanced cycling performance of 82.8% retention after 50 cycles and improvement in safety [18]. The addition of BTO particles combined with a very thin protective layer of TiO$_2$ (CSB@TiO$_2$) was used as cathode for sodium-sulfur batteries. Results show that such cathode material exhibits high-

rate capability and excellent durability compared with pure C/S and C/S/BaTiO$_3$ electrodes. For cycling performance, this CSB@TiO$_2$ electrode exhibited discharge capacity of 611 mAh/g after 400 cycles at 0.5 A/g, compared with 340 mAh/g and 459 mAh/g of C/S and C/S/BTO electrodes respectively. Such superior electrochemical performance was mainly attributed to the "BaTiO$_3$-C-TiO$_2$" synergetic structure within the matrix, which enables effectively inhibiting the shuttle effect, restraining the volumetric variation and stabilizing the ionic transport interface [19]. Another reported approach to reduce the polysulfide shuttle effect is using a carbon nanotube sheet distributing homogeneously BaTiO$_3$ as a pseudo current collector between the cathode and separator in Li-S batteries. The coin cell utilizing a ferroelectricity embedded interlayer exhibits a higher capacity of 908 mAh/g at 0.2C than that of carbon alone of 740 mAh/g at 200th cycle; this result corresponds to a capacity retention ratio enhancement from 67.5% to 75.6%. Also, it was reported that the retention of the Coulombic efficiency is effectively maintained in long cycles at 0.5C (94.5%–99.6%). The modified interlayer functions as an effective current collector due to the high affinity of the ferroelectric material to polysulfide, plus the ferroelectricity in the interlayer acts as a polysulfide anchor [20].

To meet the theoretical energy density and areal capacity of Li-S batteries, a high sulfur loading is required [8, 21, 22]. Particular attention on the progress of cathode, anode, separator, and electrolyte on a single platform toward achieving high areal capacity and long-term cycling is missing. This challenge has motivated the authors to test high mass loading sulfur cathodes with ferroelectric materials different from BTO and following a different method for cathode fabrication. Bismuth ferrite BiFeO$_3$ (BFO) is one of the most studied multiferroic materials [23, 24]. It exhibits both antiferromagnetic and ferroelectric

properties at room temperature. These properties offer alternatives for industrial and technological applications, such as its application in Li-S battery cathodes for improving specific capacity and reversibility. Our group recently reported composite electrodes of $BFO_xS_{1-x}C_{10}$ prepared by mixing the 5 wt% PVDF and NMP as a solvent for 12 hrs. at 400 rpm. The $S_{60}BFO_{30}C_{10}$ composite Li-S battery cathode capacity was as high as ~1600 mAh/g, and the cell reached 30 cycles [25].

In this study, we report the investigation of high mass loading sulfur composite cathodes for Li-S batteries. The composites were formed starting with $S_{50}hG_{50}$ and adding 5% of FNPs ($S_{47.5}FNPs_5hG_{47.5}$), where hG is the electrically conducting scaffold and the ferroelectric nanoparticles (FNPs) are BTO, BFO, $Bi_4NdTi_3Fe_{0.7}Ni_{0.3}O_{15}$ (BNTFN), $Bi_4NdTi_3Fe_{0.5}Co_{0.5}O_{15}$ (BNTFC). The cathodes were fabricated using a novel method consisting of dry pressed of S/FNPs/hG without binder and solvent. This method allows us to obtain electrodes with high mass loading and avoid using toxic solvents. The results showed high specific capacity, high areal capacity, and high mass loading in the coin cells.

3.2 Experimental details

The hG was prepared from graphene (Vorbeck materials) using the established one-step air oxidation procedure reported previously [26]. Bis(trifluoromethylsulfonyl)imide lithium salt (LiTFSI; 98+%), lithium nitrate ($LiNO_3$; 99.999%), 1,2-dimethoxyethane (DME; 99+%), and 1,3-dioxolane (DOL; 99.5%) were purchased from Thermo Fisher[*1]. Sulfur (S; 99.998%), highly pure barium carbonate ($BaCO_3$; 99.8%), high purity neodymium (III) oxide (Nd_2O_3; 99.9%), lithium foil 0.75 mm thick x 19 mm wide (Al; 99.9 %), and high

purity cobalt (II, III) oxide (Co_3O_4; 99.998 %) were purchased from Alfa Aesar[*1]. Iron oxide (Fe_2O_3; 99.998%), nickel (III) oxide nano-powder (Ni_2O_3; 99%), and Celgard membrane 25 µm thickness and 85 mm width was purchased from Sigma-Aldrich[*1]. High-purity bismuth oxide (Bi_2O_3; 99.9%) was purchased from Fluka[*1], and titanium dioxide (TiO_2; 97%) was purchased from Fisher Scientific[*1]. All chemical materials for battery assembly were handled inside an Ar-filled glove box with water (H_2O), and oxygen (O_2) contents < 0.5 ppm.

The synthesis of FNPs was done by mechanical activation followed by thermal treatment. Stoichiometric amounts of 15 wt% excess of Bi_2O_3 were used to compensate volatilization loss during the thermal treatment. The oxides were mixed with isopropanol using a high-energy ball-milling planetary machine with zirconia balls (Across International, PQ-N04 planetary ball mill, USA) operating at 45 Hz (2700 rpm) for 8 hrs. The synthesized material was dried on a hot plate at 100 °C for 8 hrs. We used a furnace (Carbolite, HTF1700, USA) at a heating and cooling rate of 5 °C/min in which the powders were calcined. Calcination parameters like temperature and duration were applied, as mentioned in Table 3.1. Ferroelectric nanoparticles synthesis process is shown in Figure 3.1.

Table 3.1. Calcination conditions of the ferroelectric nanoparticles' precursor powders.

Ferroelectric Nanoparticles (FNPs)	Precursor Type	Calcination Temperature [°C]	Calcination Time [hrs.]
BaTiO$_3$	BaCO$_3$ and TiO$_2$	1200	10
BiFeO$_3$	Bi$_2$O$_3$ and Fe$_2$O$_3$	875	10
Bi$_4$NdTi$_3$Fe$_{0.7}$Ni$_{0.3}$O$_{15}$	Bi$_2$O$_3$, Fe$_2$O$_3$, TiO$_2$, Ni$_2$O$_3$ and Nd$_2$O$_3$	800	15
Bi$_4$NdTi$_3$Fe$_{0.5}$Co$_{0.5}$O$_{15}$	Bi$_2$O$_3$, Fe$_2$O$_3$, TiO$_2$, Co$_3$O$_4$ and Nd$_2$O$_3$	800	15

[*1] Specific vendor and manufacturer names are explicitly mentioned only to accurately describe the material or test hardware. The use of vendor and manufacturer names does not imply an endorsement by the authors, nor does it imply that the specified material or equipment is the best available.
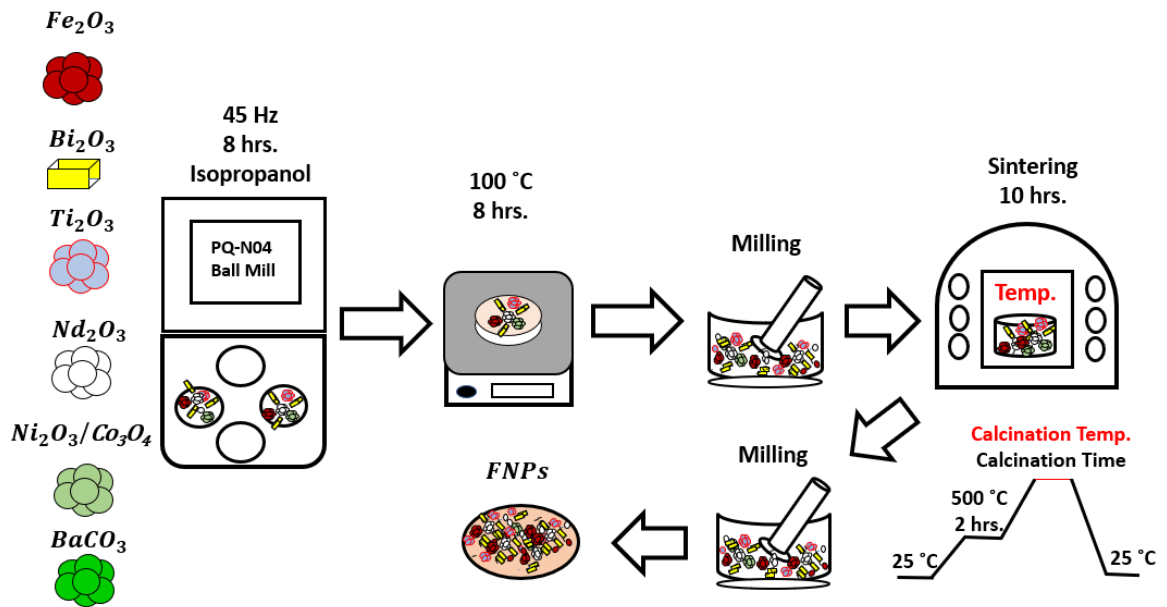
Figure 3.1. Schematic illustration of ferroelectric nanoparticles synthesis process.

Sulfur-FNPs-hG composite cathode preparation. The hG was used as dry pressable, solvent-free, and binder-free process to prepare five component powders. The sulfur, hG and ferroelectric nanoparticles were mixed in a particular ratio by ball milling for ~10 sec. The composites powders were mixed as follows: $S_{50}hG_{50}$ and $S_{47.5}(FNPs)_5hG_{47.5}$ (subscripts indicate the relative weight percentages of the components). Afterward, the electrodes were fabricated by dry pressing the powders on a stainless-steel die (13 mm diameter) and hydraulic press at 200 mbar sandwiched between aluminum foil. The product is a dense electrode that may be directly used as the composite cathode when assembling the coin cells (CR2032). This technique facilitates preparation and is less time consuming than conventional solvent-based methods. The S cathodes preparation described in the previous paragraph is illustrated in Figure 3.2. On the left side, the $S_{50}hG_{50}$ electrode with active sulfur mass loading of 6.06 mg_s/cm^2, and on the right-side $S_{47.5}(FNPs)_5hG_{47.5}$

cathodes with active sulfur mass loading ranging from 5.72 mg$_s$/cm^2 to 7.01 mg$_s$/cm^2 are shown.
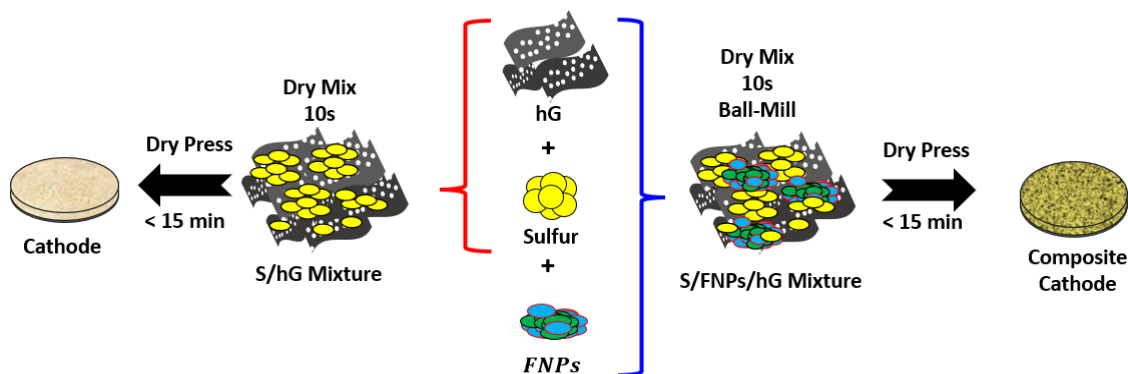
Figure 3.2. Schematic illustration of the solvent-free mix and press process for the preparation of S/hG (left) and S/FNPs/hG composite cathodes (right).

Coin cell fabrication. The coin cells CR2032 were assembled in an Ar-filled glove box (MBraun, USA) with H$_2$O, O$_2$ contents < 0.5 ppm using composite cathode S50hG50 and composite cathode S$_{47.5}$(FNPs)$_5$hG$_{47.5}$ (13 mm), polypropylene membrane (16 mm; Celgard-2400) as separator, and lithium foil (12 mm) as anode. The salt mixture of 1M LiTFSI and 0.2M LiNO$_3$ was dissolved in DOL and DME in an equal volume ratio (1:1, v/v) and used as electrolyte.

Characterizations. Powder X-ray Diffraction (XRD) patterns were collected by powder diffractometer by using a Smart Lab Rigaku system with CuKα as radiation source of wavelength (λ=1.5406 Å), operating in a Bragg angle (2θ) ranging from 20˚ to 80˚ and working conditions of 40 KV and 44 mA. The micrographs and the energy dispersive X-ray spectroscopy (EDS, JEOL, JSM 648oLV, Peabody, USA) spectra were used to identify the chemical composition of the cathode material with accuracy. Field emission scanning electron microscope (SEM, JEOL, JSM-6480LV, USA) operated at

15 KV was used to study the surface morphology of the electrodes. Raman spectroscopy was performed by a micro-Raman system (Thermo Scientific DXR, Waltham, MA, USA) with a 532 nm laser as excitation source at room temperature. Galvanostatic discharge-charge curves were measured using an 8-channel battery analyzer (BST8-CST, MTI Corporation, USA) and 32-channel battery tester (Arbin Instruments, Mits Pro8.0, USA) at different current densities and were calculated according to the area of cathode 1.327 cm^2 and range from 0.2 mA/cm^2 to 0.5 mA/cm^2. In this work, the voltage range used was 1.6 – 2.8 V (Vs Li$^+$/Li). Electrochemical impedance spectroscopy (EIS) was measured at the open circuit potential in the frequency range of 1 MHz to 0.1 Hz with amplitude of 10 mV and 10 points measured per decade.

3.3 Results and discussion
3.3.1 X-ray diffraction

XRD spectra of the pristine and modified composites are shown in Figure 3.3. The composites were fabricated using hG, sulfur, and ferroelectric nanoparticles, namely, bismuth ferrite (BTO), barium titanate (BTO), Bi$_4$NdTi$_3$Fe$_{0.7}$Ni$_{0.3}$O$_{15}$ (BNTFN), and Bi$_4$NdTi$_3$Fe$_{0.5}$Co$_{0.5}$O$_{15}$ (BNTFC). The pristine S features typical diffraction peaks which are consistent with the *Fddd* orthorhombic phase of sulfur data of (JCPDS No. 08–0247) [27] as shown in Figure 3.3a. The diffraction peak at 2θ = 20° − 30° could be ascribed to the overlapping of graphene characteristic peak ~26° with a Miller index (002) corresponding to some graphitic carbon regions (PDF 00-001-0640) [16] present within the hG powder as shown in Figure 3.3b. From the XRD patterns, it is observed that no new phase has been formed in the S/FNPs/hG composite during the synthesis process. In addition, XRD patterns of BFO, BTO, BNTFN, and BNTFC confirmed the formation of

the perovskite structure. The BFO was verified against the powder data of JCPDS No. 86-1518 [28]. These peaks revealed that BFO crystallites had the perovskite structure with rhombohedral space group $R3c$ (no. 161) as show in Figure 3.3c. The BTO compound exhibited (002)/(200) peaks splitting of the diffraction lines around 2θ of 45°, pointing to tetragonal phase. The intensity ratios of the modeled peaks were compared to the values given in the JCPDS file No. 05-0626 [29] as shown in Figure 3.3d. The compounds of $Bi_4NdTi_3Fe_{0.7}Ni_{0.3}O_{15}$ [30] and $Bi_4NdTi_3Fe_{0.5}Co_{0.5}O_{15}$ [31] exhibited layered Aurivillius phase containing four perovskite layers; both have an orthorhombic phase as shown in Figure 3.3(e-f). The XRD patterns of composite electrodes (Figure 3.3(g-k)) shows the characteristic peaks of the mixed materials.
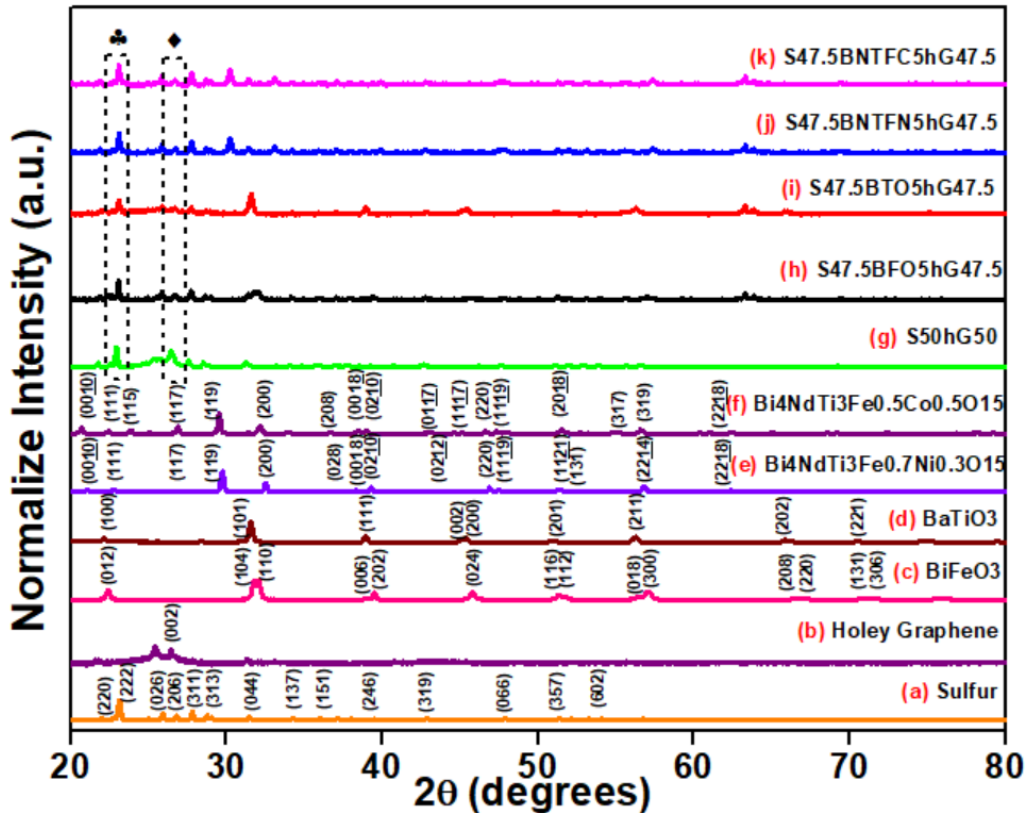
Figure 3.3. XRD spectra of (a) sulfur powder (♣), (b) hG (♦), (c) bismuth ferrite $BiFeO_3$, (d) barium titanate $BaTiO_3$, (e) $Bi_4NdTi_3Fe_{0.7}Ni_{0.3}O_{15}$, (f) $Bi_4NdTi_3Fe_{0.5}Co_{0.5}O_{15}$, (g)

$S_{50}hG_{50}$, (h) $S_{47.5}(BFO)_5hG_{47.5}$, (i) $S_{47.5}(BTO)_5hG_{47.5}$, (j) $S_{47.5}(BNTFN)_5hG_{47.5}$, and (k) $S_{47.5}(BNTFC)_5hG_{47.5}$ composites.

The crystallite size of the individual materials was calculated by Williamson-Hall method using the standard Scherrer's Equation 3.1:[32]

$$D = \frac{K\lambda}{\beta Cos\theta} \qquad (3.1)$$

where D is the crystallite size (nm), K is the Scherer constant (0.9), λ is the wavelength of the X-ray radiation CuK_α (1.5406 Å), and β is the full width at half maximum (FWHM) of the peaks, and θ is the Bragg's angle. Table 3.2. summarizes the calculated crystallite size.

Table 3.2. Crystallite size, from Scherrer equation.

S.N.	Precursors	Crystallite Size (D)[nm]
1	Sulfur	62.9
2	Holey Graphene	14.5
3	$BiFeO_3$	24.5
4	$BaTiO_3$	32.2
5	$Bi_4NdTi_3Fe_{0.7}Ni_{0.3}O_{15}$	65.5
6	$Bi_4NdTi_3Fe_{0.5}Co_{0.5}O_{15}$	72.4

3.3.2 Raman spectroscopy

The Raman spectra of hG and S/FNPs/hG composites are shown in Figure 3.4. As shown in the spectra, there are two major peaks at 1430 cm^{-1} and 1590 cm^{-1} corresponding to the D band (disorder-induced phonon mode) and G band (graphitic band), suggesting a disordered graphene like framework [33]. The Raman peaks for 2D and D+G are also visible around 2700 cm^{-1} and were attributed to layered structure of graphene. The intensity as well as in the ratio of I_D/I_G phonon peaks stay similar, depicting the presence of FNPs in the composites.
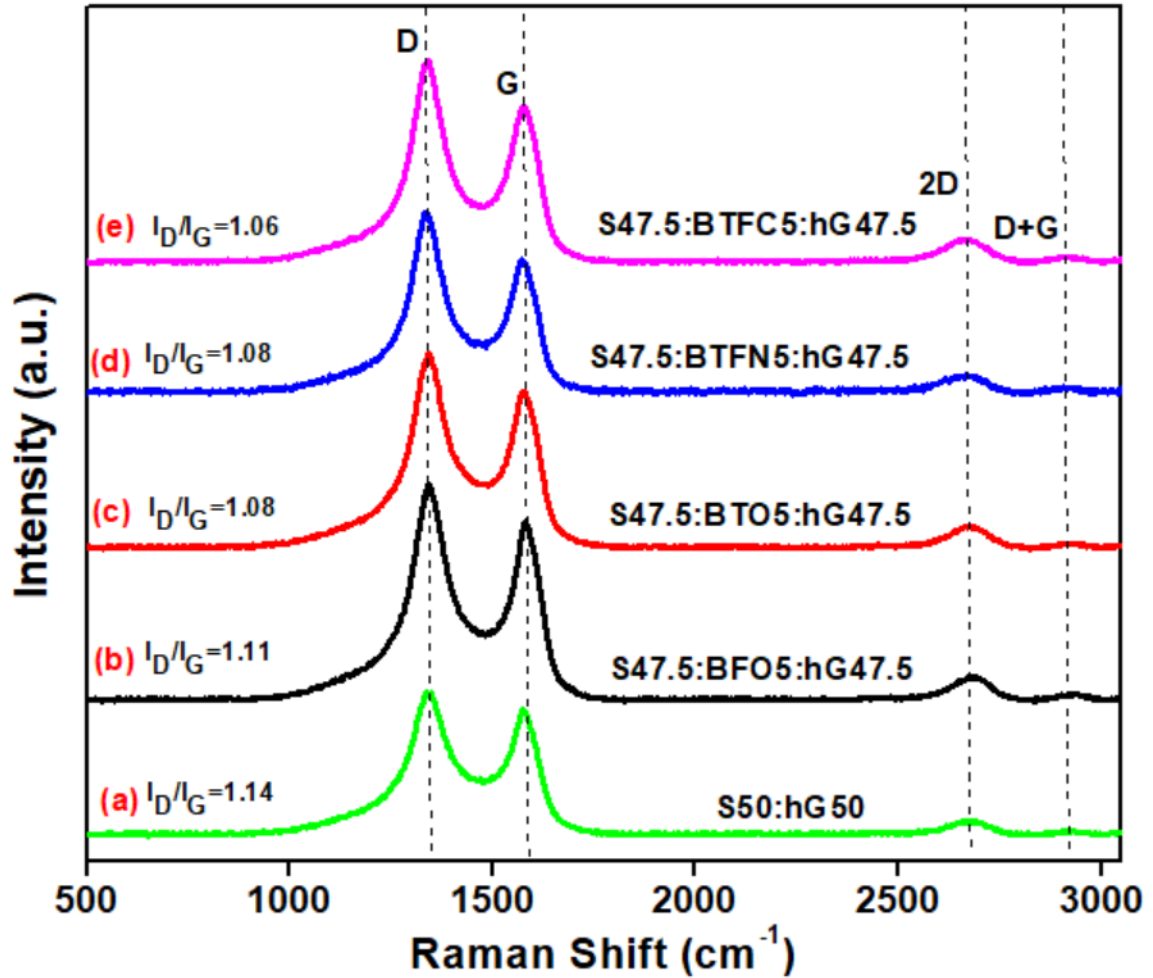
Figure 3.4. Raman spectra of (a) $S_{50}hG_{50}$, (b) $S_{47.5}(BFO)_5hG_{47.5}$, (c) $S_{47.5}(BTO)_5hG_{47.5}$, (d) $S_{47.5}(BNTFN)_5hG_{47.5}$, and (e) $S_{47.5}(BNTFC)_5hG_{47.5}$ cathodes composites.

3.3.3 Ferroelectric polarization measurement

The measured ferroelectric polarization (P-E) hysteresis loops for $BiFeO_3$, $BaTiO_3$, $Bi_4NdTi_3Fe_{0.7}Ni_{0.3}O_{15}$, and $Bi_4NdTi_3Fe_{0.5}Co_{0.5}O_{15}$ ferroelectric nanoparticles are shown in Figure 3.5(a-d), respectively. All these systems show ferroelectric polarization characteristics. The remnant polarization (P_r) for BFO at 3 kV/cm is approximately 8.5 $\mu C/cm^2$ and 8.0 $\mu C/cm^2$ for BTO, while BNTFN and BNTFC compounds have smaller P_r, although a less leaky hysteresis loop than BFO. BTO is a well-known displacive

ferroelectric with a well-behaved hysteresis loop. Since spontaneous polarization is key for reducing polysulfide shuttle effect, BTO turns out to be the obvious choice to investigate the incorporation of ferroelectric materials into battery components. For BTO, it has been proved that the existence of an internal field contributes to reducing the polysulfides formation during discharge-charge of Li-S batteries. On the other hand, BFO, BNTFN and BNTFC are multiferroic compounds at room temperature. BFO is ferroelectric and antiferromagnetic [28] while BNTFN and BNTFC are both ferroelectric and ferromagnetic [30, 31]. Since ferroelectricity and magnetic ordering are correlated phenomena in multiferroic materials, it is worthy to investigate the introduction of this kind of material into battery elements and their effect on the electrochemical performance.
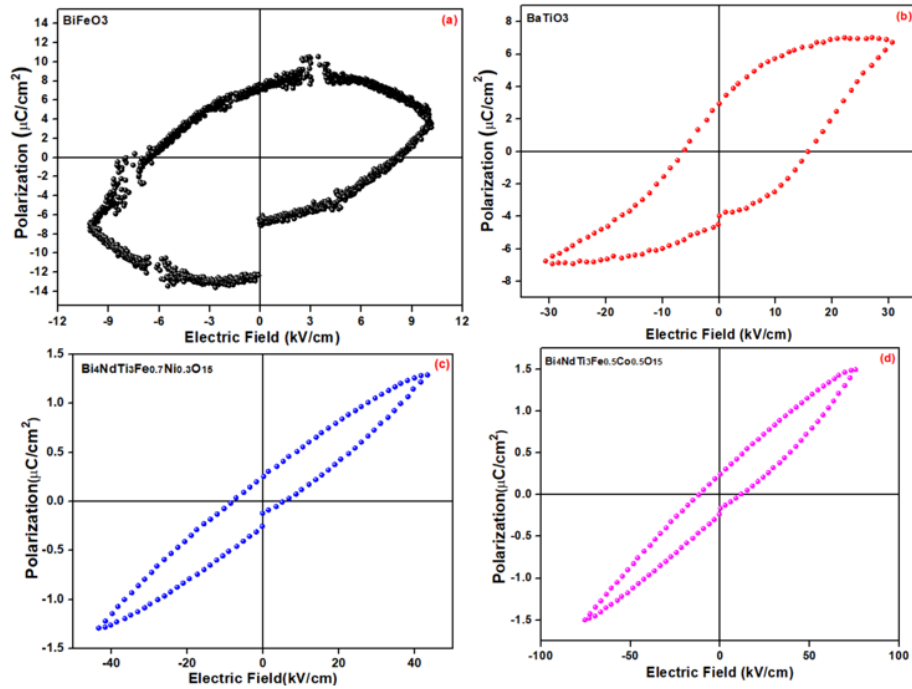
Figure 3.5. Ferroelectric hysteresis loops of (a) $BiFeO_3$, (b) $BaTiO_3$, (c) $Bi_4NdTi_3Fe_{0.7}Ni_{0.3}O_{15}$, and (d) $Bi_4NdTi_3Fe_{0.5}Co_{0.5}O_{15}$ compounds.

3.3.4 SEM and EDS measurements

The SEM images of S/hG are shown in Figure 3.6(a-e) as well as various S/FNPs/hG composites respectively. FNPs were attached to the hG-S composite surface, which is relatively smooth. It has been observed that hG and FNPs are uniformly distributed within the surface of composites, in which hG effectively provides the conductive path for sulfur, and it might block the diffusion of polysulfides.
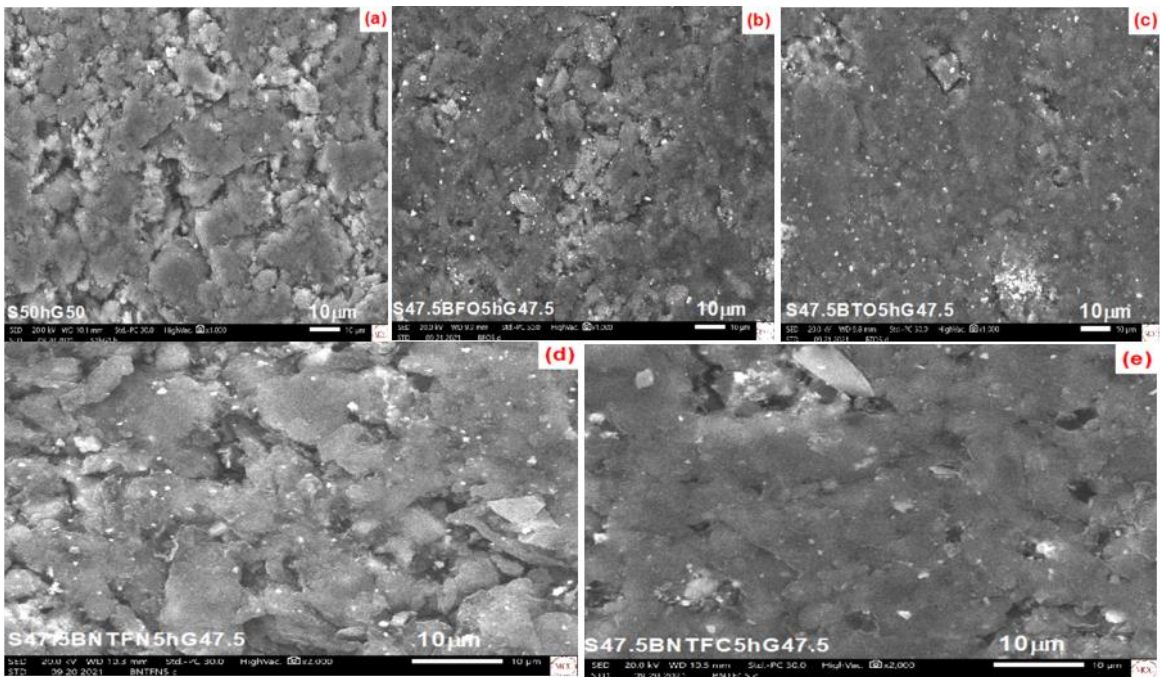
Figure 3.6. SEM images of (a) $S_{50}hG_{50}$, (b) $S_{47.5}(BFO)_5hG_{47.5}$, (c) $S_{47.5}(BTO)_5hG_{47.5}$, (d) $S_{47.5}(BNTFN)_5hG_{47.5}$, and (e) $S_{47.5}(BNTFC)_5hG_{47.5}$ cathodes composites.

The EDS spectra of S/hG and S/FNPs/hG composites is shown in Figure 3.7. In each spectrum the S-peak is dominant due to its higher concentration relative to the hG, $BiFeO_3$, $BaTiO_3$, $Bi_4NdTi_3Fe_{0.7}Ni_{0.3}O_{15}$, and $Bi_4NdTi_3Fe_{0.5}Co_{0.5}O_{15}$ peaks.
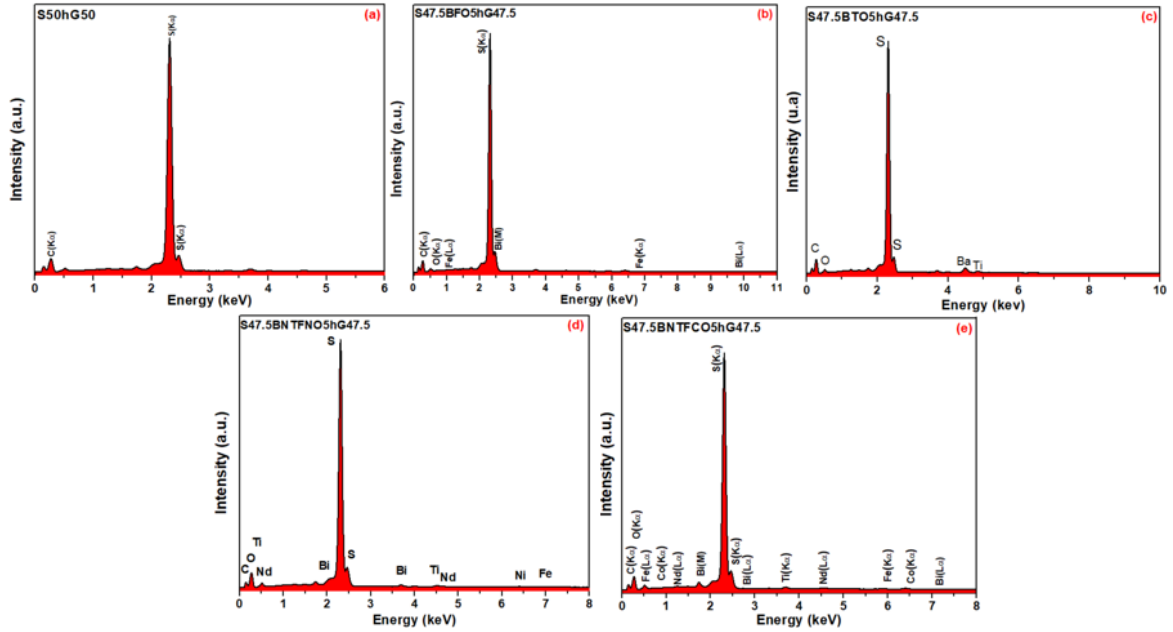
Figure 3.7. EDS spectra of (a) $S_{50}hG_{50}$, (b) $S_{47.5}(BFO)_5hG_{47.5}$, (c) $S_{47.5}(BTO)_5hG_{47.5}$, (d) $S_{47.5}(BNTFN)_5hG_{47.5}$, and (e) $S_{47.5}(BNTFC)_5hG_{47.5}$ cathodes composites.

3.3.5 Electrochemical impedance spectra

The electrochemical impedance spectra (EIS) before charge-discharge for all S/hG and S/FNPs/hG composite electrodes were analyzed by parameter optimization of each element on the selected equivalent circuit model using EIS software (Z-SimpWin3.21) to explore the role of charge transfer processes in the batteries. The impedance spectra comprised a semicircle at the high frequency and a slope at the low frequency. R_s corresponds to the distance between the left-side semicircle edge and the imaginary part axis, which was attributed to the electrolyte solution resistance within the cell and the intrinsic resistance, including the contact resistance and the resistance within the active materials. The Randles circuit model was used to determine the net impedance and simulation diagram for all the systems, as shown in Figure 3.8. The semicircle along the real part of the axis represents the Rct value; however, slope at the low frequency was related to diffusion, electrically

represented by W_{sc} [33, 34]. The resistances of charge transfer (R_{ct}) were calculated as 73.5 Ω and 13.81 Ω for S/hG and S/FNPs/hG respectively as shown in Figure 6. To study the kinetics of S/hG and S/FNPs/hG composite electrodes, Li^+ diffusion coefficients (D_{Li}) were calculated according to the impedance spectroscopy results [32]. The D_{Li} of S/FNPs/hG composite can be calculated by the diffusion length (l_D) and diffusion time constant (τ_s) as shown in Equation 3.2 [33]:

$$D_{Li} = \frac{l_D^2}{\tau_s}, \qquad (3.2)$$

and the diffusion length is based on the Equations 3.3-3.6

$$l_D = \sqrt{(\tau_s \ x \ D_m)} \qquad (3.3)$$

$$D_m = \frac{\lambda_D^2}{\tau_1} \qquad (3.4)$$

$$\lambda_D = d/\delta \qquad (3.5)$$

$$tan(\phi)_{max} = \sqrt{\delta/2} \qquad (3.6)$$

in which D_m and λ_D are the diffusion coefficient of net mobility, the Debye length of the electrode, respectively, δ is a dimensionless number, and τ_1 is the reciprocal of the frequency corresponding to the inflection point of the Nyquist plot (Figure 3.8b) [34], τ_s is the reciprocal of the frequency corresponding to the highest point in the Bode plot (Figure 3.8c), $tan(\phi)_{max}$ can be obtained from loss tangent plot (Figure 3.8d), d is the half thickness of the electrode, and W_{sc} is a part of the Warburg element, which can be extracted from the simulated equivalent circuit. Similarly, the τ_1, τ_s, $tan(\phi)_{max}$ and W_{sc} of S/hG and S/FNPs/hG composites can be obtained from the Nyquist plot, Bode Plot, loss tangent plot and simulated equivalent circuit diagram, respectively. The values of D_{Li} for S/hG and S/FNPs/hG ranging from 1.18×10^{-12} cm^2/s to 6.61×10^{-10} cm^2/s might result in good ionic

conduction and better rate performance as shown in Table 3.3. The various parameters as

shown in Table 3.3. such as solution resistance (R_s), charge transfer resistance (R_{ct}), double

layer capacitance (C) and Warburg element (W) are obtained by following R(CR)W model

for the composite electrodes. In addition, the Nyquist plot from electrochemical impedance

spectroscopy measurement showed both the solution resistance (R_s, the intercept of x-axis)

and the transfer resistance (R_{ct}, the size of semicircle) [24]. In comparison to S/hG and

S/FNPs/hG electrodes as a shown in Figure 3.8a, the batteries with ferroelectric material

exhibited a low internal resistance of 8.24 Ω, 2.34 Ω, 3.66 Ω, and 2.60 Ω for S/BFO/hG,

S/BTO/hG, S/BNTFN/hG, and S/BNTFC/hG, correspondingly and a low charge transfer

resistance of 14.51 Ω, 13.84 Ω, 15.80 Ω, and 17.21 Ω as shown in Table 3.3. The Li-S

battery with S/hG shows a low internal resistance of ~13 Ω and a charge transfer resistance

of ~77 Ω.

Table 3.3. Representation of calculated EIS parameters with R(CR)W model.

Electrodes	$R_s[\Omega]$	C	$R_{ct}\ [\Omega]$	W_{sc}	$D_{li}[cm^2/s]$
S/hG	13.45	1.36×10^{-6}	77.14	0.0815	1.18×10^{-12}
S/BFO/hG	8.24	20.54	14.51	1.04×10^4	5.47×10^{-11}
S/BTO/hG	2.34	5.37	13.84	2.25×10^8	4.55×10^{-11}
S/BNTFN/hG	3.66	2.99×10^{-8}	15.80	0.1021	6.05×10^{-11}
S/BNTFC/hG	2.60	5.96×10^{-7}	17.21	0.2207	6.61×10^{-10}
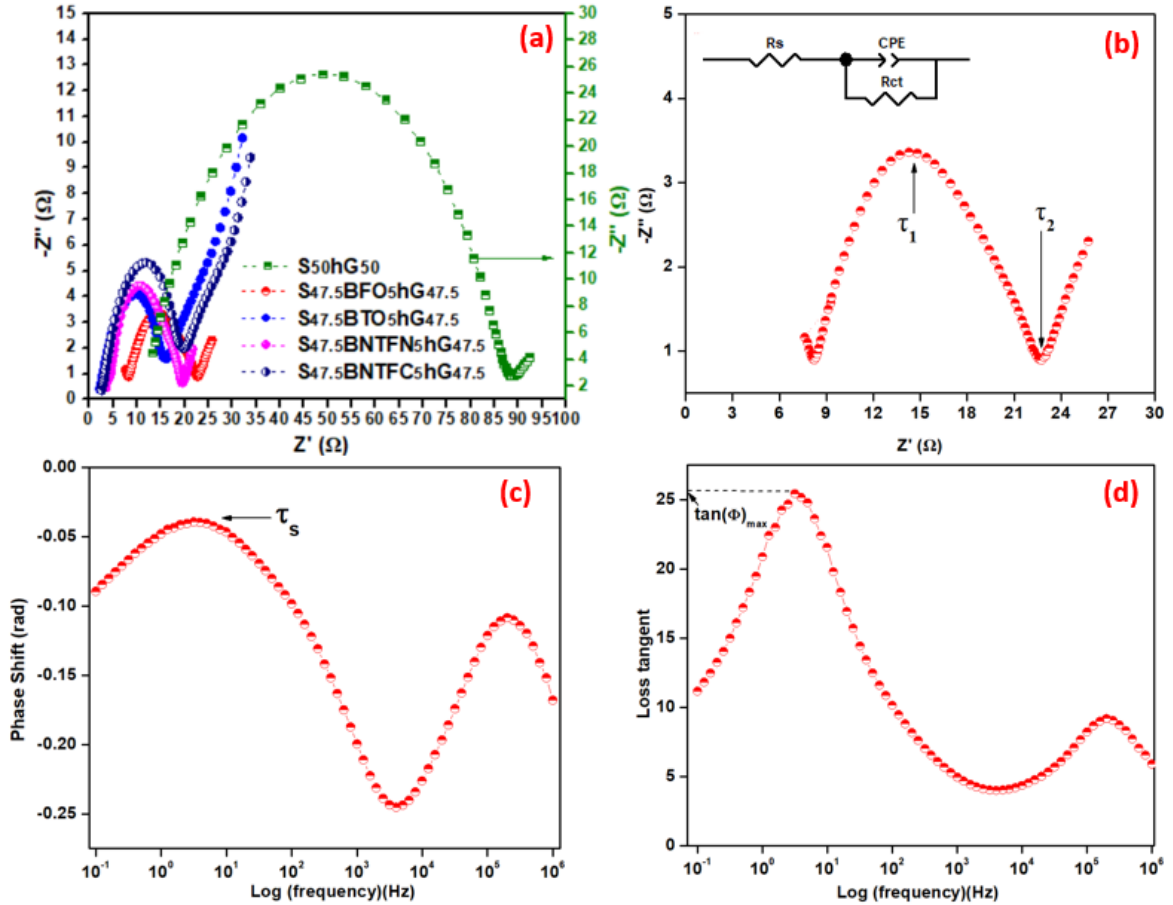
Figure 3.8. Electrochemical impedance spectroscopy spectrum before charge-discharge for all batteries of (a) Nyquist plots of the five batteries of studies from 1 MHz to 0.1 Hz at room temperature, circuit equivalent for batteries (inset) of $S_{47.5}(BFO)_5hG_{47.5}$, and (b, c, and d) Bode plot EIs analysis for batteries with a dry-pressed $S_{47.5}(BFO)_5hG_{47.5}$ cathode.

3.3.6 Electrochemical properties

The electrochemical performance is shown in Figure 3.9 as well as the cyclic behavior of assembled cells with various composite cathodes. To determine the electrochemical performance of the assembled cells, galvanostatic discharge-charge performances were measured at different current densities: 0.5, 0.3, and 0.2 mA/cm^2 (corresponding to C-rates of C/10, 3C/50, and C/25). In Figure 3.9(a–e), the initial discharge capacities of S/hG and

the various S/FNPs/hG composites values at first cycle at 0.2 mA/cm^2 are shown. These are 1390, 1316, 1409, 1062, and 1330 mAh/g$_s$, for S/hG, S/BFO/hG, S/BTO/hG, S/BNTFN/hG, and S/BNTFC/hG respectively. The highest discharge capacity (1409 mAh/g$_s$) occurs with long-term cycling performance up to 58 cycles for S/BTO/hG cathode as shown in discharge-charge profiles. The capacity of cells coupled with ferroelectric nanoparticles remarkably improved compared with the S/hG cells. This result is consistent with the hypothesis that there is an extra internal field induced by ferroelectric nanoparticles that could help to reduce the polysulfides formation during the cycling process and improve the efficiency of ion transport, since the induced macroscopic charges on the surface of ferroelectrics act as "trapping" center for the polysulfides that are heteropolar in nature. The strong polarization of ferroelectric particles also influences distribution of Li ions, yielding diffusion pathways in the electrolyte/active material, which accelerates the transfer speed of Li ions, thus eliminates the concentration gradient of Li-ions near the deposition surface. As the C-rate varies, capacity retention and the discharge profiles of Li-S cells became differentiated. For 0.2 mA/cm^2 and 0.3 mA/cm^2 cycling, the discharge-charge capacity displayed the highest retention during the cycling test up to 90% of S/BNTFN/hG cathode for the 18$^{\text{th}}$ cycles.
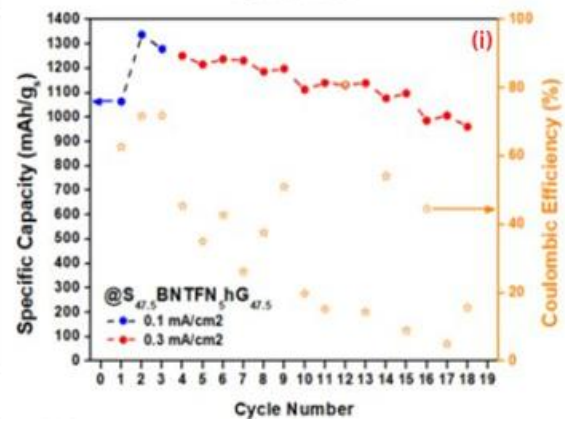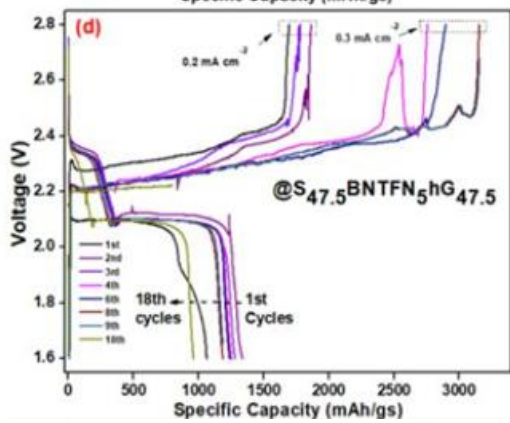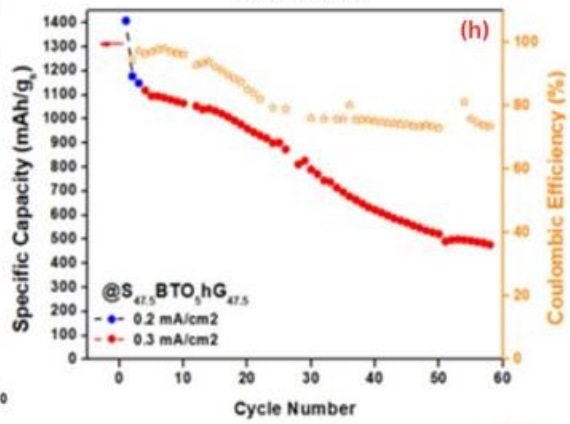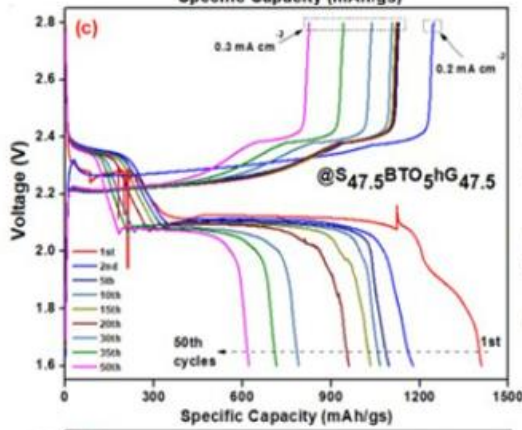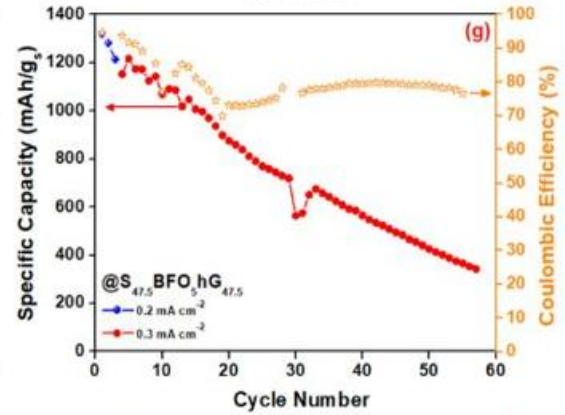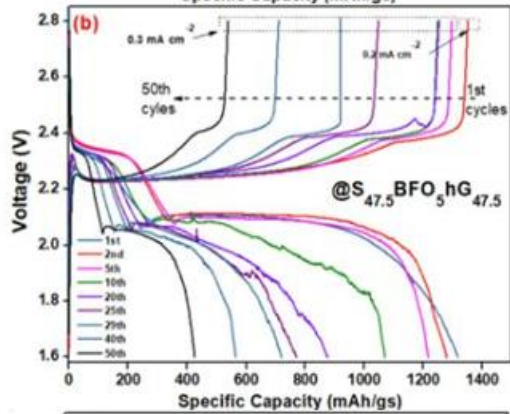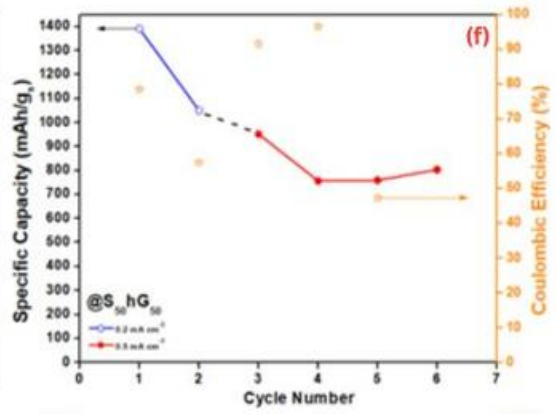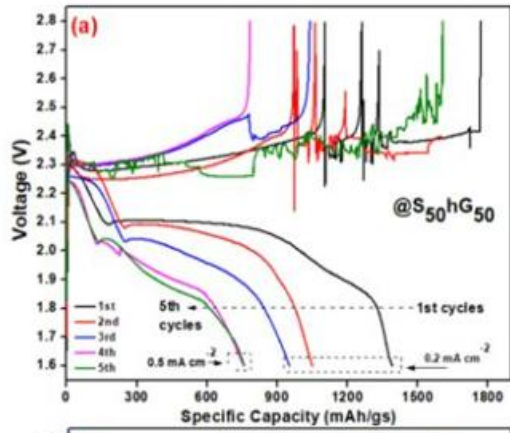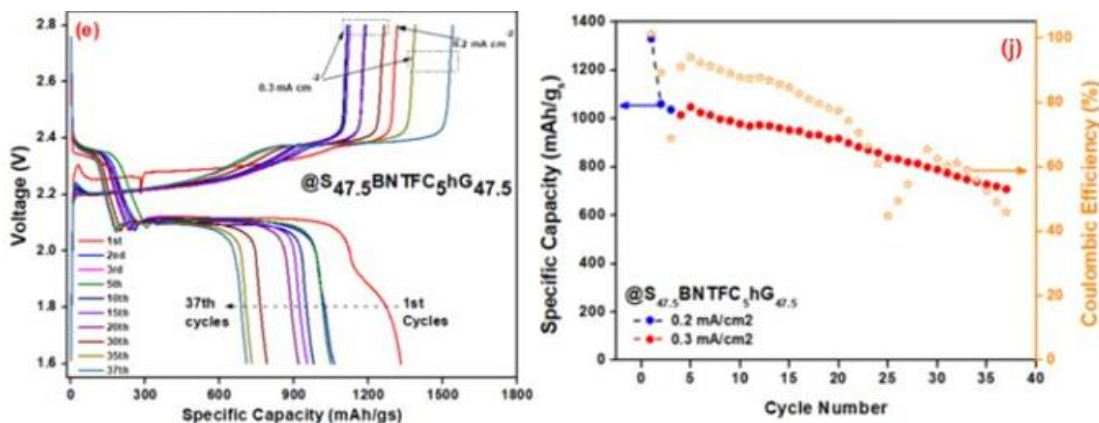
Figure 3.9. Discharge-Charge profiles and specific capacity, Coulombic efficiency in function of battery with $S_{50}hG_{50}$ at various current density from 0.2 mA/cm^2 to 0.5 mA/cm^2 (a-f), battery with $S_{47.5}(BFO)_5hG_{47.5}$ values (b-g), battery with $S_{47.5}(BTO)_5hG_{47.5}$ values (c-h), battery with $S_{47.5}(BNTFN)_5hG_{47.5}$ values (d-i), and battery with $S_{47.5}(BNTFC)_5hG_{47.5}$ values (e-j). All batteries were run over cycling at 0.3 mA/cm^2 (first 3rd cycles were run at 0.2 mA/cm^2).

The capacity fading was closely related to the lowered ability of Li-S insertion-extraction within the electrodes. The presence of FNPs diffuse the active material layers and generate an internal field trapping the polysulfide, which may probably be the main cause of capacity fading observed in the 0.2 mA/cm^2 cycling cell. As shown in Figure 3.9c. and Figure 3.9h, $S_{47.5}(BTO)_5hG_{47.5}$ electrode with the same 7.01 mg$_s$/cm^2 mass loading, mentioned above, also exhibited impressive high capacity in 1st cycle of 1409 mAh/g$_s$, 5th cycle of 1095 mAh/g$_s$, 20th cycle of 959 mAh/g$_s$, and 58th cycle of 477 mAh/g$_s$ (or 9.9, 7.6, 6.7, and 3.3 mA/cm^2 respectively) at current densities of 0.2 mA/cm^2 and 0.3 mA/cm^2, with an overpotential of 0.20 V. The results for $S_{47.5}(BFO)_5hG_{47.5}$ electrode with 6.87 mg$_s$/cm^2 mass loading capacity values were 1316, 1216, 875, and 342 mAh/g$_s$, areal capacity values 9.0, 8.3, 6.0, and 3.3 mA/cm^2 with a low overpotential of 0.16V at

0.2 mA/cm^2 as shown in Figure 3.9b. and Figure 3.9g. The specific capacity values of S/BNTFN/hG for the 1st, 2nd, 5th, 10th, and 18th cycles were 1062, 1337, 1215, 1113, and 960 mAh/g$_s$ respectively, while the current density was 0.2 mA/cm^2 for the first three cycles and 0.3 mA/cm^2 for the rest of the cycles as shown in Figure 3.9d. and Figure 3.9i. The specific capacity values of S/BNTFC/hG cathode for the 1st, 2nd, 5th, 10th, 20th, and 37th cycles were 1330, 1061, 1048, 978, 917, and 708 mAh/g$_s$ respectively, while the current density was 0.2 mA/cm^2 for the first three cycles and 0.3 mA/cm^2 for the rest of the cycles as shown in Figure 3.9e. and Figure 3.9j. Incorporating FNPs in Li-S battery cathodes helps to decrease the rapid formation of polysulfides as the cyclability of the batteries increases. The highest specific capacity was for the cathode containing BFO with a value of 1409 mAh/gs. The second highest was the electrode containing BNTFC nanoparticles with a value of 1330 mAh/gs. A capacity retention value of 90% was obtained for the S/BNTFN/hG battery up to cycle 18. The average Coulombic efficiency for S/hG batteries not containing FNPs was 78.57% while the average Coulombic efficiency for the batteries incorporating FNPs ranged from 62.70% to 94.71%. It is important to highlight that the FNPs increase the cyclability in the batteries (i.e., 18 cycles S/BNTFN, 37 cycles S/BNTFC/hG, 57 cycles S/BFO/hG, and 58 cycles S/BTO/hG). The batteries which did not contain FNPs present low cyclability values, not being able to surpass 6 cycles mark.

The discharge-charge profiles of the five batteries are shown in Figure 3.10. A principal characteristic of the Li-S batteries is that the discharge curve shows two plateau regions. The formation of a valley at the end of the first discharge plateau and a peak at the beginning of the charging process can be seen in the curves as shown in Figure 3.10. The presence of the valley is due to the formation of soluble long-chain polysulfide by the

reduction of elemental sulfur, which was produced during discharge, increasing the viscosity, and decreasing the ion conductivity. However, when the medium chain polysulfides are reduced to the insoluble species (Li_2S_2/Li_2S) in the second plateau, the viscosity of the electrolyte is reduced and reduction of the soluble polysulfides is followed by formation of solid reduction. The peak at the beginning of the charge curve is attributed to the formation of soluble lithium polysulfides from the insulating layers of insoluble species [6, 8, 35-37].
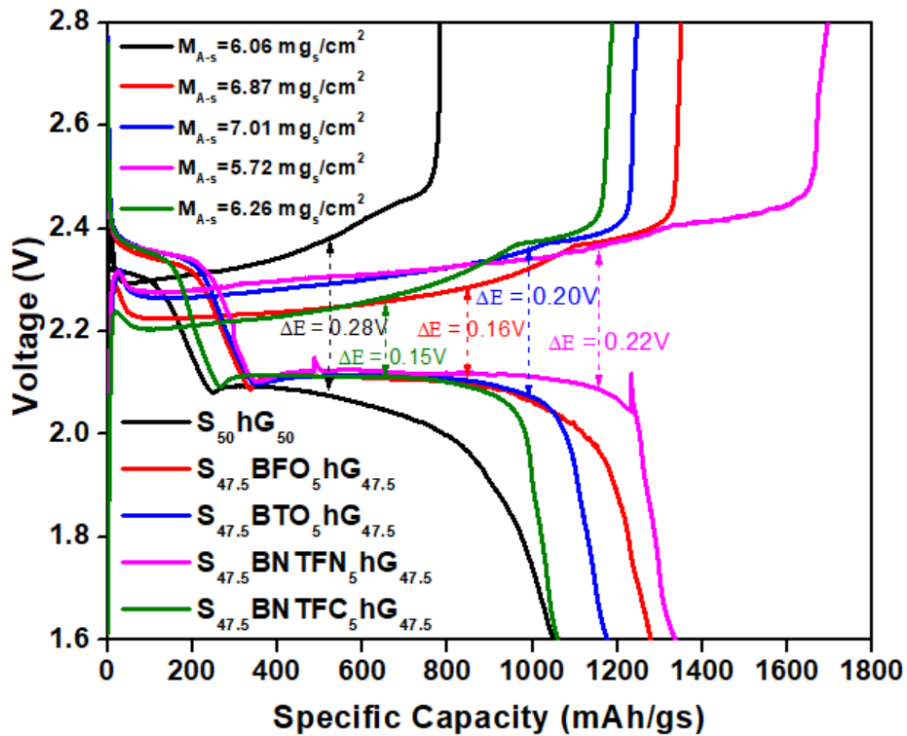
Figure 3.10. Comparison of the discharge-charge profiles of cycle two for S/hG, S/BFO/hG, S/BTO/hG, S/BNTFN/hG, and S/BNTFC/hG for batteries evaluated at current densities of 0.2 mA/cm².

The use of ferroelectric nanoparticles and hG significantly improved the performances of high mass loading cathodes as shown in Figure 3.11. In comparison to S/hG, S/FNPs/hG cathodes exhibited improved S utilization in terms of specific capacity (1316 mAh/g$_s$

versus 1049 mAh/g_s for first cycle) and areal capacity (6.09 mAh/cm^2 versus 9.89 mAh/cm^2 for first cycle). In addition, the S/FNPs/hG electrodes exhibited reduced overpotential (ΔE ~0.15 V versus 0.28 V at the 2nd cycle) in comparison to the S/hG cathode. To achieve high areal capacity, high mass loading of sulfur ranging from 5.72 mg/cm^2 to 7.01 mg/cm^2 has been procured and the obtained value of high areal capacity is of the order of ~10 mAh/cm^2 as shown in Figure 3.11. FNPs are useful in avoiding the loss of soluble polysulfides in the electrolytes as well as reducing the polysulfide formation due to their higher internal field of polarization. Although the theoretical specific capacity of sulfur is difficult to achieve, our method was able to produce high-capacity values.
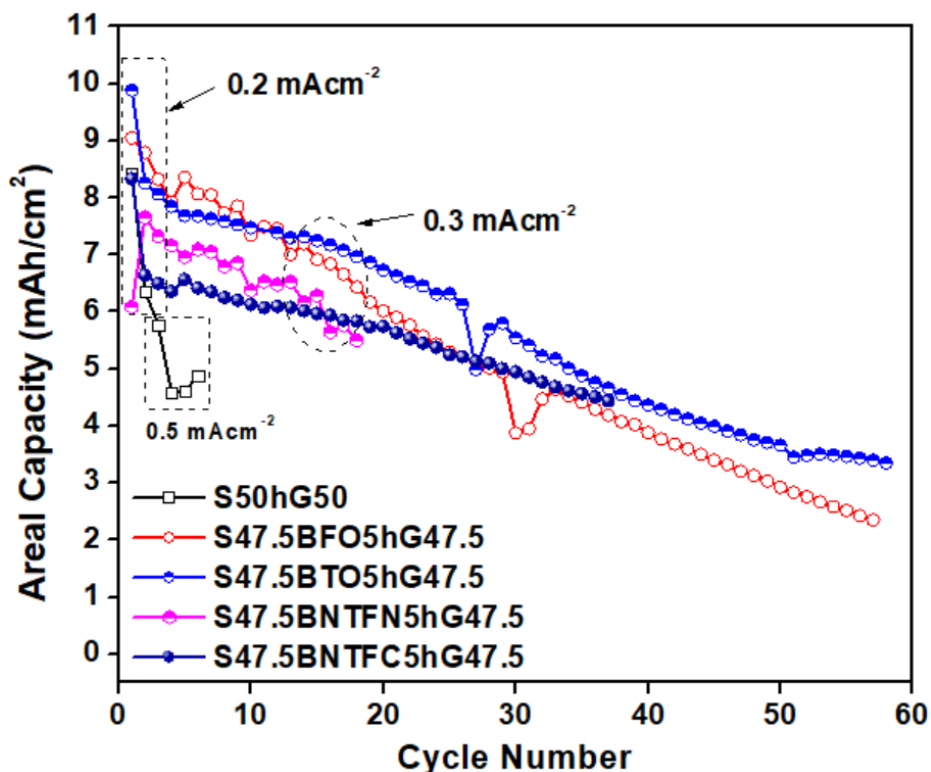
Figure 3.11. Comparison of the areal capacity for the batteries evaluated at different currents densities ran at 0.2 mA/cm^2, 0.3 mA/cm^2, and 0.5 mA/cm^2. The representation of the composite

cathodes are black squares for $S_{50}hG_{50}$, red circles for S/BFO/hG, blue circles for S/BTO/hG, magenta circles for S/BNTFN/hG, and royal circles for S/BNTFC/hG.

References

[1] P.G. Bruce, S.A. Freunberger, L.J. Hardwick, J.M. Tarascon, Li-O$_2$ and Li-S batteries with high energy storage., *Nature Materials 11*(1) (**2011**) 19-29.

[2] D. Herbert, J. Ulam, Electric Dry Cells and Storage Batterries., *United States Patent Office* (**1962**).

[3] H. Yamin, A. Gorenshtein, J. Penciner, Y. Sternberg, E. Peled, Lithium Sulfur Battery Oxidation-Reduction Mechanisms of Polysulfides in THF Solutions., *Journal of The Electrochemical Society* (**1988**).

[4] M.Q. Zhao, Q. Zhang, J.Q. Huang, G.L. Tian, J.Q. Nie, H.J. Peng, F. Wei, Unstacked Double-Layer Templated Graphene for High-Rate Lithium-Sulphur Batteries., *Nat Commun 5* (**2014**) 3410.

[5] B. Liu, R. Fang, D. Xie, W. Zhang, H. Huang, Y. Xia, X. Wang, X. Xia, J. Tu, Revisiting Scientific Issues for Industrial Applications of Lithium-Sulfur Batteries., *Energy & Environmental Materials 1*(4) (**2018**) 196-208.

[6] X. Ji, L.F. Nazar, Advances in Li–S Batteries., *Journal of Materials Chemistry 20*(44) (**2010**).

[7] Y.X. Yin, S. Xin, Y.G. Guo, L.J. Wan, Lithium-Sulfur Batteries: Electrochemistry, Materials, and Prospects., *Angew Chem Int Ed Engl 52*(50) (**2013**) 13186-200.

[8] S.H. Chung, C.H. Chang, A. Manthiram, Progress on the Critical Parameters for Lithium–Sulfur Batteries to be Practically Viable., *Advanced Functional Materials 28*(28) (**2018**).

[9] D. Lv, J. Zheng, Q. Li, X. Xie, S. Ferrara, Z. Nie, L.B. Mehdi, N.D. Browning, J.-G. Zhang, G.L. Graff, J. Liu, J. Xiao, High Energy Density Lithium-Sulfur Batteries: Challenges of Thick Sulfur Cathodes., *Advanced Energy Materials 5*(16) (**2015**).

[10] Z. Deng, Z. Zhang, Y. Lai, J. Liu, J. Li, Y. Liu, Electrochemical Impedance Spectroscopy Study of a Lithium/Sulfur Battery: Modeling and Analysis of Capacity Fading, Journal of The Electrochemical Society 160(4) (2013) A553-A558.

[11] Y. Lin, K.J. Jones, L.C. Greenburg, J.W. Kim, L. Hu, J.W. Connell, Facile, Solvent-Free Preparation of High Density, High Mass Loading Sulfur Cathodes Enabled by Dry-Pressable Holey Graphene Scaffolds., Batteries & Supercaps 2(9) (**2019**) 774-783.

[12] X. Han, Z. Yang, B. Zhao, S. Zhu, L. Zhou, J. Dai, J.W. Kim, B. Liu, J.W. Connell, T. Li, B. Yang, Y. Lin, L. Hu, Compressible, Dense, Three-Dimensional Holey Graphene Monolithic Architecture, ACS Nano 11(3) (2017) 3189-3197.

[13] C.O.P.-R. Yi Lin, Liangbing Hu, and John W. Connell, Scalable Dry-Pressed Electrodes Based on Holey Graphene, American chemican Chemical society 55(20) (2022) 3020-3031.

[14] C.O. Plaza-Rivera, B.A. Walker, N.X. Tran, R.P. Viggiano, D.A. Dornbusch, J.J. Wu, J.W. Connell, Y. Lin, Dry Pressing Neat Active Materials into Ultrahigh Mass Loading Sandwich Cathodes Enabled by Holey Graphene Scaffold, ACS Applied Energy Materials 3(7) (2020) 6374-6382.

[15] C.O. Plaza-Rivera, R.P. Viggiano, D.A. Dornbusch, J.J. Wu, J.W. Connell, Y. Lin, Holey Graphene–Enabled Solvent-Free Preparation of Ultrahigh Mass Loading Selenium

Cathodes for High Areal Capacity Lithium–Selenium Batteries, Frontiers in Energy Research 9 (2021).

[16] D.J. Kirsch, S.D. Lacey, Y. Kuang, G. Pastel, H. Xie, J.W. Connell, Y. Lin, L. Hu, Scalable Dry Processing of Binder-Free Lithium-Ion Battery Electrodes Enabled by Holey Graphene, ACS Applied Energy Materials 2(5) (2019) 2990-2997.

[17] K. Xie, Y. You, K. Yuan, W. Lu, K. Zhang, F. Xu, M. Ye, S. Ke, C. Shen, X. Zeng, X. Fan, B. Wei, Ferroelectric-Enhanced Polysulfide Trapping for Lithium-Sulfur Battery Improvement, Adv Mater 29(6) (2016).

[18] T. Yim, S.H. Han, N.H. Park, M.-S. Park, J.H. Lee, J. Shin, J.W. Choi, Y. Jung, Y.N. Jo, J.-S. Yu, K.J. Kim, Effective Polysulfide Rejection by Dipole-Aligned $BaTiO_3$ Coated Separator in Lithium-Sulfur Batteries, Advanced Functional Materials 26(43) (2016) 7817-7823.

[19] D. Ma, Y. Li, J. Yang, H. Mi, S. Luo, L. Deng, C. Yan, M. Rauf, P. Zhang, X. Sun, X. Ren, J. Li, H. Zhang, New Strategy for Polysulfide Protection Based on Atomic Layer Deposition of TiO_2 onto Ferroelectric-Encapsulated Cathode: Toward Ultrastable Free-Standing Room Temperature Sodium-Sulfur Batteries., Advanced Functional Materials 28(11) (2018).

[20] B.D. Son, S.H. Cho, K.Y. Bae, B.H. Kim, W.Y. Yoon, Dual functional effect of the ferroelectricity embedded interlayer in lithium sulfur battery, Journal of Power Sources 419 (2019) 35-41.

[21] H.-J. Peng, J.-Q. Huang, X.-B. Cheng, Q. Zhang, Review on High-Loading and High-Energy Lithium-Sulfur Batteries, Advanced Energy Materials 7(24) (2017).

[22] Z. Zhao, G. Li, Z. Wang, M. Feng, M. Sun, X. Xue, R. Liu, H. Jia, Z. Wang, W. Zhang, H. Li, Z. Chen, Black $BaTiO_3$ as Multifunctional Sulfur Immobilizer for Superior Lithium Sulfur Batteries, Journal of Power Sources 434 (2019).

[23] M.K. Singh, W. Prellier, M.P. Singh, R.S. Katiyar, J.F. Scott, Spin-Glass Transition in Single-Crystal $BiFeO_3$, Physical Review B 77(14) (2008).

[24] S.R. Das, R.N.P. Choudhary, P. Bhattacharya, R.S. Katiyar, P. Dutta, A. Manivannan, M.S. Seehra, Structural and Multiferroic Properties of La-Modified $BiFeO_3$ Ceramics, Journal of Applied Physics 101(3) (2007).

[25] B. Tripathi, R.K. Katiyar, G. Morell, A. Dixit, R.S. Katiyar, $BiFeO_3$ Coupled Polysulfide Trapping in C/S Composite Cathode Material for Li-S Batteries as Large Efficiency and High Rate Performance, Energies 14(24) (2021).

[26] Y. Lin, X. Han, C.J. Campbell, J.-W. Kim, B. Zhao, W. Luo, J. Dai, L. Hu, J.W. Connell, Holey Graphene Nanomanufacturing: Structure, Composition, and Electrochemical Properties, Advanced Functional Materials 25(19) (2015) 2920-2927.

[27] K.D. P.Rajkumar, R.Subadevi, M.Sivakumar, Preparation and Physical Characterization of sulfur/Carbon Black Compisite Cathode Material for Li-s battery., International Research Journal of Engineering and Technology (IRJET) (2017) 3.

[28] M. Čebela, D. Zagorac, K. Batalović, J. Radaković, B. Stojadinović, V. Spasojević, R. Hercigonja, $BiFeO_3$ Perovskites: A Multidisciplinary Approach to Multiferroics, Ceramics International 43(1) (2017) 1256-1264.

[29] F. Sun, Y.S. Yin, Rietveld Refinement of the $BaTiO_3$ from X-ray Powder Diffraction, Advanced Materials Research 79-82 (2009) 593-596.

[30] X. Chen, J. Xiao, J. Yao, Z. Kang, F. Yang, X. Zeng, Room Temperature Magnetoelectric Coupling Study in Multiferroic $Bi_4NdTi_3Fe_{0.7}Ni_{0.3}O_{15}$ Prepared by a Multicalcination Procedure., Ceramics International 40(5) (2014) 6815-6819.

[31] F.J. Yang, P. Su, C. Wei, X.Q. Chen, C.P. Yang, W.Q. Cao, Large Magnetic Response in $(Bi_4Nd)Ti_3(Fe_{0.5}Co_{0.5})O_{15}$ Ceramic at Room-Temperature, Journal of Applied Physics 110(12) (2011).

[32] Y.P.a.B.D. VD Mote, Williamson-Hall Analysis in Estimation of Lattice Strain in Nanometer-Sized ZnO Particles, Journal of Theoretical and Applied Physics (2012).

[33] T.Q. Nguyen, C. Breitkopf, Determination of Diffusion Coefficients Using Impedance Spectroscopy Data, Journal of The Electrochemical Society 165(14) (2018) E826-E831.

[34] T. Wang, Q. Zhang, J. Zhong, M. Chen, H. Deng, J. Cao, L. Wang, L. Peng, J. Zhu, B. Lu, 3D Holey Graphene/Polyacrylonitrile Sulfur Composite Architecture for High Loading Lithium Sulfur Batteries, Advanced Energy Materials 11(16) (2021).

[35] A. Manthiram, S.H. Chung, C. Zu, Lithium-Sulfur Batteries: Progress and Prospects, Adv Mater 27(12) (2015) 1980-2006.

[36] J. Sun, Y. Sun, M. Pasta, G. Zhou, Y. Li, W. Liu, F. Xiong, Y. Cui, Entrapment of Polysulfides by a Black-Phosphorus-Modified Separator for Lithium-Sulfur Batteries, Adv Mater 28(44) (2016) 9797-9803.

[37] J. Yan, X. Liu, B. Li, Capacity Fade Analysis of Sulfur Cathodes in Lithium-Sulfur Batteries, Adv Sci (Weinh) 3(12) (2016) 1600101.

Chapter 4

High Areal Capacity and Sustainable High Energy in Ferroelectric Doped Holey Graphene/Sulfur Composite Cathode for Lithium-Sulfur Batteries

4.1 Introduction

Li-S rechargeable batteries with high-energy capacity are considered one of the most promising energy storage systems for electronic devices and electric vehicles, such as electronic devices and electric vehicles [1]. These Li-S batteries have the following advantages: low cost, low operating voltage (2.2V), environment friendly, high energy storage system due to its higher theoretical energy density (2600 Wh/kg) and theoretical specific capacity (1675 mAh/g) [2-6]. On the other hand, they present a disadvantage since low sulfur cycle life reduces the performance of Li-S batteries [7]. These challenges can be dealt with by adding a carrier material with a rich pore structure to adsorb lithium polysulfides and chemisorption [8, 9], limiting the dissolution and diffusion of lithium polysulfide between polar carrier materials and lithium polysulfides (LiPs) [10]. The insulating nature of sulfur still limits the development of high-loading sulfur cathodes with sufficient sulfur content, and most existing cathodes have low sulfur loadings (<2 mg/cm^2) and low sulfur contents (<60 wt%) [11]. To address these problems, porous substrates with various functions have emerged as an effective sulfur host that can prevent the rapid loss of large amounts of polysulfides, especially at increased sulfur loadings. To improve the sulfur conductivity and sulfur loading area, porous carbon materials are applied. The pore structure enhances sulfur loading as well as promoting fast ion diffusion. Furthermore, the

capillary effect of the elemental sulfur filled in pores can effectively inhibit the diffusion of LiPs into the electrolyte, slow down the shuttle effect, and increase the utilization rate of active materials to improve the energy density of Li-S batteries. Various synthesis strategies of S-doped carbon as electrode materials for energy storage applications have been reported [12], including thermal treatment [13], hydrothermal method [14], biomass-assisted synthesis [15], polymer-assisted synthesis [16], template-assisted synthesis [17], microwave-assisted synthesis [18], solvothermal method [19], sol-gel processing [20], chemical vapor deposition [21], and sublimation [22]. Song and co-workers [23] synthesized highly crumpled nitrogen-doped graphene (NG) with an ultrahigh pore volume and large surface area, enabling strong LiPs adsorption, and high sulfur content and areal loading in the NG host and reported high capacity of ≈1000 mAh/g with 80 wt.% sulfur content and high sulfur loading of 5 mg /cm^2. Ferroelectric nanoparticles (FNPs) exhibiting spontaneous polarization, provides strong interaction with electric field [24] having capability to suppress shuttle effects in sulfur cathode. FNPs into cathode eliminates the concentration gradient of Li-ions near the deposition surface, yielding diffusion pathways in electrolyte/active material, and accelerating the transfer speed of Li-ions. In commercial batteries, the areal capacity density of cathode is generally higher than 2.0 mAh/cm^2 with an average output voltage of 3.5 V. However, the areal capacity density of sulfur cathode is higher than 3.3 mAh/cm^2 considering the average voltage of 2.1 V for Li-S batteries [25]. Moreover, for electric vehicle (EV) applications to deliver a mileage of more than 300 miles, an areal capacity of 5 mAh/cm^2 and energy density of 500 Wh/kg are required to support its practical power output requirements, due to which high sulfur loading and high sulfur utilization are needed to achieve high areal capacity and high energy density of Li-

S batteries[26, 27]. We recently demonstrated that the hG framework greatly improves the performance of electrodes, facilitating the active material to fully participate in electrochemical reactions [28]. Ferroelectrics have strong polarization and can assist polysulfides chemisorption as well as altering Li^+ diffusion. The uniform distribution of ferroelectrics is expected to contribute to enhance affinity to polysulfides in the overall cell system [29, 30]. Moreover, it can be seen that the C/S +BTO composite exhibits a higher initial discharge capacity of 1143 mAh/g at 0.2 C after 100 cycles, and for the C/S electrode without BTO nanoparticles discharge capacity of 407 mAh/g can be obtained after 100 cycles [31]. In 2019, a unique "black" B-BTO was developed for the first time as a multifunctional sulfur immobilizer to improve performance, promote high conductivity with electron transfer and facilitate kinetics with sulfur reaction in this type of battery [32]. The bismuth ferrite $BiFeO_3$ (BFO) incorporated in cathode reduced the impact of polysulfide shuttle and improved the cyclic stability. The cathode capacity of the $S_{60}BFO_{30}C_{10}$ composite Li-S battery reached ~1600 mAh/g, and the cell operated up to 30 cycles [33]. In most of the work on Li-S batteries, the ferroelectric nanoparticle materials are incorporated in the separator or cathode of these devices. In Table 4.1, we make a comparison of these references and our work in terms of capacity retention, cyclability, initial specific capacity and Coulombic efficiency [29, 31-35]. It can be seen that we achieved a much better overall performance in relation to these references. In this study, we are presenting the effect of mass loading and coupling of different FNPs such as BTO, BFO, BNTFN, and BNTFC on hG/S composites to achieve high areal capacity in Li-S cathodes.

Table 4.1. Comparison of reported results on incorporated ferroelectric materials in Li-S batteries, initial specific capacity, Cyclability, capacity retention, and Coulombic efficiency of separator and cathode compositions.

Reference	Incorporated Ferroelectric Materials	Initial Specifics Capacity [mAh/g]	Cyclability	Capacity Retention	Coulombic Efficiency
2016[29] Separator	A. PE B. PE-poled BTO C. PE–BTO	997.2 1121.1 1124	50 cycles 50 cycles 50 cycles	59.4% 82.8% 72.3%	26.3% 79.6% 42.3%
2016[31] Cathodes	A. C/S B. C/S +BTO C. Multi-rate (A and B)	407 1143-0.2C A. B.	100 cycles 100 cycles 60 cycles	------------ ---------- -----------	------------- ------------ ------------
2019[32] Cathodes	A. C/S B. C/S @B-BTO C. C/S@W-BTO D. Multi-rate (A, B, and C)	1009.1 1129.5 928.2 A. 223.9, B. 607.6 C. 475.2	200 cycles 200 cycles 200 cycles 50 cycles 50 cycles 50 cycles	71.3% 80.2% 42.5% --------- --------- ---------	------------ ------------- ------------- ----------- ------------- --------------
2021[34]	A. Celgard 2320 B. AC/GO C. AC/BTO D. AC/BTO-g-GO C. Multi-rate (B, C, and D)	910 1200 950 1450-0.1C -----------	--------- --------- --------- 100 cycles 55 cycles	--------- --------- --------- -------- --------	--------- --------- --------- --------- 75%
2021[33] Cathodes	A. S60BFO30C10 B. S70BFO20C10 C. S80BFO10C10	1600 1525 1450	30 cycles 30 cycles 30 cycles	~86% ------ ~62%	86% -------- --------
2023[35] Cathodes	A. S/hG B. S/BFO/hG C. S/BTO/hG D. S/BNTFN/hG E. S/BNTFC/hG	1390 1316 1409 1069 1330	6 cycles 57 cycles 58 cycles 18 cycles 37 cycles	57.7% 26% 34% 90% 53%	25% 83.71% 82.65% 78.93% 86.92%
2023 This work Cathodes	A. S/CBhG/PVDF B. S/BTO/CBhG/PVDF C. S/BFO/CBhG/PVDF D. S/BNTFN/CBhG/PVDF E. S/BNTFC/CBhG/PVDF	1123 1402 1430 1486 1509	134 cycles 110 cycles 116 cycles 158 cycles 107 cycles	54.49% 46.72% 45.31% 43.40% 37.90%	83% 87% 78% 93% 90%

4.2 Experimental details

Materials. In this work, the hG was prepared from graphene (Vorbeck materials) using the established one-step air oxidation procedure previously reported [36]. Bis(trifluoromethylsulfonyl)imide lithium salt (LiTFSI; 98+%), lithium nitrate (LiNO₃;

99.99%), 1,2-dimethoxyethane (DME; 99+%), and 1,3-dioxolane (DOL; 99.5%) were purchased from Thermo Fisher*[2]. Sulfur (S; 99.998%), highly pure barium carbonate ($BaCO_3$; 99.8%), Neo-dymium (III) oxide (Nd_2O_3; 99.9%), lithium foil 0.75 mm thick x 19 mm wide (Al; 99.9%), high-purity cobalt (II, III) oxide (Co_3O_4; 99.998%), polyvinylidene fluoride (PVDF), and carbon back (CB) were purchased from Alfa Aesar*[1]. Iron oxide (Fe_2O_3; 99.998%), nickel (III) oxide nanopowder (Ni_2O_3; 99%), and Celgard membrane 25 µm thickness and 85 mm width were purchased from Sigma-Aldrich*[1]. High-purity bismuth oxide (Bi_2O_3; 99.9%) was purchased from Fluka, and titanium dioxide (TiO_2; 97%) was purchased from Fisher Scientific*[1]. All precursors and elements for the battery assembly were managed inside the glove box filled with argon, water (H_2O) and oxygen (O_2) contents <0.5 ppm.

Synthesis of ferroelectric nanoparticles. The FNPs were synthesized via mechanical activation followed by thermal treatment. Stoichiometric amounts of 15 wt% excess of Bi_2O_3 were used to compensate volatilization loss during the thermal treatment. The oxides were mixed with isopropanol using a high-energy ball-milling planetary machine with zirconia balls (Across International, PQ-N04 planetary ball mill, USA) operating at 45 Hz (2700 rpm) for 8 hrs. The synthesized material was dried on a hot plate at 100 °C for 8 hrs. We used a furnace (Carbolite, HTF1700, USA) at a heating and cooling rate of 5 °C/min in which the powders were calcined.

---

*[1]Specific vendor and manufacturer names does not imply an endorsement by the authors, nor does it imply that the specified material or equipment is the best available.

Sulfur-FNPs-holey graphene/Carbon black-PVDF composite cathode preparation and characterizations. In a typical experiment to prepare $S_{25}(CBhG)_{65}PVDF_{10}$ and $S_{25}FNPs_5(CB_{98.5\%}hG_{1.5\%})_{60}PVDF_{10}$ composite cathode, individual powder was mixed in a particular ratio by using ball milling to fabricate composite electrodes of $S_{25}(CB_{98.5\%}hG_{1.5\%})_{65}PVDF_{10}$ and $S_{25}FNPs_5(CB_{98.5\%}hG_{1.5\%})_{60}PVDF_{10}$. For each sample, 100 mg composite was prepared in the desirable amount of S, CBhG, FNPs PVDF powders (weight ratios of 2.5:0.0:6.5:1.0 and 2.5:0.5:6.0:1.0 for a total of five different samples) and loaded in a 50 ml zirconia vial. After placing two zirconia balls in the vial, the set was secured in PQ-N04 series planetary ball mills and milled for 10−15 seconds to yield the $S_{25}(CBhG)_{65}PVDF_{10}$ and $S_{25}FNPs_5(CB_{98.5\%}hG_{1.5\%})_{60}PVDF_{10}$ composites. The PVDF has been used as binder and d CB as conductor to improve the electrical conductivity and cycle life of the active material. PVDF as binder helps counter volumetric changes occurring in the insertion electrodes during intercalation/deintercalation and insure adhesion to the current collectors useful for the stability of the electrodes. The fabrication of composite cathodes using the dry-press method is facile and does not require the use of solvent. The hG can be compressed from its dry powder form into solid architectures of various shapes [37-39]. For the fabrication of the electrode disc, 20 mg of the material was added to the 13 mm diameter stainless-steel pressing die. The pressed powders were directly used as the composite cathode $S_{25}(CBhG)_{65}PVDF_{10}$ and $S_{25}FNPs_5(CBhG)_{60}PVDF_{10}$, while polypropylene membrane as separator and lithium foil were used as anode for assembling the coin cells (CR2032). To prepare the electrolyte, 1M LiTFSI and 0.2M $LiNO_3$ were dissolved in DOL/DME (1:1, v/v). To calculate the proper amount of electrolyte (40 uL) we use 5.72 mg_s of the active mass with cathode loadings as 7 mL/g_s. This technique

facilitates preparation, and it is less time consuming than conventional solvent-based methods. Table 4.2 summarizes the critical cell parameters, such as sulfur content, sulfur loading, and electrolyte to sulfur ratios. Powder X-ray Diffractometer for structure, scanning electron microscopy for surface morphology of the electrodes, Raman spectroscopy were performed for electronic structure. Galvanostatic discharge-charge curves were collected using battery tester. A detailed description of FNPs synthesis intercalation inside the sulfur cathode and their characterization was provided in the article "Holey Graphene/Ferroelectric/Sulfur Composite Cathodes for High-Capacity Lithium-Sulfur Batteries" published in ACS Omega by the authors [35].

Table 4.2. Summarizes the critical cell parameters.

Electrodes	Sulfur content (wt%) [mg$_s$]	Sulfur loading [mgs/cm^2]	Electrolyte to sulfur ratio [μL]
S/CBhG/PVDF	5.72	4.31	40
S/BTO/CBhG/PVDF	4.81	3.62	34
S/BFO/CBhG/PVDF	5.20	3.92	36
S/BNTFN/CBhG/PVDF	4.57	3.45	32
S/BNTFC/CBhG/PVDF	5.92	4.46	42

4.3 Results and discussion
4.3.1 X-ray diffraction

Figure 4.1(a–e) shows X-ray diffraction (XRD) spectra of $S_{25}(CBhG)_{65}PVDF_{10}$ and $S_{25}FNPs_5(CBhG)_{60}PVDF_{10}$ composites. The XRD analysis was performed to investigate structural changes due to the incorporation of materials such as, BTO [37], BFO [40], BNTFN [41], BNTFC [42], and their possible reactions with S, CB, hG, and PVDF. As shown in Figure 4.1, the prominent peak of *hkl* (222) at $2\Theta = 23°$ corresponds to the *Fddd* orthorhombic structure of S (JCPDS No. 08-0247) [43, 44]. The peak planes of (002) and (101) are at $2\Theta = 25°$ and 43° attributed to carbon materials (either CB or hG) respectively,

however, (110) plane at 2Θ = 27° corresponds to PVDF. These peaks are detected in all cathode compounds demonstrating the presence of all the aforementioned materials. Furthermore, the rest of the identified peaks can be perfectly indexed with their respective miller indices in the XRD spectra corresponding to the FNPs.
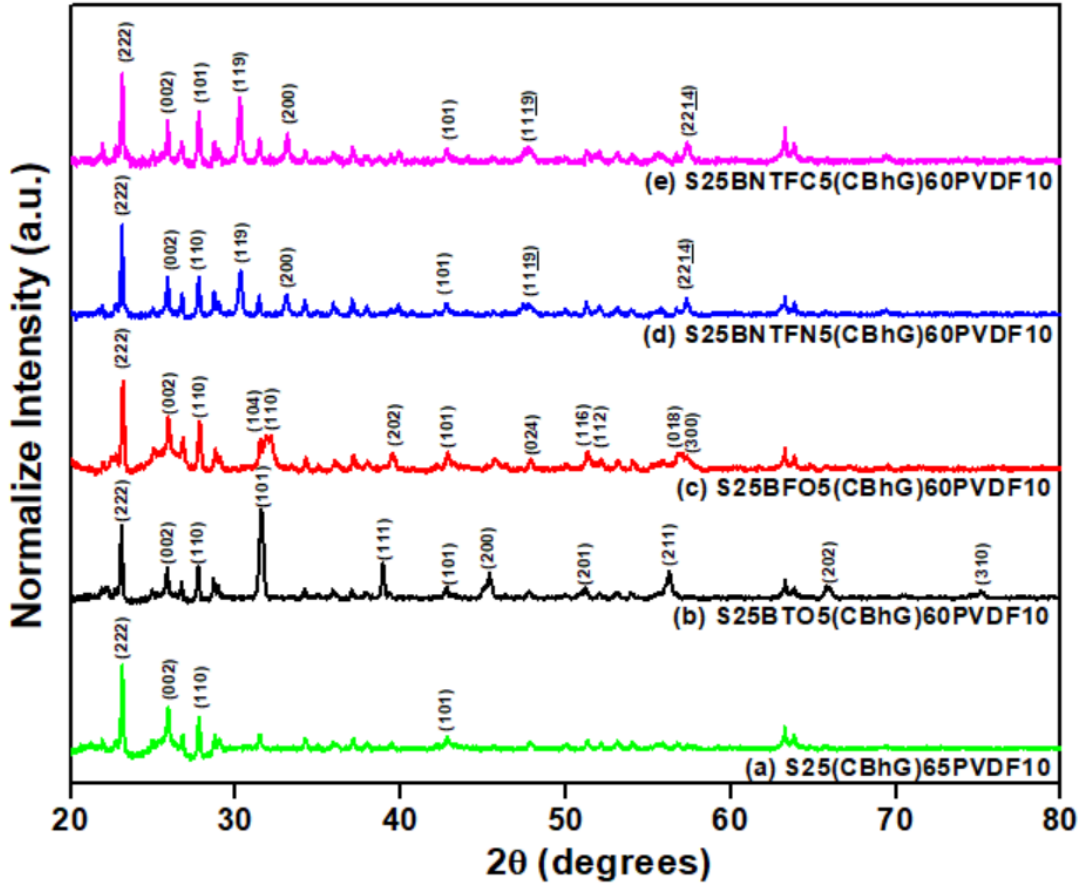
Figure 4.1. XRD spectra of (a) $S_{25}(CBhG)_{65}PVDF_{10}$ composite, (b) $S_{25}BTO_5(CBhG)_{60}PVDF_{10}$, (c) $S_{25}BFO_5(CBhG)_{60}PVDF_{10}$, (d) $S_{25}BNTFN_5(CBhG)_{60}PVDF_{10}$, and (e) $S_{25}BNTFC_5(CBhG)_{60}PVDF_{10}$ composites.

4.3.2 Raman spectroscopy

Figure 4.2(a–e) shows Raman spectra for $S_{25}(CBhG)_{65}PVDF_{10}$ and $S_{25}FNPs_5(CBhG)_{60}PVDF_{10}$ composites. The pronounced D band (disorder-induced phonon

mode) at around 1336 cm^{-1} and a G band (associated with in-plane vibration of the graphite lattice) at around 1575 cm^{-1} suggest a graphite like carbon framework [45, 46]. The intensity ratios (I_D/I_G) shown in Figure 4.2a (I_D/I_G is 1.06 for S/CBhG/PVDF), Figure 4.2b (I_D/I_G is 1.10 for S/BTO/CBhG/PVDF), Figure 4.2c (I_D/I_G is 1.01 for S/BFO/CBhG/PVDF), Figure 4.2e (I_D/I_G is 1.00 for S/BNTFC/CBhG/PVDF), and Figure 4.2d (I_D/I_G is 0.97 for S/BNTFN/CBhG/PVDF) were slightly reduced, presumably due to the defect removal through the combined effects of ferroelectric nanoparticles doping. The Raman peaks for 2D and D+G are also visible around 2700 cm^{-1} attributed to layered structure of graphene.
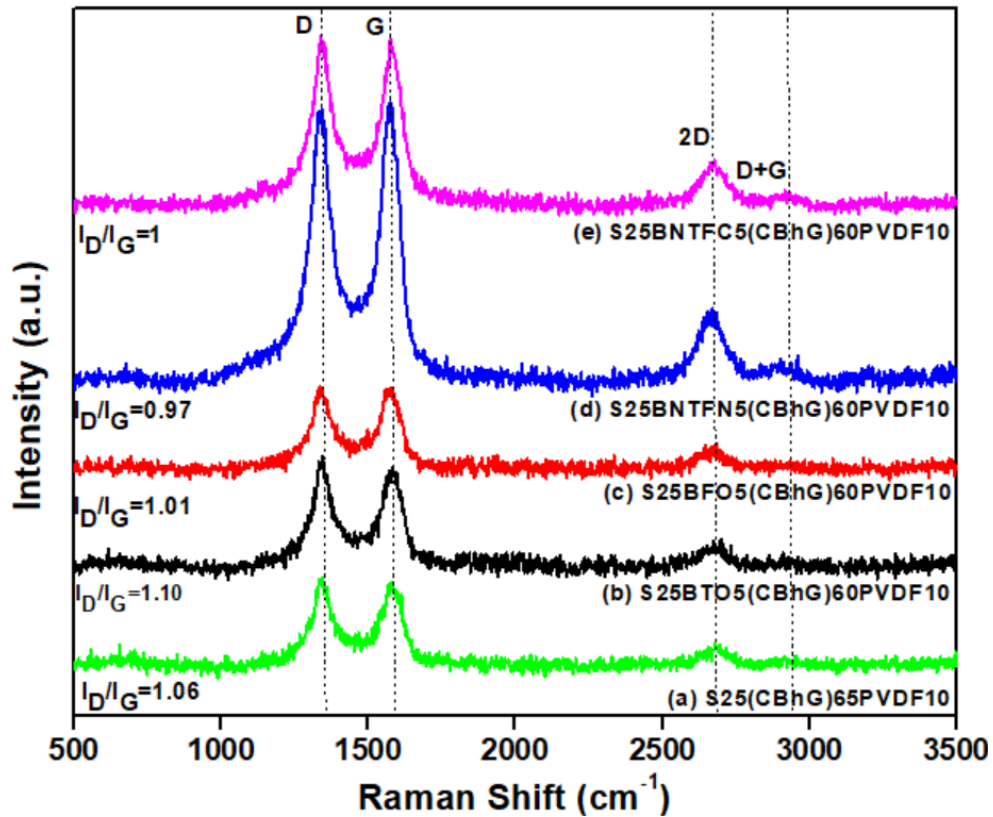
Figure 4.2. Raman spectra of (a) $S_{25}(CBhG)_{65}PVDF_{10}$ composite, (b) $S_{25}BTO_5(CBhG)_{60}PVDF_{10}$, (c) $S_{25}BFO_5(CBhG)_{60}PVDF_{10}$, (d) $S_{25}BNTFN_5(CBhG)_{60}PVDF_{10}$, and (e) $S_{25}BNTFC_5(CBhG)_{60}PVDF_{10}$ composites.

4.3.3 SEM and EDS measurements

Figure 4.3(a–e) shows SEM images of $S_{25}(CBhG)_{65}PVDF_{10}$ and $S_{25}FNPs_5(CBhG)_{60}PVDF_{10}$ composites respectively. It is clear from Figure 4.3(a−e) that BTO, BFO, BNTFN, BNTFC ferroelectric nanoparticles, carbon black, holey graphene, and sulfur were well mixed in the composites. The composite surface is smooth, which confirms that sulfur dispersed in hG framework very well. The holey graphene and CB acts as an efficient electron transport carrier to ensure good electrical contact within the composites. The layered structures provide sufficient space for effectively absorbing electrolyte, and buffering volume expansion of sulfur could help sufficient electrochemical reactions and excellent cycling performance [46].
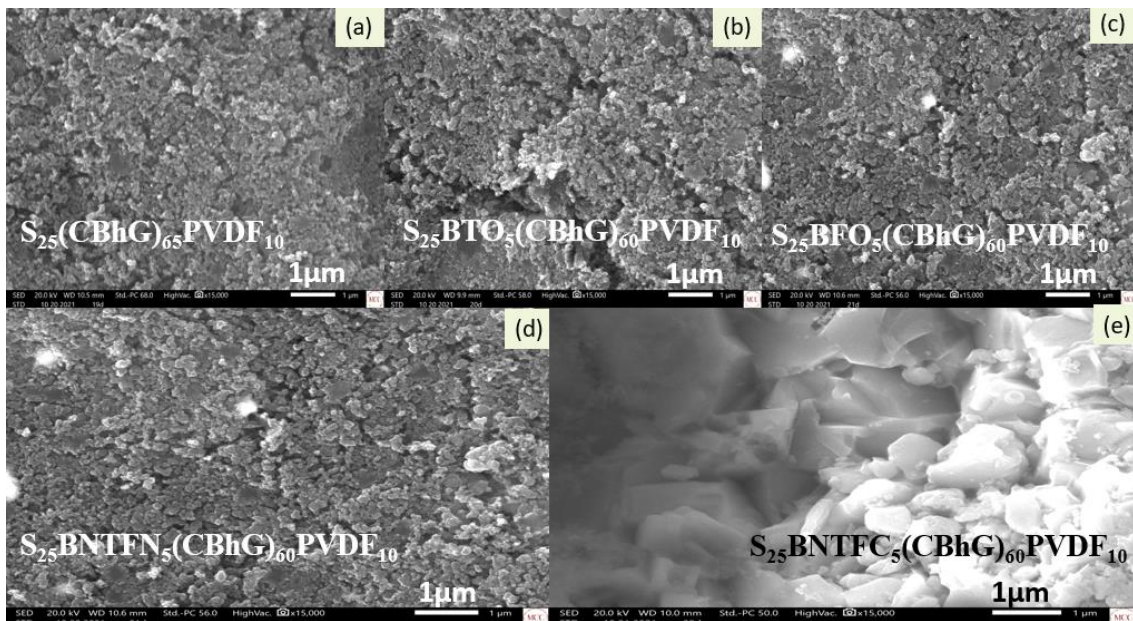
Figure 4.3. SEM images of (a) $S_{25}(CBhG)_{65}PVDF_{10}$ composite, (b) $S_{25}BTO_5(CBhG)_{60}PVDF_{10}$, (c) $S_{25}BFO_5(CBhG)_{60}PVDF_{10}$, (d) $S_{25}BNTFN_5(CBhG)_{60}PVDF_{10}$, and (e) $S_{25}BNTFC_5(CBhG)_{60}PVDF_{10}$ composites with magnification of **X15000** at 1µm.

Figure 4.4. shows EDS spectra of $S_{25}(CBhG)_{65}PVDF_{10}$ and $S_{25}FNPs_5(CBhG)_{60}PVDF_{10}$ composites. In each spectrum, the S-peak is dominant due to its higher concentration relative to the carbon black, hG, PVDF, $BiFeO_3$, $BaTiO_3$, $Bi_4NdTi_3Fe_{0.7}Ni_{0.3}O_{15}$, and $Bi_4NdTi_3Fe_{0.5}Co_{0.5}O_{15}$ since the observed peaks clearly indicate their presence.
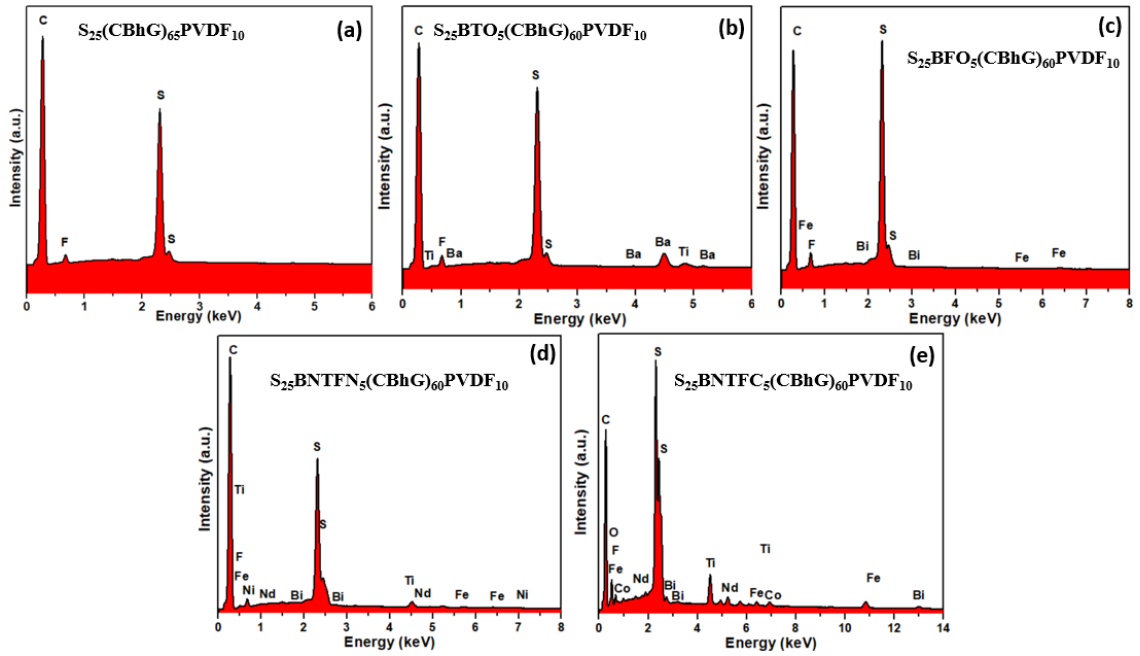
Figure 4.4. EDS of (a) $S_{25}(CBhG)_{65}PVDF_{10}$ composite, (b) $S_{25}BTO_5(CBhG)_{60}PVDF_{10}$, (c) $S_{25}BFO_5(CBhG)_{60}PVDF_{10}$, (d) $S_{25}BNTFN_5(CBhG)_{60}PVDF_{10}$, and (e) $S_{25}BNTFC_5(CBhG)_{60}PVDF_{10}$ composites.

4.3.4 Electrochemical impedance spectra

Figure 4.5 shows Nyquist plots for $S_{25}(CBhG)_{65}PVDF_{10}$, $S_{25}BTO_5(CBhG)_{60}PVDF_{10}$, $S_{25}BNTFN_5(CBhG)_{60}PVDF_{10}$ and $S_{25}BNTFC_5(CBhG)_{60}PVDF_{10}$ composites. The Nyquist plot of $S_{25}BFO_5(CBhG)_{60}PVDF_{10}$ composite is shown in the inset for clarity. All the EIS spectra show depressed semicircles in the high-frequency region, corresponding to the

charge transfer process, and a sloping straight line in the low-frequency region consistent to semi-infinite Warburg diffusion process [45, 46].
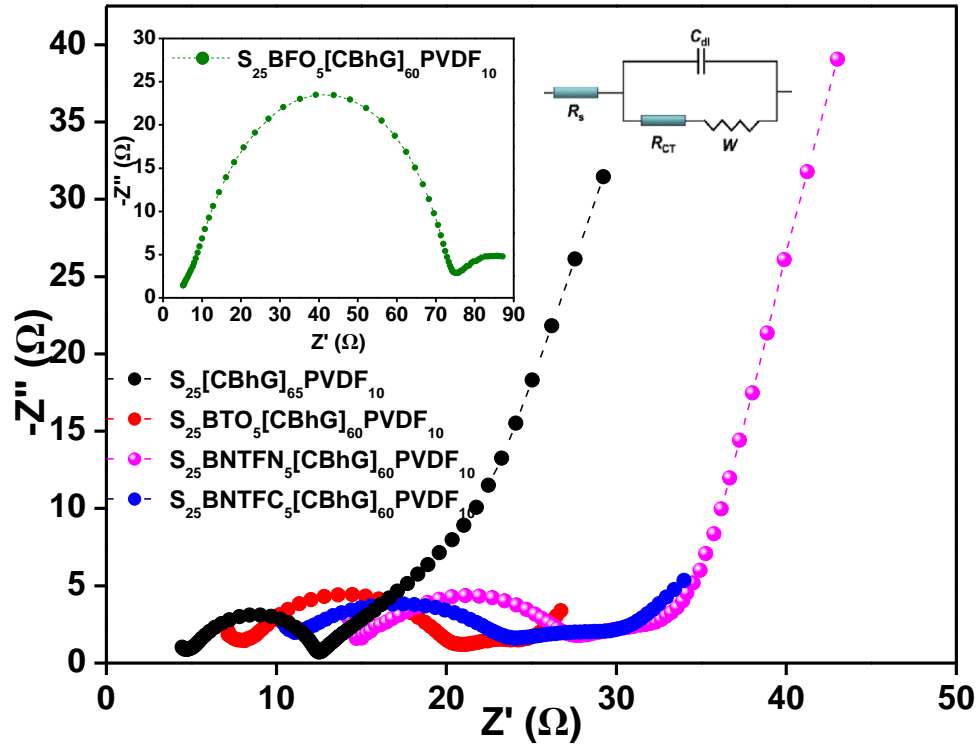
Figure 4.5. Nyquist plot comparison from electrochemical impedance spectroscopy spectrum measurements before charge-discharge of all battery cells with $S_{25}(CBhG)_{65}PVDF_{10}$, $S_{25}BTO_5(CBhG)_{60}PVDF_{10}$, $S_{25}BFO_5(CBhG)_{60}PVDF_{10}$ (inset), $S_{25}BNTFN_5(CBhG)_{60}PVDF10$, and $S_{25}BNTFC_5(CBhG)_{60}PVDF_{10}$ cathode of studies from 1 MHz to 0.1 Hz at room temperature with circuit model.

The EIS spectra before charge-discharge for all batteries were fitted with an R(CR)W model and the results are shown in Table 4.3. It was observed that the charge transfer resistance (R_{ct}) values for $S_{25}FNPs5(CBhG)_{60}PVDF_{10}$ composites is higher than the pristine $S_{25}(CBhG)_{65}PVDF_{10}$ composite. The diffusion coefficients for samples with various FNPs are almost the same except for BFO nanoparticles, which exhibited slightly higher values favoring good ionic conduction for lithium ions. The values of solution

resistances (R_s) for FNPs doped composite cathodes varies between 11.08 Ω to 5.32 Ω. In comparison, the pristine $S_{25}(CBhG)_{65}PVDF_{10}$ composite exhibited low solution resistance (R_s) of ~4.92 Ω and a low charge transference resistance of ~7.63 Ω. R_s reflects not only the electrolytic solution resistance but also a penetration or an affinity of the solution within the cathode, anode, and separator. The higher R_s and R_{ct} for the BNTFN battery may be due to the insufficient penetration or affinity of the solution within them [47]. The increase in R_s due to the cyclic charge-discharge processes might have a relation with electrolyte degradation.

Table 4.3. Interfacial characteristics calculated using EIS with R(CR)W model.

Electrodes	$R_s[\Omega]$	C	R_{ct} [Ω]	W_{sc}	D_{li} [cm^2/s]
S/CBhG/PVDF	4.92	0.027	7.63	0.0320	2.17×10^{-16}
S/BTO/CBhG/PVDF	8.15	1.459×10^{-8}	12.67	0.1438	3.43×10^{-15}
S/BFO/CBhG/PVDF	5.32	1.948×10^{-8}	69.77	0.0907	4.15×10^{-15}
S/BNTFN/CBhG/PVDF	14.85	0.179	12.82	0.0268	2.91×10^{-15}
S/BNTFC/CBhG/PVDF	11.08	1.234×10^{-8}	13.11	0.0705	4.11×10^{-15}

4.3.5 Electrochemical properties

Figure 4.6 shows discharge-charge profiles for the $S_{25}(CBhG)_{65}PVDF_{10}$, and $S_{25}FNPs_5(CBhG)_{60}PVDF_{10}$ composite cathodes with the varying fractions of FNPs. The $S_{25}(CBhG)_{65}PVDF_{10}$ cathode without FNPs provide initial specific capacity of 1123 mAh/g$_s$ at current density of 0.2 mA/cm^2 and reversible capacity of 541 mAh/g$_s$ after 134 cycles at 0.3 mA/cm^2 as shown in Figure 4.6a. and Figure 4.6f. The specific capacity values of $S_{25}BTO_5(CBhG)_{60}PVDF_{10}$ cathode for the 1st, 2nd, and 110th cycles were 1402, 1287, 625 mAh/g$_s$ respectively, as shown in Figure 4.6b and Figure 4.6g. The specific capacity values of $S_{25}BFO_5(CBhG)_{60}PVDF_{10}$ cathode for the 1st, 2nd, and 116th cycles were 1430, 1325, 564 mAh/g$_s$ respectively, as shown in Figure 4.6c and Figure 4.6h. The specific

capacity values of $S_{25}BNTFN_5(CBhG)_{60}PVDF_{10}$ for the 1st, 2nd, and 158th cycles were 1486, 1287, 676 mAh/g$_s$ respectively, as shown in Figure 4.6d and Figure 4.6i. The specific capacity values of $S_{25}BNTFC_5(CBhG)_{60}PVDF_{10}$ cathode for the 1st, 2nd, and 107th cycles were 1509, 1350, 505 mAh/g$_s$ respectively, as shown in Figure 4.6e and Figure 4.6j. For all batteries, the current density was 0.2 mA/cm^2 for the first three cycles and 0.3 mA/cm^2 for the rest of the cycles. These remarkable values were attributed to the trap of polysulfides through polar interactions with the FNPs particles embedded in the cathode [48]. The Coulombic efficiency values of $S_{25}FNPs_5(CBhG)_{60}PVDF_{10}$ composite cathodes were in the range of 80-90%, as shown in Figure 4.6g–4.6j improving from 67% for the composite cathode without FNPs. This indicates that the modified composite cathodes have an improved reversible capacity. In Figure 4.6a–4.6e, the initial discharge capacities of various $S_{25}FNPs_5(CBhG)_{60}PVDF_{10}$ composites values improved to 1400-1500 mAh/g$_s$, in comparison to 1123 mAh/g$_s$ for the pristine $S_{25}(CBhG)_{65}PVDF_{10}$. The comparison of specific capacity, areal capacity, and capacity retention for the Li-S batteries is shown in Table 4.4.
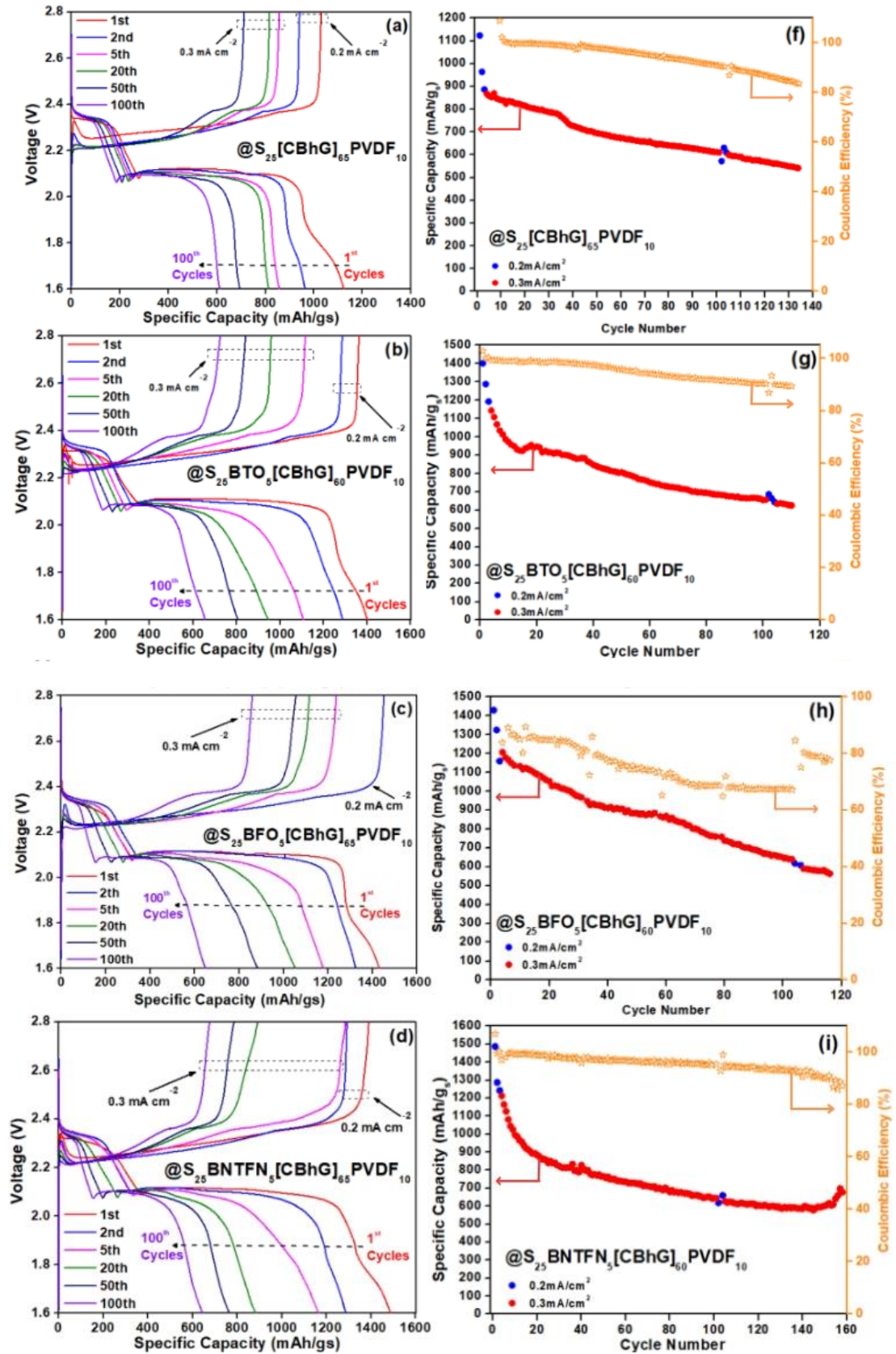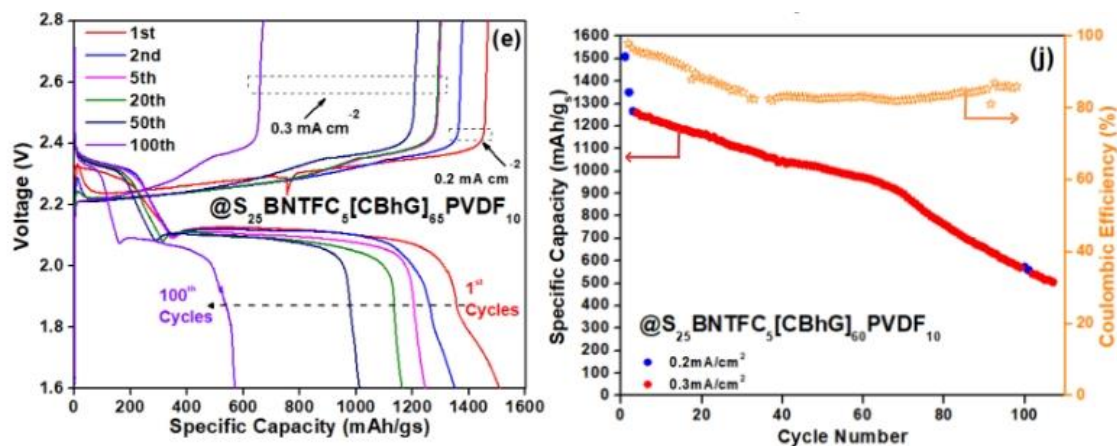
Figure 4.6. Discharge-Charge profiles and specific capacity, Coulombic efficiency in function of cycle number of battery with $S_{25}(CBhG)_{65}PVDF_{10}$ at various current density from 0.2 mA/cm^2 to 0.3 mA/cm^2 (a-f), battery with $S_{25}BTO_5(CBhG)_{60}PVDF_{10}$ (b-g), battery with $S_{25}BFO_5(CBhG)_{60}PVDF_{10}$ values (c-h), battery with $S_{25}BNTFN_5(CBhG)_{60}PVDF_{10}$ values (d-i), and battery with $S_{25}BNTFC_5(CBhG)_{60}PVDF_{10}$ values (e-j). All batteries were run over cycling at 0.2 mA/cm^2 (first 3 cycles were run at 0.3 mA/cm^2).

Table 4.4. Comparison of specific capacity [mAh/g$_s$] between 1st and 100th cycles, areal capacity for 1st cycle, and capacity retention for all batteries.

Electrodes	Specific. Cap. 1st Cyc. [mAh/g$_s$]	Specific. Cap. 100th Cyc. [mAh/g$_s$]	Areal Cap. 1st Cyc. [mAh/cm^{-2}]	Capacity. Retention [%]
S/CBhG/PVDF	1123	612	4.84	54.49
S/BTO/CBhG/PVDF	1402	655	5.08	46.72
S/BFO/CBhG/PVDF	1430	648	5.60	45.31
S/BNTFN/CBhG/PVDF	1486	645	5.12	43.40
S/BNTFC/CBhG/PVDF	1509	572	6.74	37.90

Figure 4.7a represents three plateau regions in the charge-discharge profiles which are typical characteristics of the Li-S batteries. The formation of a valley at the end of the first discharge plateau and a peak at the beginning of the charging process can be seen in the curves during transition of ion from solid to liquid. In comparison to $S_{25}(CBhG)_{65}PVDF_{10}$, $S_{25}BNTFC_5(CBhG)_{60}PVDF_{10}$ cathodes exhibited improved S utilization in terms of

specific capacity (1123 mAh/g$_s$ versus 1509 mAh/g$_s$) with mass loading (4.84 mg$_s$/cm^2 versus 6.74 mg$_s$/cm^2) and over potential ($\Delta E \sim 0.16$ V versus 0.17 V at the 2nd cycle) respectively as shown in Figure 4.7(a–b). Cycle performance testing (Figure 4.7b) is conducted to quantify population of battery according to the requirements and the life expectation of the battery for its various applications. On varying current density, the discharge performance will result in two-way acceleration by means of increase in the battery degradation (capacity fade) rate and reduction in the time to complete one full charge-discharge cycle. Hence it is very important to achieve a good cycling performance of the battery, its testing should be at various current densities for the accelerated use of Li-S batteries. To achieve high areal capacity, high mass loading of 4.31 mg$_s$/cm^2, 3.625 mg$_s$/cm^2, 3.92 mg$_s$/cm^2, 3.45 mg$_s$/cm^2, and 4.46 mg$_s$/cm^2 was acquired respectively. Highest initial discharge areal capacity reached >6 mAh/cm^2.
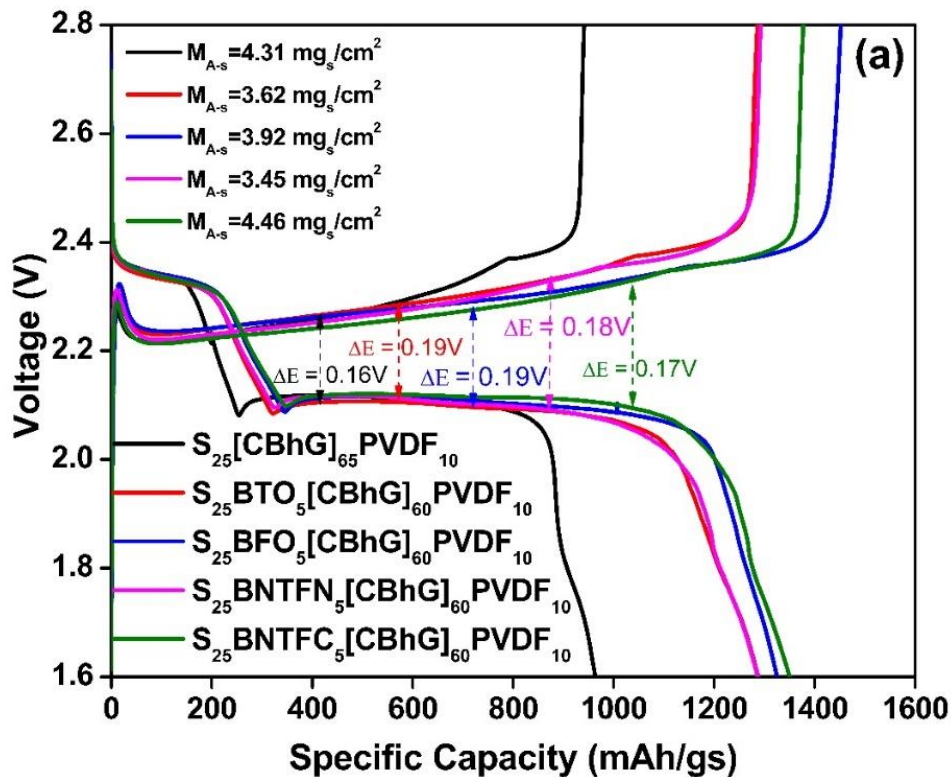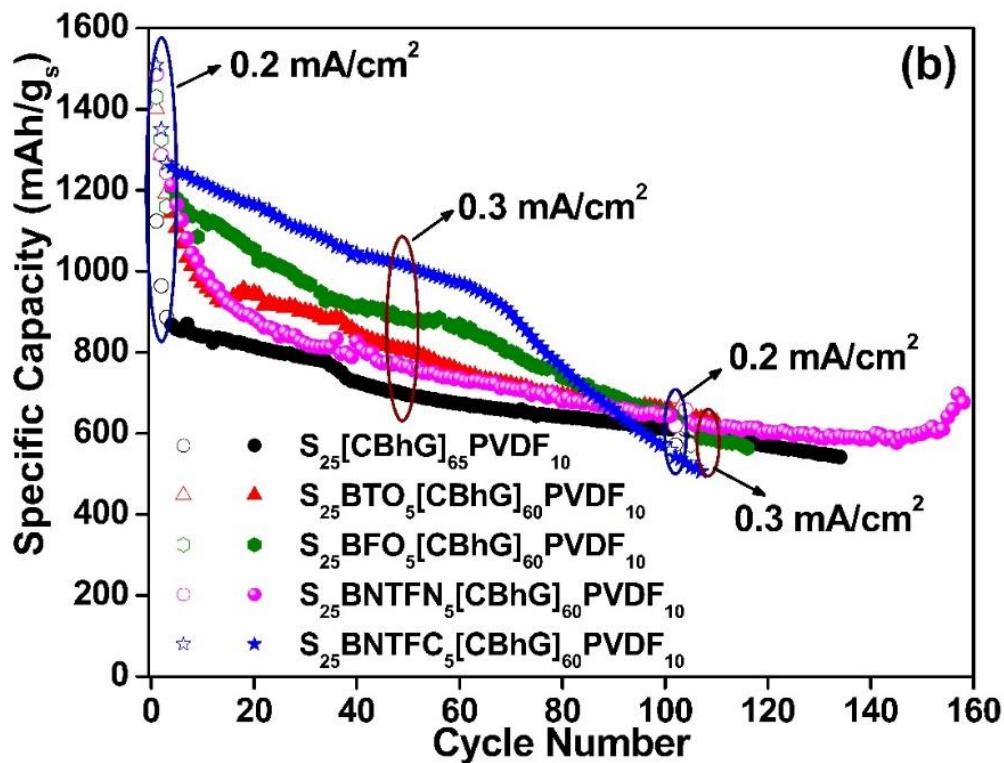
Figure 4.7. Comparison of electrochemical performance of $S_{25}(CBhG)_{65}PVDF_{10}$ and $S_{25}FNPs_5(CBhG)_{60}PVDF_{10}$ materials: (a) discharge-charge profile of two cycles for the batteries evaluated at current densities of 0.2 mA/cm^2, (b) Specific capacity in function of cycle number at a current density of 0.2 mA/cm^2 and 0.3 mA/cm^2.

Figure 4.8 shows that the values of areal capacity reached 4.84 mAh/cm^2, 5.08 mAh/cm^2, 5.60 mAh/cm^2, 5.12 mAh/cm^2, and 6.74 mAh/cm^2 for $S_{25}(CBhG)_{65}PVDF_{10}$, $S_{25}BTO_5(CBhG)_{60}PVDF_{10}$, $S_{25}BFO_5(CBhG)_{60}PVDF_{10}$, $S_{25}BNTFN_5(CBhG)_{60}PVDF_{10}$, and $S_{25}BNTFC_5(CBhG)_{60}PVDF^{10}$ cathode composites respectively. Among the investigated composites, the highest areal capacity was obtained for the $S_{25}BNTFC_5(CBhG)_{60}PVDF_{10}$ cathode [49].
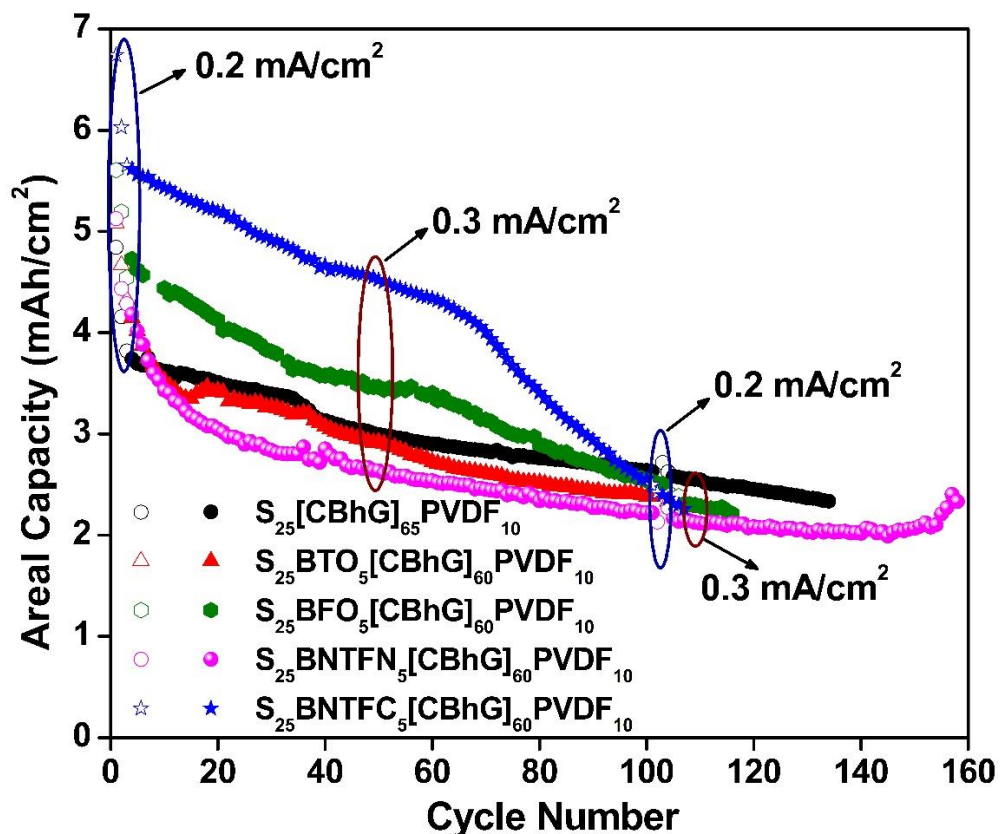
Figure 4.8. Areal capacity for the batteries evaluated at different current densities ran at 0.2 mA/cm^2 and 0.3 mA/cm^2. The representation of the composite cathodes are black circles for $S_{25}(CBhG)_{65}PVDF_{10}$, red triangle for $S_{25}BTO_5(CBhG)_{60}PVDF_{10}$, green hexagonal for $S_{25}BFO_5(CBhG)_{60}PVDF_{10}$, magenta circles for $S_{25}BNTFN_5(CBhG)_{60}PVDF_{10}$, and blue stars for $S_{25}BNTFC_5(CBhG)_{60}PVDF_{10}$ composites.

References

[1] A. Manthiram, S.H. Chung, C. Zu, Lithium-Sulfur Batteries: Progress and Prospects, Adv Mater 27(12) (2015) 1980-2006.

[2] R. Song, R. Fang, L. Wen, Y. Shi, S. Wang, F. Li, A trilayer separator with dual function for high performance lithium–sulfur batteries, Journal of Power Sources 301 (2016) 179-186.

[3] P.G. Bruce, S.A. Freunberger, L.J. Hardwick, J.M. Tarascon, Li-O_2 and Li-S batteries with high energy storage., *Nature Materials 11*(1) (**2011**) 19-29.

[4] R. Fang, S. Zhao, Z. Sun, D.W. Wang, H.M. Cheng, F. Li, More Reliable Lithium-Sulfur Batteries: Status, Solutions and Prospects, Adv Mater 29(48) (2017).

[5] D. Lv, J. Zheng, Q. Li, X. Xie, S. Ferrara, Z. Nie, L.B. Mehdi, N.D. Browning, J.-G. Zhang, G.L. Graff, J. Liu, J. Xiao, High Energy Density Lithium-Sulfur Batteries: Challenges of Thick Sulfur Cathodes., *Advanced Energy Materials 5*(16) (**2015**).

[6] Z.W. Seh, Y. Sun, Q. Zhang, Y. Cui, Designing high-energy lithium-sulfur batteries, Chem Soc Rev 45(20) (2016) 5605-5634.

[7] Yuriy V. Mikhaylik, z.a.J.R. Akridge, Polysulfide Shuttle Study in the Li-S Battery System, Journal ofThe Electrochemical Society 151 (11) (2004) A1969-A1976.

[8] G. Zhou, L. Li, D.W. Wang, X.Y. Shan, S. Pei, F. Li, H.M. Cheng, A flexible sulfur-graphene-polypropylene separator integrated electrode for advanced Li-S batteries, Adv Mater 27(4) (2015) 641-7.

[9] J. Liang, L. Yin, X. Tang, H. Yang, W. Yan, L. Song, H.M. Cheng, F. Li, Kinetically Enhanced Electrochemical Redox of Polysulfides on Polymeric Carbon Nitrides for Improved Lithium-Sulfur Batteries, ACS Appl Mater Interfaces 8(38) (2016) 25193-201.

[10] X. Han, Z. Yang, B. Zhao, S. Zhu, L. Zhou, J. Dai, J.W. Kim, B. Liu, J.W. Connell, T. Li, B. Yang, Y. Lin, L. Hu, Compressible, Dense, Three-Dimensional Holey Graphene Monolithic Architecture, ACS Nano 11(3) (2017) 3189-3197.

[11] Y.-J. Yen, T.-H. Chen, Y.-T. Wang, A. Robles, M. Đerić, O.Š. Miljanić, W. Kaveevivitchai, S.-H. Chung, Selective chemisorption of polysulfides by porous molecular crystal: Cathode host materials for lean-electrolyte lithium-sulfur cells with high electrochemical stability, Journal of Power Sources 565 (2023).

[12] S.S. Shah, M.A. Aziz, E. Cevik, M. Ali, S.T. Gunday, A. Bozkurt, Z.H. Yamani, Sulfur nano-confinement in hierarchically porous jute derived activated carbon towards high-performance supercapacitor: Experimental and theoretical insights, Journal of Energy Storage 56, (2022).

[13] S.-x. Yan, Q. Wang, S.-h. Luo, Y.-h. Zhang, X. Liu, Y.-g. Liu, Z.-y. Wang, A.-m. Hao, T.-f. Yi, Coal-based S hybrid self-doped porous carbon for high-performance supercapacitors and potassium-ion batteries, Journal of Power Sources 461 (2020).

[14] M. Zhang, Z. Song, H. Liu, A. Wang, S. Shao, MoO_2 coated few layers of MoS_2 and FeS_2 nanoflower decorated S-doped graphene interoverlapped network for high-energy asymmetric supercapacitor, J Colloid Interface Sci 584 (2021) 418-428.

[15] F.R. Maria Sundar Raj, N.V. Jaya, G. Boopathi, D. Kalpana, A. Pandurangan, S-doped activated mesoporous carbon derived from the Borassus flabellifer flower as active electrodes for supercapacitors, Materials Chemistry and Physics 240 (2020).

[16] W. Gu, M. Sevilla, A. Magasinski, A.B. Fuertes, G. Yushin, Sulfur-containing activated carbons with greatly reduced content of bottle neck pores for double-layer capacitors: a case study for pseudocapacitance detection, Energy & Environmental Science 6(8) (2013).

[17] S. Cao, D. Liu, H. Ding, H. Lu, J. Gui, Towards understanding corrosion inhibition of sulfonate/carboxylate functionalized ionic liquids: An experimental and theoretical study, J Colloid Interface Sci 579 (2020) 315-329.

[18] R.K. Sahoo, S. Singh, J.M. Yun, S.H. Kwon, K.H. Kim, Sb_2S_3 Nanoparticles Anchored or Encapsulated by the Sulfur-Doped Carbon Sheet for High-Performance Supercapacitors, ACS Appl Mater Interfaces 11(37) (2019) 33966-33977.

[19] C. Wang, S.-H. Zhang, L. Zhang, R. Xi, D.-P. Jiang, Z.-Y. Chen, H. Huang, L.-Y. Ding, G.-B. Pan, Natural bamboo leaves derived sulphur-doped mesoporous heteroatom enriched carbon for high-performance supercapacitors and gas sensors, Journal of Power Sources 443 (2019).

[20] Y. Zhou, S.L. Candelaria, Q. Liu, Y. Huang, E. Uchaker, G. CaO, Sulfur-rich carbon cryogels for supercapacitors with improved conductivity and wettability, Journal of Materials Chemistry A 2(22) (2014).

[21] X. Ma, X. Song, G. Ning, L. Hou, Y. Kan, Z. Xiao, W. Li, G. Ma, J. Gao, Y. Li, S-Doped Porous Graphene Microspheres with Individual Robust Red-Blood-Cell-Like

Microarchitecture for Capacitive Energy Storage, Industrial & Engineering Chemistry Research 56(34) (2017) 9524-9532.

[22] E.H.M. Salhabi, J. Zhao, J. Wang, M. Yang, B. Wang, D. Wang, Hollow Multi-Shelled Structural TiO_{2-x} with Multiple Spatial Confinement for Long-Life Lithium-Sulfur Batteries, Angew Chem Int Ed Engl 58(27) (2019) 9078-9082.

[23] J. Song, Z. Yu, M.L. Gordin, D. Wang, Advanced Sulfur Cathode Enabled by Highly Crumpled Nitrogen-Doped Graphene Sheets for High-Energy-Density Lithium-Sulfur Batteries, Nano Lett 16(2) (2016) 864-70.

[24] B.J.K.a.B. Noheda, Ferroelectric chalcogenides—materials at the edge, Science 353(6296) (2016).

[25] W. Zhou, B. Guo, H. Gao, J.B. Goodenough, Low-Cost Higher Loading of a Sulfur Cathode, Advanced Energy Materials 6(5) (2016).

[26] X. Ji, K.T. Lee, L.F. Nazar, A highly ordered nanostructured carbon-sulphur cathode for lithium-sulphur batteries, Nat Mater 8(6) (2009) 500-6.

[27] J. Xiao, H. Wang, X. Li, Z. Wang, J. Ma, H. Zhao, N-doped carbon nanotubes as cathode material in Li–S batteries, Journal of Materials Science: Materials in Electronics 26(10) (2015) 7895-7900.

[28] T. Liu, L. Zhang, B. Cheng, X. Hu, J. Yu, Holey Graphene for Electrochemical Energy Storage, Cell Reports Physical Science 1(10) (2020).

[29] T. Yim, S.H. Han, N.H. Park, M.-S. Park, J.H. Lee, J. Shin, J.W. Choi, Y. Jung, Y.N. Jo, J.-S. Yu, K.J. Kim, Effective Polysulfide Rejection by Dipole-Aligned $BaTiO_3$ Coated

Separator in Lithium-Sulfur Batteries, Advanced Functional Materials 26(43) (2016) 7817-7823.

[30] H. Cheng, H. Liu, H. Jin, N. Cai, C. Gao, S. Zhao, M. Wang, Suppression of polysulfide shuttling with a separator modified using spontaneously polarized bismuth ferrite for high performance lithium–sulfur batteries, Journal of Materials Chemistry A 8(32) (2020) 16429-16436.

[31] K. Xie, Y. You, K. Yuan, W. Lu, K. Zhang, F. Xu, M. Ye, S. Ke, C. Shen, X. Zeng, X. Fan, B. Wei, Ferroelectric-Enhanced Polysulfide Trapping for Lithium-Sulfur Battery Improvement, Adv Mater 29(6) (2016).

[32] Z. Zhao, G. Li, Z. Wang, M. Feng, M. Sun, X. Xue, R. Liu, H. Jia, Z. Wang, W. Zhang, H. Li, Z. Chen, Black $BaTiO_3$ as Multifunctional Sulfur Immobilizer for Superior Lithium Sulfur Batteries, Journal of Power Sources 434 (2019).

[33] B. Tripathi, R.K. Katiyar, G. Morell, A. Dixit, R.S. Katiyar, $BiFeO_3$ Coupled Polysulfide Trapping in C/S Composite Cathode Material for Li-S Batteries as Large Efficiency and High Rate Performance, Energies 14(24) (2021).

[34] P. Półrolniczak, M. Walkowiak, J. Kaźmierczak-Raźna, D. Kasprzak, D.E. Mathew, M. Kathiresan, A.M. Stephan, N. Angulakshmi, BaTiO3-g-GO as an efficient permselective material for lithium–sulfur batteries, Materials Chemistry Frontiers 5(2) (2021) 950-960.

[35] C.O.P.-R. Claudia C. Zuluaga-Gómez, Balram Tripathi, Rajesh K. Katiyar, Dhiren K. Pradhan, Gerardo Morell, Yi Lin, Margarita Correa, and Ram S. Katiyar, Holey

Graphene/Ferroelectric/Sulfur Composite Cathodes for HighCapacity Lithium−Sulfur Batteries, ACS OMEGA (2023).

[36] Y. Lin, X. Han, C.J. Campbell, J.-W. Kim, B. Zhao, W. Luo, J. Dai, L. Hu, J.W. Connell, Holey Graphene Nanomanufacturing: Structure, Composition, and Electrochemical Properties, Advanced Functional Materials 25(19) (2015) 2920-2927.

[37] X. Zhao, W. Liu, W. Chen, S. Li, Preparation and properties of BaTiO3 ceramics from the fine ceramic powder, Ceramics International 41 (2015) S111-S116.

[38] M.S. Bernardo, T. Jardiel, M. Peiteado, A.C. Caballero, M. Villegas, Reaction pathways in the solid state synthesis of multiferroic BiFeO3, Journal of the European Ceramic Society 31(16) (2011) 3047-3053.

[39] Y. Lin, K.J. Jones, L.C. Greenburg, J.W. Kim, L. Hu, J.W. Connell, Facile, Solvent-Free Preparation of High Density, High Mass Loading Sulfur Cathodes Enabled by Dry-Pressable Holey Graphene Scaffolds., Batteries & Supercaps 2(9) (**2019**) 774-783.

[40] S.R. Das, R.N.P. Choudhary, P. Bhattacharya, R.S. Katiyar, P. Dutta, A. Manivannan, M.S. Seehra, Structural and Multiferroic Properties of La-Modified $BiFeO_3$ Ceramics, Journal of Applied Physics 101(3) (2007).

[41] X. Chen, J. Xiao, J. Yao, Z. Kang, F. Yang, X. Zeng, Room Temperature Magnetoelectric Coupling Study in Multiferroic $Bi_4NdTi_3Fe_{0.7}Ni_{0.3}O_{15}$ Prepared by a Multicalcination Procedure., Ceramics International 40(5) (2014) 6815-6819.

[42] F.J. Yang, P. Su, C. Wei, X.Q. Chen, C.P. Yang, W.Q. Cao, Large Magnetic Response in $(Bi_4Nd)Ti_3(Fe_{0.5}Co_{0.5})O_{15}$ Ceramic at Room-Temperature, Journal of Applied Physics 110(12) (2011).

[43] G. Radhika, R. Subadevi, K. Krishnaveni, W.R. Liu, M. Sivakumar, Synthesis and Electrochemical Performance of PEG-MnO(2)-Sulfur Composites Cathode Materials for Lithium-Sulfur Batteries, J Nanosci Nanotechnol 18(1) (2018) 127-131.

[44] M. Li, Y. Zhang, Z. Bai, W.W. Liu, T. Liu, J. Gim, G. Jiang, Y. Yuan, D. Luo, K. Feng, R.S. Yassar, X. Wang, Z. Chen, J. Lu, A Lithium-Sulfur Battery using a 2D Current Collector Architecture with a Large-Sized Sulfur Host Operated under High Areal Loading and Low E/S Ratio, Adv Mater 30(46) (2018) e1804271.

[45] T.Q. Nguyen, C. Breitkopf, Determination of Diffusion Coefficients Using Impedance Spectroscopy Data, Journal of The Electrochemical Society 165(14) (2018) E826-E831.

[46] T. Wang, Q. Zhang, J. Zhong, M. Chen, H. Deng, J. Cao, L. Wang, L. Peng, J. Zhu, B. Lu, 3D Holey Graphene/Polyacrylonitrile Sulfur Composite Architecture for High Loading Lithium Sulfur Batteries, Advanced Energy Materials 11(16) (2021).

[47] M. Gaberscek, Understanding Li-based battery materials via electrochemical impedance spectroscopy, Nat Commun 12(1) (2021) 6513.

[48] M. Rana, S.A. Ahad, M. Li, B. Luo, L. Wang, I. Gentle, R. Knibbe, Review on areal capacities and long-term cycling performances of lithium sulfur battery at high sulfur loading, Energy Storage Materials 18 (2019) 289-310.

[49] C.Y. Fan, H.Y. Yuan, H.H. Li, H.F. Wang, W.L. Li, H.Z. Sun, X.L. Wu, J.P. Zhang, The Effective Design of a Polysulfide-Trapped Separator at the Molecular Level for High Energy Density Li-S Batteries, ACS Appl Mater Interfaces 8(25) (2016) 16108-15.

Chapter 5

Conclusion and Future Plan

4.1 Conclusion

We have fabricated $S_{47.5}FNPs_5hG_{47.5}$ cathodes where FNPs were ferroelectric nanoparticles such as: $BaTiO_3$, $BiFeO_3$, $Bi_4NdTi_3Fe_{0.7}Ni_{0.3}O_{15}$, and $Bi_4NdTi_3Fe_{0.5}Co_{0.5}O_{15}$ by means of solid-state reaction route. The cathodes were synthesized by a solvent-free and binder-free process and tested for high-capacity, long-cyclability of Li−S batteries at high sulfur mass loadings. A dry compression manufacturing process was used to facilitate the bonding between the sulfur and the ferroelectric nanoparticle layer to generate a more stable cathode. Due to the unique characteristics and design of $S_{47.5}FNPs_5hG_{47.5}$, composite electrodes with high mass loading delivered a high specific capacity of 1409 mAh/g_s for the $S_{47.5}BTO_5hG_{47.5}$ cathode and an areal capacity up to ∼10 mAh/cm^2 for $S_{47.5}BTO_5hG_{47.5}$ compounds under various current rates with outstanding cyclic stability. The decisive role played by hG and FNPs in $S_{50}hG_{50}$ composite electrodes is to suppress the shuttling of polysulfides. The hG framework greatly improves the electronic conductivity of the electrode, facilitating the active material to fully participate in electrochemical reactions. The customized nanoscale porous structure design significantly shortens the Li$^+$ transport path and ensures high-speed ion conduction, guaranteeing better rate performance within the electrodes. The hG and FNPs can effectively mitigate structural change of electrodes during the discharge−charge process as well as protecting the electrode and maintaining good cycling stability. The utilization of hG and FNPs in the fabrication of high-mass-

loading lithium−sulfur batteries may find practical applications toward the future commercialization of these advanced electrochemical energy storage systems.

The sulfur composite was prepared, with hG as the dry pressable matrix and conductive scaffold $S_{25}(FNPs)_5CBhG_{60}PVDF_{10}$ cathodes. The FNPs were added to improve electrochemical performance by reducing polysulfide shuttling. The Raman spectra confirmed the dominance of hG and the presence of FNPs in the composites, while SEM images confirmed the homogeneous distribution of FNPs throughout the composite matrix. EIS analysis confirmed the good diffusion of Li^+ ions during charge–discharge of the composite electrodes. The enhancement in diffusion coefficients due to the coupling of FNPs was attributed to the improvement in the rate performance of the composites. The electrochemical performance represents an innovative contribution to the development of high energy density and stable Li-S batteries. The significant improvement in the stability as well as the dramatic change in the cyclability of the Li-S batteries was attributed to the contribution of the bi-functional effect of ferroelectricity coupled with the hG/S composite system. When $S_{25}(BNTFN)_5CBhG_{60}PVDF_{10}$ nanoparticles were incorporated into the cathode's fabrication, the observed capacity at the first cycle was 1486 mAh/g_s, and after ~158 cycles, it was still high (~676 mAh/g_s). This also occurred with $S_{25}(BNTFC)_5CBhG_{60}PVDF_{10}$, where the capacity started at ~1509 mAh/g_s, and after 100 cycles, had a value of ~500 mAh/g_s. The electrochemical performance retention of the fabricated electrodes up to 100 cycles showed a specific capacity (~541 mAh/g_s). The Coulombic efficiency improved by more than 10% upon adding ferroelectric nanoparticles into the composite cathode. The highest areal capacity value obtained for the composite electrodes was 6.74 mAh/cm^2. The incorporation of ferroelectric nanoparticles into the

cathodes of Li-S batteries controlled the formation of polysulfides due to their internal electric fields, which reduced the rapid formation of polysulfides. This was attributed to the effect of an extra internal field induced by ferroelectric nanoparticles. The development of such composite electrodes will provide effective alternatives towards a strategy for suppressing the polysulfide shuttle phenomenon in the Li-S cell system and contribute to the advanced design of better Li-S cathodes for the next generation of energy storage systems.

4.2 Future plan

I envision my future research investigation on energy storage to focus on implementing the use of solid-state electrolyte. I want to investigate this field because of its novel and promising applications from automotive vehicles to electronic devices, due to their high energy density, ecological friendliness, fast charging time, and long cycle life. I will focus on the fabrication of $Li_7La_3Zr_2O_{12}$ oxide (LLZO) solid electrolyte using the Sol-Gel method, which is a simple way to synthesize LLZO at room temperature. The results of batteries fabricated using this type of solid electrolyte are promising for future applications. Using a solid electrolyte (LLZO) in the study of cathodes containing sulfur, holey graphene, carbon black, PVDF and ferroelectric nanoparticles will help to improve the electrochemical properties of Li-S batteries. This research will open a new avenue for understanding advances in energy storage materials such as batteries. This research shift promises very innovative results.